Dottorato di Ricerca in Fisica

XX ciclo

Alma Mater Studiorum
Università degli Studi di Bologna

SETTORE DISCIPLINARE: FIS/03

TESI PER IL CONSEGUIMENTO DEL
TITOLO DI DOTTORE DI RICERCA

4H SILICON CARBIDE PARTICLE DETECTORS: STUDY OF THE DEFECTS INDUCED BY HIGH ENERGY NEUTRON IRRADIATION.

Candidato: Filippo Fabbri

Supervisore: Chiar.mo Prof. Anna Cavallini

_____

Coordinatore: Chiar.mo Prof. Fabio Ortolani

_____

Introduction 4

Chapter 1: Silicon Carbide and related properties. 6

Introduction 6
1.1 Material Properties 7
1.2 Material Growth 11
1.2.1 BULK GROWTH 12
1.2.2 EPITAXIAL GROWTH 14
1.3 Crystal Imperfections 16
1.3.1 DOPING 17
1.3.2 SCREW DISLOCATIONS 18
1.3.4 STACKING FAULTS 19
Bibliography 21

Chapter 2: Silicon Carbide Particle Detector. 24

Introduction 24
2.1 Semiconductor junctions 26
2.2 Schottky Diodes 28
2.2.1 FORWARD OPERATION 29
2.2.2 REVERSE OPERATION 31
2.3 *p / n* junctions 34
2.3.1 FORWARD OPERATION 36
2.3.2 REVERSE OPERATION 39
2.4 Junction Edge Terminations 41
2.4.1 JUNCTION TERMINATING EXTENTION 41
2.4.2 FIELD RING 42
2.5 Current-Voltage and Activation-Energy Measurements Set-up 43
Bibliography 45

Chapter 3: Physical principles of measurements 47

3.1 Capacitance Voltage Measurements 47
3.1.1 CAPACITANCE VOLTAGE MEASUREMENTS ON SCHOTTKY DIODES 47
3.1.2 CAPACITANCE VOLTAGE MEASUREMENTS ON JUNCTION DIODE 49
3.1.3 CAPACITANCE-VOLTAGE MEASUREMENTS SET-UP 51
3.2 Electrical and Electro-optical properties of defect by complementary transient spectroscopy 53
3.2.1 PHYSICS OF CARRIER CAPTURE AND EMISSION AT A TRAP 54
3.2.2 MAJORITY CARRIER TRAPS SPECTROSCOPY: DLTS 59
3.2.3 PHOTO-CONDUCTIVITY TRANSIENT SPECTROSCOPY 62

3.2.4 THERMAL TRANSIENT SPECTROSCOPY SET-UP: DLTS, PICTS. 66
Temperature controller and cryogenic apparatus. 66
Impulse generator and equipment gauges. 66
Exponential correlators and double boxcar averagers 67
3.3 Scanning Electron Microscopy and Spectroscopy 70
3.3.1 BEAM-SAMPLE INTERACTION 71
3.3.2 IMAGES BY SECONDARY ELECTRONS 73
3.3.3 ELECTRON BEAM INDUCED CURRENT 73
3.3.4 CATHODOLUMINESCENCE 75
3.3.5 CATHODOLUMINESCENCE SET-UP 77
Bibliography 80

Chapter 4: Neutron irradiation induced defect in 4H-SiC particle detector 82

4.1 Schottky particle detector 83
4.1.1 ANALYZED SAMPLES AND IRRADIATION CONDITION 83
4.1.2 EFFECT OF IRRADIATION ON THE ANALYZED SAMPLES: EVOLUTION OF TRANSPORT PROPERTIES 85
4.1.3 EFFECT OF IRRADIATION INVESTIGATED BY DLTS AND PICTS 89
4.2 Junction particle detector 97
4.2.1 ANALYZED SAMPLES AND IRRADIATION CONDITION 97
4.2.2 Defect analysis on un-irradiated samples by capacitance transient spectroscopy 99
4.2.2 DEFECT ANALYSIS OF UN-IRRADIATED SAMPLES BY CATHODOLUMINESCENCE 113
4.2.3 EFFECT OF IRRADIATION: TRANSPORT PROPERTIES EVOLUTION. 120
4.2.4 EFFECT OF IRRADIATION BY PICTS, CL AND SE IMAGINING. 121
Conclusions 126
Bibliography 128

Conclusions 133

Introduction

During the last decade advances in the field of sensor design and improved base materials have pushed the radiation charge collection efficiency of the current silicon detector technology to impressive performance. It should allow operation of the tracking systems of the Large Hadron Collider (LHC) experiments at nominal luminosity (10^{34} $cm^{-2}s^{-1}$) for about 10 years [CMS]. However, the predicted 1MeV neutron equivalent fluences of fast hadrons, ranging from 3 x 10^{15} cm^{-2} at a radius of R = 4 cm to 3 x 10^{13} cm^{-2} at R = 75 cm for an integrated luminosity of 500 fb^{-1}, will lead to substantial radiation damage of the sensors and degradation of their performance [RD48]. For the innermost silicon pixel layers a replacement of the detectors may become necessary before 500 $femtobarn^{-1}$ has been reached. One option that has recently been discussed to extend the physics reach of the LHC, is a luminosity upgrade to 10^{35} $cm^{-2}s^{-1}$, envisaged after the year 2012. Present pixel detector technology, applied at larger radius (e.g. R > 20 cm), may be a viable but much cost extensive solution. This requires a tracking layer down to R = 4 cm where one would face fast hadron fluences above 10^{16} cm^{-2} (2500 fb^{-1}). The current silicon detectors are unable to cope with such an environment. The necessity to separate individual interactions at a collision rate of the order of 100MHz may also exceed the capability of available technology. It is well possible that a fluence of 10^{16} cm^{-2} corresponds to the operating limit of silicon sensors for temperatures close to room temperature. Other sensor materials are therefore under investigation [Lebedev1].

Silicon carbide (SiC), which has recently been recognized as potentially radiation hard, is now studied. Epitaxial 4H–SiC with very high crystal quality is now available and Schottky barrier detectors have been studied with α-particles from a ^{241}Am source. Charge collection efficiency (CCE) of 100% has been measured. Radiation damage of these devices has been tested with a ^{60}Co γ-source and 8.2MeV electrons up to a dose of 40MRad and with 24 GeV protons up to a fluence of 9 x 10^{13} cm^{-2}. Although the effective carrier

concentration (N_{eff}) was observed to decrease from the initial value after the highest electron dose of 40 MRad, no influence on the CCE was observed. Also after the highest gamma dose and proton fluence a CCE of 100% was observed at room temperature. Furthermore, the leakage current decreased after irradiation. The charge collection signal is stable and reproducible, showing an absence of priming and polarization effects.

In this work it was analyzed the effect of high energy neutron irradiation on 4H-SiC particle detectors. Schottky and junction particle detectors were irradiated with 1 MeV neutrons up to fluence of 10^{16} cm^{-2}. It is well known that the degradation of the detectors with irradiation, independently of the structure used for their realization, is caused by irradiation induced defects, like creation of point-like defects, dopant deactivation and dead layer formation and that a crucial aspect for the understanding of the defect kinetics at a microscopic level is the correct identification of the crystal defects in terms of their electrical activity.

In order to clarify the defect kinetic investigations were carried out thermal transient spectroscopys (DLTS and PICTS) analysis of different samples irradiated at increasing fluences. The defect evolution was correlated with the transport properties of the irradiated detector, always comparing with the un-irradiated one. The charge collection efficiency degradation of Schottky detectors induced by neutron irradiation was related to the increasing concentration of defects as function of the neutron fluence.

The state-of-art on SiC is given in chapter 1. Chapter 2 describes the main issues of different SiC particle detector structures. Chapter three illustrates the experimental techniques employed in this thesis, i.e. capacitance voltage (C-V), Deep Level Transient Spectroscopy (DLTS), Photo Induced Current Spectroscopy (PICTS) and Secondary Electron Microscopy (SEM) in Electron Beam Induced Current (EBIC) and in Cathodoluminescence (CL) mode. Results for the electrical performance of the diodes and for the analyses of electrically active defects induced by the neutron irradiation are reported in chapter 4. Finally, conclusions are drawn.

Chapter 1: Silicon Carbide and related properties.

Introduction

Silicon carbide is a semiconductor with a wide, indirect band gap. Due to its composition SiC it is the only stable compound in the binary phase diagram of the two groups IV elements, silicon and carbon. It is thermally stable up to about 2000 °C, even in oxidizing and aggressive environments. Of all the wide band gap semiconductors, silicon carbide is presently the most intensively studied one and the one with the highest potential to reach market maturity in a wide field of device applications. Silicon carbide was discovered in 1824 by the Swedish scientist Jons Jakob Berzelius [Berzelius], in the same year when he also discovered elemental silicon [Engels, Nowak]. Rapidly recognized for its extreme hardness of about 9.5 on the ten point Mohs scale, silicon carbide has since then been commercialized as abrasive under the trademark Carborundum, a contraction of the words carbon and corundum (another name for alumina used as abrasive). Silicon carbide is also used for fireproof, high-temperature ceramics and resistive heating elements utilized in silicon device manufacturing. In the early years of solid state physics at the beginning of the 20^{th} century, the British physicist Round discovered that certain pieces of silicon carbide emitted light when an electric current was passed through these samples. It was also discovered that silicon carbide had rectifying properties. In spite of the comparatively high turn-on voltage, silicon carbide crystal detectors were used in the early days of radio telecommunication under its brand name Carborundum. With the emerging semiconductor technology focusing on germanium and silicon in the 1930s, silicon carbide was abandoned as semiconductor material. In the search for semiconductor materials suitable for blue light emitting diodes, silicon carbide came into focus again in the late 1970s, but it was soon replaced by direct band gap semiconductors of the III-nitride group, i.e. compounds of one

or more group III metal (Al, In, and Ga) and the group V element nitrogen. However, the advances in technology and the need for high-power electronic devices resulted in the ongoing research activity on this particular material, which led to the availability of high quality silicon carbide material and to the commercialization of silicon carbide devices in the beginning of the 21st century.

1.1 Material Properties

Silicon carbide crystallizes in the form of silicon-carbon bilayers with a bond length of d = 1.9 Å, which also is the arithmetic average between the C-C bond in diamond and the Si-Si bond in crystalline silicon. In the silicon carbide crystal lattice these bilayers are closely packed. Silicon carbide has the quite unique property of showing a large variation in crystal lattices, which are all built up by these stacked bilayers. This property is known as polytypism and is to a certain degree also observed for some III-nitride and II-VI compounds. The stacking sequence causes the presence of inequivalent hexagonal and cubic lattice sites, as shown in Fig. 1.1. The different crystal structures can be identified by their characteristic stacking sequence. Designating the layers with letters A for the base layer and B and C for the following layers, the lattice order can be written as letter sequences. In the often-used Ramsdell notation [Ramsdell], the three letters **C**, **H** and **R** are used to indicate the cubic, hexagonal and rhombohedral symmetry of the crystal lattice, following the number of layers in the stacking sequence.

Table 1.1: Physical parameters of common semiconductors at room temperature in comparison to silicon carbide. [Choyke,Pensl] [Sze] [Harris]

		Ge	Si	GaAs	3C-SiC	6H-SiC	4H-SiC	GaN	
band gap	E_g	$^{(i)}0.66$	$^{(i)}1.12$	$^{(d)}1.43$	$^{(i)}2.4$	$^{(i)}3.0$	$^{(i)}3.2$	$^{(d)}3.4$	eV
crit. field	E_c	0.1	0.25	0.3	2.0	2.5	2.2	3.3	MV/cm
mobility	μ_n	3900	1350	8500	1000	500	1000	1000	$\mathrm{cm^2/Vs}$
	μ_p	1900	480	400	40	80	120	30	$\mathrm{cm^2/Vs}$
intrinsic conc.(1)	n_i	10^{13}	10^{10}	10^{6}	10^{1}	10^{-6}	10^{-8}	10^{-9}	$\mathrm{cm^{-3}}$
permittivity	ε_r	16.0	11.9	13.1	9.7	10.0	10.0	~ 10	
therm.conduct.	κ	1.6	1.5	0.46	$\gtrsim 3.5$	$\gtrsim 3.5$	$\gtrsim 3.5$	$\gtrsim 1.6$	W/cm K
density	ρ	5.3	2.3	5.3	3.2	3.2	3.2	6.1	$\mathrm{g/cm^3}$
lattice		cubic	cubic	cubic	cubic	hexag.	hexag.	hexag.	
lattice const.	a	5.65	5.43	5.65	4.36	3.08	3.08	3.19	Å
	c	—	—	—	—	15.12	10.08	5.19	Å

(i) indirect electronic band gap (d) direct electronic band gap

(1) only given to the order of magnitude

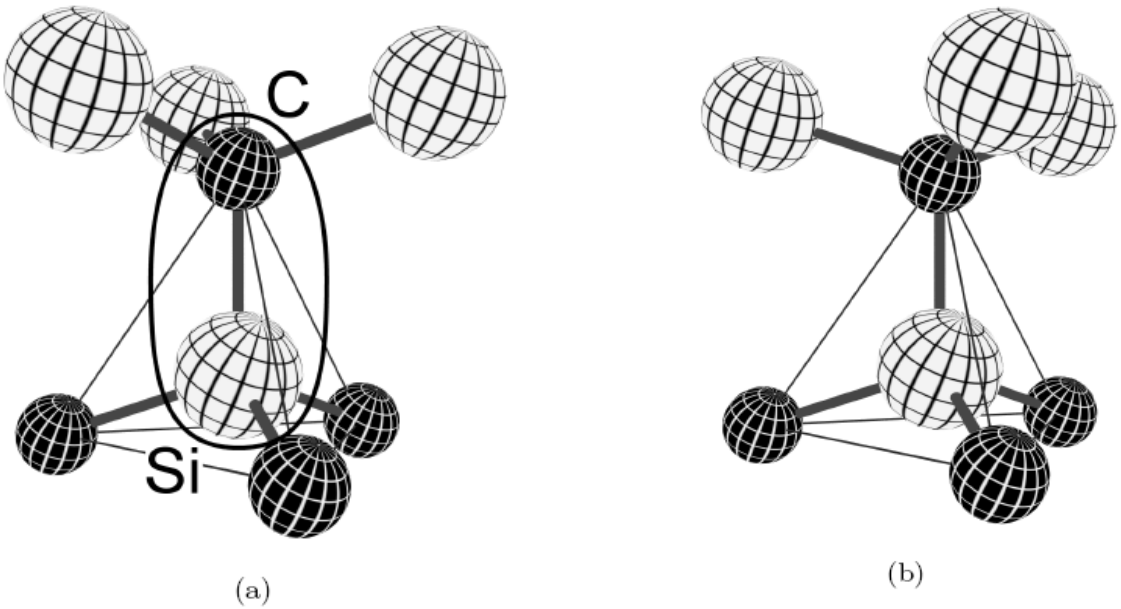

Figure 1.1: The (a) cubic and (b) hexagonal lattice site for silicon (bright spheres) and carbon atoms (dark

spheres) in the silicon carbide lattice.

2H With the stacking sequence AB this is the purely hexagonal or wurtzite structure. All lattice sites show the hexagonal symmetry (Fig. 1.1(b)). This polytype has not been of technological interest so far, because of difficulties in material growth.

3C This is the cubic zincblende structure with the stacking sequence ABC. As in semiconductors like GaAs all lattice sites show the same cubic symmetry (Fig. 1.1(a)). Since this view of the cubic lattice is unconventional, it should be pointed out that the [0001] axis in the hexagonal structure corresponds to the [111] orientation in the cubic lattice. Fig. 1.2 shows the 3C crystal lattice

4H With a macroscopic hexagonal symmetry and the stacking sequence ABAC, this is the currently most intensively studied poly-type for power electronic devices. On a microscopic scale it shows 50% cubic and 50% hexagonal lattice sites.

6H ABCACB is the stacking sequence of the first silicon carbide polytype, which was available in the form of single-crystalline wafers. Compared to the 4H polytype, 6H silicon carbide shows a more pronounced anisotropy of its material parameters. The crystal lattice contains 2/3 cubic and 1/3 hexagonal sites.

Silicon carbide polytypes containing several hundred bilayers in the stacking sequence have been identified by X-ray diffraction indicating the tendency of this material to form highly anisotropic crystals.

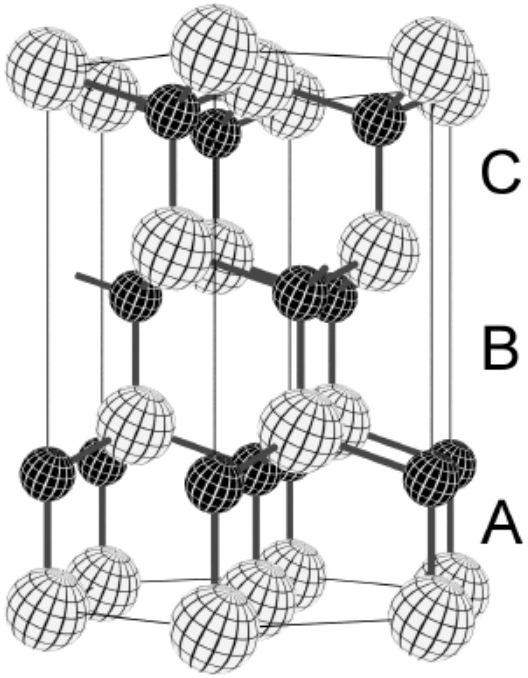

Figure 1.2: Crystal lattice of 3C silicon carbide. The lattice consists of a repetition of Si-C bilayers stacked in a ABC sequence along the crystal's [111] axis. The cubic lattice constant is a = 4.36°A.

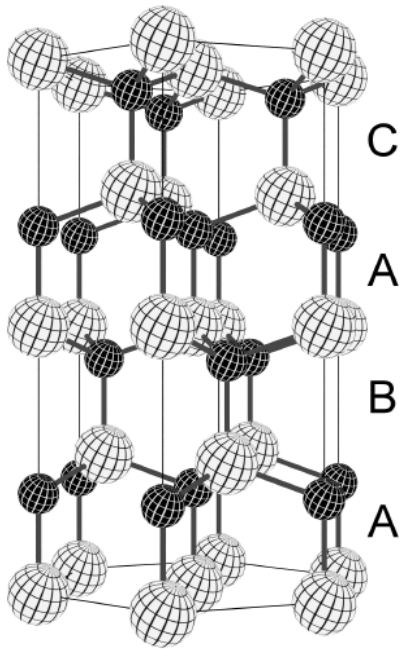

Figure 1.3: Crystal lattice of 4H silicon carbide. The lattice consists of a repetition of Si-C bilayers stacked in a ABAC sequence with lattice constants a = 3.08°A and c = 10.08°A.

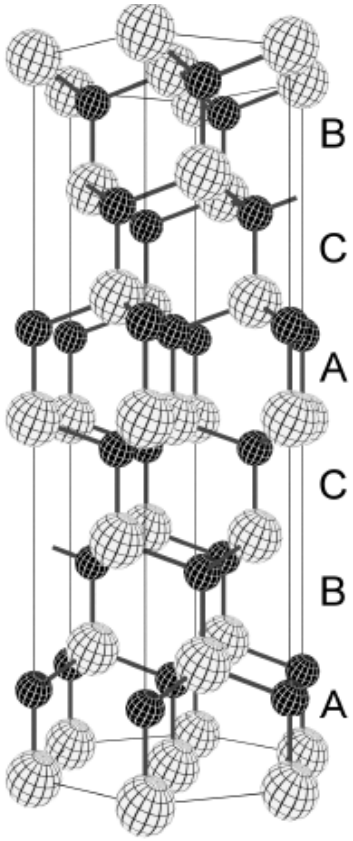

Figure 1.4: Crystal lattice of 6H silicon carbide. The lattice consists of a repetition of Si-C bilayers stacked in a ABCACB sequence with lattice constants a = 3.08°A and c = 15.12°A.

1.2 Material Growth

Unlike most other semiconductor materials of technological interest, silicon carbide does not show a liquid phase. The only way to synthesize, purify and grow silicon carbide raw material for device processing is by means of gaseous phases. Still research is carried out on the field of liquid phase epitaxy (LPE) where silicon carbide layers are deposited from a supersaturated solution of carbon in silicon or silicon and carbon in a different solvent at high temperatures, but these techniques are merely used in experimental work. Silicon carbide can be synthesized by reducing sand (SiO2) in the presence of excess carbon in electrical arc furnaces. In this

process, developed by Acheson in 1891, silicon carbide is formed as a sintered mass of small crystallites. Under certain growth conditions, larger single crystalline platelets of silicon carbide can be found in cavities and at the outer surface of the synthesized material. The commonly used techniques for the growth of electronic-grade silicon carbide are

- **Physical Vapor Transport** (PVT): a solid source of silicon carbide is evaporated at high temperatures and the vapors crystallize at a colder part of the reactor.

- **Chemical Vapor Deposition** (CVD): gas-phase silicon and carbon containing precursors react in a reactor and silicon carbide is solidified on the target.

1.2.1 BULK GROWTH

An important feature for the growth of bulk silicon carbide as base material for both silicon carbide and III-nitride based electronic and optoelectronic components, is the possibility to grow large single crystals in high quantities. This emphasizes the need for a high growth rate, which can easily be achieved by PVT techniques using either powder or polycrystalline source materials. The process is known as the modified Lely process in analogy to the method of producing larger size silicon carbide crystals by sublimation introduced by Lely in the 1950s [Lely]. In the modified Lely technique used for bulk crystal growth, a small crystal of silicon carbide in the cooler part of a cavity serves as a crystallization seed for the vapour from the evaporation of silicon carbide source material. It has been shown that this vapour mainly consists of Si, Si_2C and SiC_2. The crystal growth on the seed is depending on the reactor design and leads to a lateral and axial enlargement of the crystal boule. The focus during the recent years has been to increase the diameter of the wafers while at the same time reducing the density of extended material defects such as

micropipes and dislocations. CREE Inc. has presented in the last months the first 0-micropipes wafers [Cree catalog]. Since evaporation and growth takes place in a closed environment, precise doping control and uniformity is not easily controlled. This fact discourages the direct use of silicon carbide wafers as active parts in electronic components. Different approaches have been made to optimize the reactor design in order to provide good control of thermal gradients inside the growth chamber at temperatures in the range of 2200 − 2500 ◦C. This, in turn, leads to an improved uniformity in growth rate, less in-grown stress fields in the material and a better crystalline quality with a reduction of dislocations and other extended defects.

Table 1.2: Parameters of commercially available silicon carbide substrate wafers in 2007. Data according to the manufacturers' specifications [Cree catalog].

	n – type		p - type		Semi-insulating	
	4H-SiC	6H-SiC	4H-SiC	6H-SiC	4H-SiC	
Diameter	50.8 100	50.8	50.8 100	50.8	50.8 100	cm
Resistivity	0.015 0.028	0.040 0.090	0.015 0.028	0.040 0.090	$> 10^5$	Ωcm
Net doping conc.	9×10^{14} 1×10^{19}	9×10^{14} 1×10^{19}	9×10^{14} 1×10^{19}	9×10^{14} 1×10^{19}	N/A	cm^{-3}
Micropipe density	0 30	5 30	0 30	5 30	N/A	cm^{-2}

Silicon carbide wafers have become available from a growing number of manufacturers in the recent years [Cree_catalog] [Nippon Steel] [Okmetic] [SiCrystal] [TDI Inc.]. These are advertised by means of the parameters listed in Tab. 2.2. The Finnish/Swedish silicon carbide substrate manufacturer Okmetic AB introduced semi-insulating (SI) silicon carbide wafers cut from

CVD grown bulk crystals [Okmetic]. As opposed to SI silicon carbide from other manufacturers, where the residual doping is compensated by mid-band gap levels of extrinsic impurities (e. g. transition metals like vanadium), the new high-purity material seems to be compensated by mid-gap intrinsic defects.

1.2.2 EPITAXIAL GROWTH

Due to the above-mentioned imperfections still present in state-of-the-art silicon carbide wafers, these cannot be directly used for the active regions in electronic components. The achievable doping concentrations and inhomogeneities are generally too high, as well as the concentration of extended crystal defects. Therefore the commercially available silicon carbide wafers are mainly used as a substrate to support the epitaxially grown active layers. Epitaxy allows for a much more precise control of layer thickness, doping and homogeneity than achievable in bulk material growth. The gaseous source materials are available with a higher purity than solid silicon carbide source materials. The dopants are also provided by means of gaseous precursors, and a free control over the ratio between those different source gases determines the amount of incorporated doping impurities. The incorporation of dopants is not only controlled by the concentration of the dopant species, but also by means of a site competition affected by the Si/C ratio of the source gases. This is due to the preferential occupation of the carbon sites for donors and silicon sites for acceptors, respectively [Larkin]. Different reactor designs have been developed to increase the throughput of epitaxial growth and to improve the material properties in the epitaxial layers. Some of the special features of silicon carbide epitaxy reactors are

- **substrate rotation** the wafers are rotated during epitaxial growth to improve thickness and doping homogeneity.

- **high-temperature** a higher temperature T ≥ 1700 ◦C can result in growth rates higher than 100 µm/h.

- **vertical gas flow** improves gas flow dynamics especially at higher temperatures. The reactor design is also known as chimney reactor.

- **hot-wall/cold-wall** differ in the temperature gradients in the vicinity of the wafers. In the cold-wall design the growth chamber walls are actively cooled while the growth chamber is thermally isolated from the surrounding ambient in the hot-wall design.

When growing epitaxial layers of silicon carbide, one of the main problems to solve is the reproduction of the stacking sequence of the base material. In the hexagonal polytypes most material is grown along the c-axis with a [0001] surface. In principle both B and C orientations of the bilayers can nucleate on an atomically flat [0001] surface of an A oriented layer, but only one of these two orientations will repeat the stacking sequence of the desired polytype. Epitaxial growth on flat surfaces can therefore cause inclusions of different polytypes and twin structures into the grown layers. Using substrate materials, which are cut at small off-axis angles (typically 3.5◦ for 6H and 8◦ and 4◦ for 4H) a 1-dimensional growth along the surface steps can be achieved. This ensures the reproduction of the stacking sequence of the base material during the epitaxial growth [Kimoto]. Recently also other crystal orientations have been studied for the manufacturing of power devices. The [$11\bar{2}0$] orientation is one of the most promising in the hexagonal polytypes. This orientation offers a surface parallel to the orientation of possible micropipes and screw dislocations and these will not be reproduced from the substrate when growing corresponding epitaxial layers. Additionally, improved device performance of MOS controlled devices has been reported on [$11\bar{2}0$] oriented epitaxial layers. However, a 75% reduction in the critical electric

field for diodes on the [11$\bar{2}$0] surface compared to the [0001] surface of 4H silicon carbide has been reported by Nakamura et al. [Nakamura]. State-of-the-art commercially available epitaxial layers are still advertised with doping variations in the order of ±25% for the *n*-type and ±50% for the *p*-type and thickness variations of ±10%.

1.3 Crystal Imperfections

Deviations from the perfect crystal lattice are commonly called defects. It is important to distinguish between four major classes of defects always present in the currently available silicon carbide material:

0 dimensional point defects

"Misplaced" single atoms or smaller clusters of atoms in the lattice. These can be intrinsic point defects such as silicon and carbon vacancies and interstitials, silicon atoms on carbon lattice sites and vice versa. Also intentionally introduced dopant atoms, such as N, P, Al and B, transition metal atoms V or Ti and unintentional impurities like H or O, are point defects in the lattice.

1 dimensional dislocations

The crystal lattice is distorted along a dislocation line while the periodicity of the lattice is not affected. Dislocation lines can only be bound by larger defects, voids or inclusions in the crystal or by the crystal surface. In [0001]-oriented silicon carbide screw dislocations and threading edge dislocations parallel to the c-axis of the crystal

can penetrate whole wafers and epitaxial layers.

2 dimensional stacking faults

The periodicity of the stacking sequence is broken along a lattice plane. Below and above of this plane, the crystal shows the full periodicity of the crystal lattice of the corresponding polytype.

grain boundaries

The crystal is built up from smaller perfect crystals, which are tilted, shifted or rotated against each other. The interface between neighboring crystallites or grains forms a low-angle grain boundary.

3 dimensional polytype inclusions

Grains with the stacking sequence of a different polytype are embedded in the crystal [Si][Hallin].

1.3.1 DOPING

The bi-atomic base and the presence of inequivalent lattice sites with cubic and hexagonal symmetry give raise to different ionization energy levels of incorporated impurity atoms. From the reaction kinetics during crystal growth and dopant incorporation, and from results of different measurement techniques it was concluded that the main p-type impurities aluminum and boron are incorporated preferably on the silicon site, while the main n-type

impurity nitrogen occupies the carbon lattice site. The shallow phosphorus donor on the other hand appears to occupy the silicon lattice site [Choyke,Pensl][Larkin][Rupp]. In the case of the donor impurities a clear split in ionization energy is observed between atoms incorporated on cubic and hexagonal lattice sites, respectively. Nitrogen, the most common donor in silicon carbide, shows ionization energies of $E_C - E_N^{cub}$ = 102meV and $E_C - E_N^{hex}$ = 59 meV, respectively. Boron as common acceptor type dopant shows a deep level at $E_B^{deep} - E_V$ ' 60 meV in the band gap in addition to the shallow levels at $E_B - E_V \approx$ 300meV. During recent years aluminum with ionization energy of $E_{Al} - E_V \approx$ 200meV has become the favorite p-type dopant in silicon carbide device technology. As can be seen from the numbers above, even the shallow dopant ionization levels in silicon carbide are deep compared to dopant ionization energies in traditional semiconductors, such as silicon and gallium arsenide, and lead to an incomplete ionization of the impurity atoms at room temperature.

1.3.2 SCREW DISLOCATIONS

Screw dislocations are present in state-of-the-art silicon carbide material in densities in excess of 10^4 cm^{-2}. The dislocation line of screw dislocations can penetrate along the c-axis through the whole length of crystals grown by the modified Lely method and are thus present in all wafers subsequently cut from these crystals. Screw dislocations can only terminate at crystal surfaces and those present in the substrate wafer are there fore reproduced during subsequential epitaxial growth. During epitaxial growth additional screw dislocations can also be nucleated at inclusions and voids formed inside the epitaxial layer [Kuhr][Sanchez]. The amount of distortion along the direction of the dislocation line is given by the length of the Burgers vector B. In the case of pure screw dislocations the Burgers vector is parallel to the *c*-axis of the silicon carbide crystal and the length of the Burgers vector corresponds to

the step height of the screw dislocation. Screw dislocations in silicon carbide crystals have been observed with Burgers vectors ranging from B = 1*c* up to several 10*c*. It was found that all screw dislocations with B ≥ 3*c* form an open core or a pinhole along the dislocation line. This is explained by the surface free energy according to Frank's theory [Si][Frank][Vetter]. Screw dislocations with hollow core are called micropipes. Along with the progress in material growth, the densities of micropipes has been reduced by at least two orders of magnitude during recent years, due to a massive research effort, achieving to grow micropipe-free epitaxial layer. However, the disappearance of micropipes revealed the influence of other crystal defects, such as the close-core screw dislocations with B ≤ 2*c*, on device performance [Zimmermann01][Neudeck][Neudeck2].

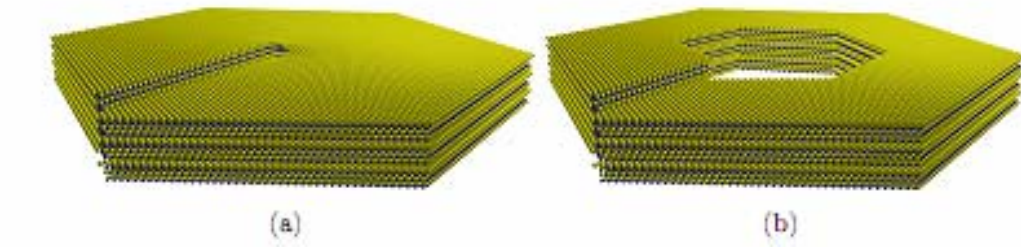

Figure 1.5: Illustration of (a) a closed-core and (b) an open-core screw dislocation with a Burgers vector B = 1c in the crystal lattice of 4H silicon carbide.

1.3.4 STACKING FAULTS

Recently the presence of stacking faults in the active volume of silicon carbide devices has attracted the attention of a number of research institutes worldwide. It was observed that an increase in the forward voltage drop and thus in the power loss of *p/n* diodes was correlated with the appearance of stacking faults in the hexagonal stacking sequence of the typically used 4H silicon carbide. Calculations have shown [Lindefelt] that the stacking fault can form a 2-dimensional quantum well, reducing the effective carrier

lifetimes in the active region. Stacking faults can be introduced into the epitaxial silicon carbide layers during growth, where they originate at imperfections at the substrate-epilayer interface, during oxidation [Okojie] and during device operation in the presence of dense electron-hole plasmas in the drift region of bipolar devices. A correlation between in-grown stacking faults and long, straight lines or edges observed on the surface of the epitaxial layer has been proposed, based on electrical, photoluminescence and SEM measurements [Zimmermann02]. Fig. 1.6 illustrates the position of a stacking fault in a 4H-silicon carbide layer with the typical 8◦ off-axis orientation used for step-controlled epitaxy. The stacking fault area is formed between the leading partial dislocations and the trailing partial dislocation. In the Figure the trailing partial is located at the sample surface, while the leading partial dislocations are extending into the epitaxial layer. The results presented indicate that stacking faults with a similar structure can cause a contrast in a scanning electron microscope, which is probably caused by the accumulation of charge carriers in the area of the stacking fault [Zimmermann02].

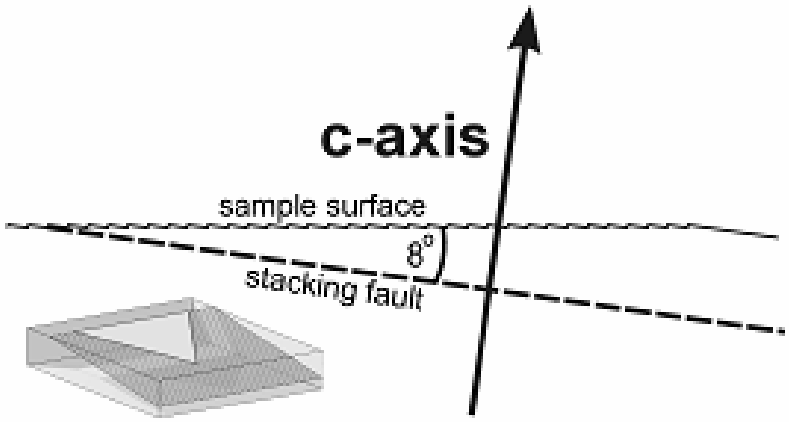

Figure 1.6: Schematic cross-section through an 8◦ off-axis oriented epitaxial silicon carbide layer with a stacking fault originating from the sample surface. The stacking fault terminates with the trailing partial dislocation at a surface terrace. The leading partial dislocations extend into the epitaxial layer and the stacking fault is formed in between.

Bibliography

[Berzelius] J. J. Berzelius: Annalen der Physik 1, p. 169 (1824)

[Engels, Nowak] S. Engels and A. Nowak: Auf der Spur der Elemente (VEB DeutscherVerlag fur Grundstoffindustrie, Leipzig, 1982), 3rd edn.

[Choyke, Pensl] W. J. Choyke and G. Pensl: Mater. Res. Bull. 22, pp. 25–29 (1997)

[Sze] S. M. Sze: Physics of Semiconductor Devices (John Wiley and Sons, New York, 1981)

[Harris] G. L. Harris (ed.): Properties of Silicon Carbide (Inspec/IEE, 1995)

[Ramsdell] L. S. Ramsdell: Amer. Mineral. 32, pp. 64–82 (1947)

[Selvam] A. Selvam, N. Nair, and P. Singh: Journal of Materials Science Letters 17, pp. 57–60 (1998)

[Lely] J. A. Lely: Berichte der Deutschen Keramischen Gesellschaft 32, p. 229 (1955)

[Cree catalog] Cree Inc, http://www.cree.com/products/pdf/MAT-CATALOG.00K.pdf

[Nippon Steel] Nippon Steel, http://www.nsc.co.jp/english/index.html

[Okmetic] Okmetic, http://www.okmetic.com/

[SiCrystal] SiCrystal, http://www.sicrystal.de/products.html

[TDI Inc.] TDI Inc., http://www.tdii.com/products/SiC_epi.html

[Larkin] D. Larkin: Phys. Stat. Sol. B 202, pp. 305–320 (1997)

[Kimoto] T. Kimoto, A. Itoh, and H. Matsunami: Physica Status Solidi B 202, pp.247–62 (1997)

[Nakamura] S.I. Nakamura, H. Kumagai, T. Kimoto, and H. Matsunami: Appl. Phys. Lett. 80, pp. 3355–3357 (2002)

[Si] W. Si, M. Dudley, H.-S. Kong, J. Sumakeris, and C. Carter: J. Electron. Mater. 26, pp. 151–159 (1997)

[Hallin] C. Hallin, A. Konstantinov, B. Pecz, O. Kordina, and E. Janzen: Diamond and Related Materials 6, pp. 1297–300 (Aug 1997)

[Rupp] R. Rupp, Y. Makarov, H. Behner, and A. Wiedenhofer: Phys. Stat. Sol. B
202, pp. 281–304 (1997)

[Kuhr] T. Kuhr, E. Sanchez, M. Skowronski, W. Vetter, and M. Dudley: J. Appl. Phys. 89, pp. 4625–30 (15 April 2001)

[Sanchez] E. Sanchez, S. Ha, J. Grim, M. Skowronski, W. Vetter, M. Dudley, R. Bertke, and W. Mitchel: J. Electrochem. Soc. 149, pp. G131–6 (2002)

[Frank] F. C. Frank: Acta Cryst. 4, p. 497 (1951)

[Vetter] W. Vetter and M. Dudley: J. Mater. Res. 15, pp. 1649–52 (Aug 2000)

[Neudeck] P. G. Neudeck, W. Huang, and M. Dudley: IEEE Trans. Electron Devices 46, pp. 478–484 (1999)

[Neudeck2] P. G. Neudeck and C. Fazi: IEEE Trans. Electron Devices 46, pp. 485–492 (1999)

[Lindefelt] U. Lindefelt, H. Iwata, S. Oberg, and P. Briddon: Mater. Sci. Forum (2002)

[Okojie] R. Okojie, M. Xhang, P. Pirouz, S. Tumakha, G. Jessen, and L. Brillson: Mater. Sci. Forum 389-393, pp. 451–4 (2002)

[Zimmermann01] U. Zimmermann, J. Osterman, D. Kuylenstierna, A. Hallen, W. Vetter and Dudley: JAP 93 (2003) pp. 611–618

[Zimmermann02] U. Zimmermann, J. Osterman, A. Galeckas, A Hallen: Mater. Sci. Forum (2003)

Chapter 2: Silicon Carbide Particle Detector.

Introduction

Radiation damage can affect various properties of a detector. Phenomena connected with the alteration of these properties are the increase of the leakage current, the decrease of charge collection efficiency (CCE) and the removal of free carriers from the conductive regions of the device. Radiation hardness is the inertness of these device parameters to high doses of particle irradiation. [Lebedev1]

SiC, due to its wide gap and strength of its chemical bonds, has been seriously considered as a valid alternative to silicon for the production of radiation hard ionizing particle detectors. An important driving force for the development of SiC-based detectors has come from the construction of the large hadron collider (LHC) at CERN in Geneva. The collaboration CERN RD-50 aims to the development of detectors able to withstand the higher irradiation fluences that will affect them: a large amount of research is made for the improvement of silicon-based detectors, but also the possibility of using new materials, as SiC or GaN, is investigated [Bruzzi05] [Sellin06].Our group at the University of Bologna is currently involved in this collaboration, and our contributions span from the characterization of the radiation hardness of several SiC detector schemes to the study of the defects introduced by irradiation by means of DLTS and other experimental techniques.

The usual design of a detector includes a *p+/n*, *n+/p* or a *p+/ i /n+* diode structure or metal-semiconductor barriers, operating under reverse bias. Figure [2.1] shows the cross section of a *p+/ i /n+* and the reverse biased detector band diagram.

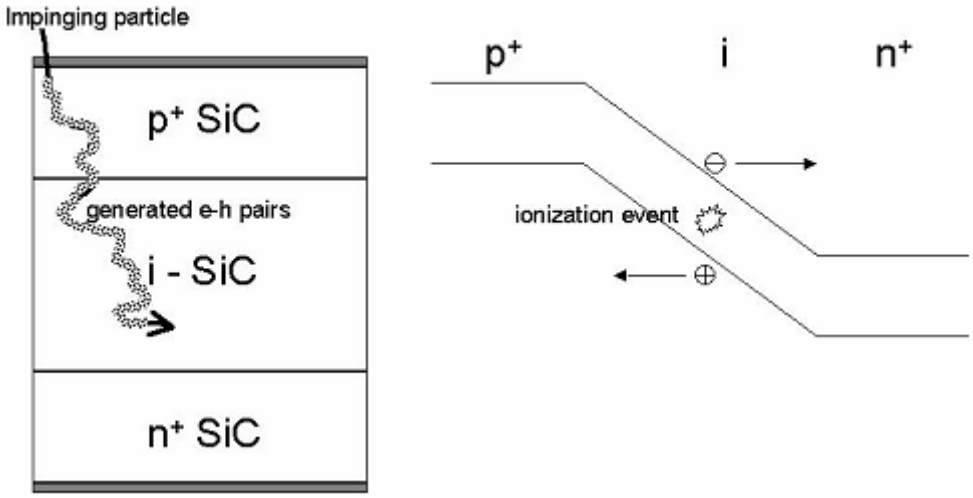

Figure 2.1 a) Cross Section for a typical SiC detector

b) Band Structure of reverse biased detector, during the a detection event.

A space charge region is formed, and the p+ and n+ regions act as electrodes. Ionizing particles produce ionization in a semiconductor when they are slowed down or absorbed. Thus, electron-hole pairs are formed, which are then separated by the electric field and collected at the electrodes, yielding a current pulse in the detection circuit. The current generated is well correlated with the impinging particle energy.

A detector should have a low concentration of impurities and defects, because these cause a diminution in the current pulse amplitude due to recombination of electron-hole pairs and scattering of charge carriers. Moreover, a low concentration of dopant impurities extends the thickness of the space charge region, i.e. the detection active region.

The wide bandgap is useful, as it reduces significantly the rate of thermally generated charge carriers raising the noise level. On the other hand, it also represents a disadvantage: a particle with certain energy, ideally transforming all its energy for the generation of electron-hole pairs, generates 3 times more particles in Si than in SiC. Detectors based on SiC, therefore, have lower pulse amplitudes. However, for low signals, the reduction of the noise level is

more important than the reduction of the signal level, so that the overall signal-to-noise ratio (SNR) is improved for SiC-based detectors. Furthermore, SiC-based detectors still have a high SNR at temperatures which are unattainable for Si-based devices, needing external cooling to keep the intrinsic carrier level sufficiently low [Lebedev02].

2.1 Semiconductor junctions

Apart from being one of the simplest semiconductor device to study, the junction between two different materials is also the basic building block of all other semiconductor devices. Several possible material combinations can form electrically active junctions, and these can roughly be grouped into two classes:

- **Metal-Semiconductor** Whenever a metal contact is attached to a semiconductor this type of junction is formed. The physical parameters of the metal and the semiconductor determine the characteristics of this junction. Most important types are ohmic contacts and Schottky junctions.

- **Homojunctions** Two pieces of the same semiconductor material but with different doping type and/or concentration are in metallurgical contact to each other. The most important type is the *p/n* junction.

Here the basic principles of the device electrical behavior will be presented, starting from the ideal rectifier to the real device.
The ideal rectifier would allow current transport without loss in one direction while it would impose an infinite resistance on the current in the reverse direction. In the real device performance is limited by the physics of carrier transport over a potential barrier at the junction. This leads to the well known equation for the current I through an ideal diode

(2.1) $$I = J \cdot A = I_0\left(e^{qV/\eta k_B T} - 1\right)$$

Where J is the current density, A the cross-sectional area of the diode, I_0 is the reverse leakage or saturation current, q is the elementary charge, K_B the Boltzmann constant, T the junction temperature and V is the applied bias voltage over the diode. The ideality factor η is characteristic for the carrier transport mechanism in the diode.

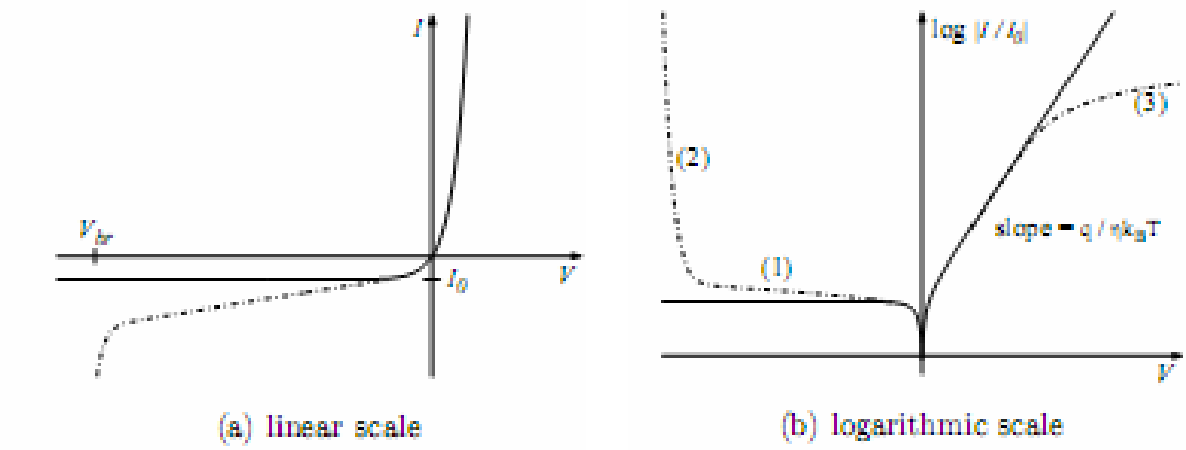

Figure 2.2: Current-voltage characteristic of a rectifying semiconductor junction. The solid line shows the ideal diode equation while the dashed line indicates deviations from the ideal diode equation, such as (1) increased leakage currents, (2) electrical breakdown and (3) series resistance.

This current-voltage (I-V) characteristic is plotted in Fig. 2.2 together with the deviations commonly observed in the reverse characteristics of real diodes, namely increased, voltage-dependent leakage currents and electrical breakdown at a certain reverse voltage V_{BR}. At forward voltages significantly higher than the thermal voltage k_BT/q Eq. 2.1 can be simplified to

(2.2) $$I = I_0 \cdot e^{qV/\eta k_B T}$$

For higher forward currents deviations from the ideal diode characteristic are observed as an additional voltage drop over the device. Depending on the design of the diode the major contribution to this voltage drop is normally found in the series resistance R_s of the neutral regions of the semiconductor and the diode equation can then be written as

$$I = I_0 \cdot e^{(qV - IRs)/\eta k_B T} \tag{2.2}$$

The series resistance of the neutral semiconductor regions depends on the carrier mobilities $\mu_{n,p}$ and the carrier concentrations n, p

$$R_s = \frac{l}{A} \cdot \rho_S = \frac{l}{A} \cdot \frac{1}{(n\mu_n + p\mu_p)} \tag{2.3}$$

Where l is the length of the resistive region in question, which can be the low doped drift region of a pin diode, the substrate wafer and the emitter regions on either side of the junction. In a full rectifier device, additional resistive contributions from the contact regions have to be accounted for, as well.

2.2 Schottky Diodes

When a metal contact is applied to an *n*-type doped semiconductor, the Fermi level in the semiconductor lines up with the Fermi level in the metal. This leads to the band structure shown in Fig. 2.3 and the formation of a barrier Φ_B for electrons from the *n*-type semiconductor towards the metal contact

$$\Phi_B = \Phi_M - \chi_S \tag{2.4}$$

defined by the metal work function Φ_m and the electron affinity χ_s of the semiconductor. On the semiconductor side of the junction a depletion region is formed balancing the built-in potential Φ_{bi} (also referred to as the built-in voltage V_{bi}) of the junction

$$\Phi_{bi} = \Phi_B - \frac{E_C - E_F}{q} \tag{2.5}$$

The width w of the depletion region with an external bias V is given by the doping concentration N_D and the permittivity $\varepsilon_0\varepsilon_r$ of the semiconductor:

$$w = \sqrt{\frac{2\varepsilon_0\varepsilon_r(\Phi_{bi} - V)}{qN_D}} \tag{2.6}$$

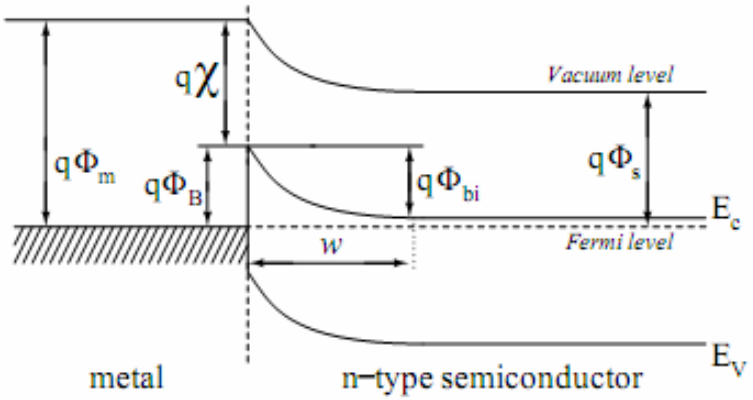

Figure 2.3: Band structure at a Schottky contact between a metal and an *n*-type semiconductor at thermal equilibrium. Φ_M is the metal work function, Φ_s the semiconductor work function, χ_s the electron affinity of the semiconductor,Φ_B the barrier height, Φ_{bi} is the build-in potential and *w* the depletion width of the junction.

2.2.1 FORWARD OPERATION

In the case of moderately or low doped semiconductors the current transport through the Schottky junction is dominated by emission of majority carriers

over the potential barrier from the semiconductor into the metal contact. If the Schottky barrier is significantly higher than the thermal energy $q\Phi_B >> k_BT$, the thermionic emission-diffusion theory describes the current-voltage characteristic of the Schottky junction as

(2.7) $$J = J_S\left(e^{qV/k_BT} - 1\right)$$

Where V is the applied voltage and J_s is the saturation current density

(2.8) $$J_S = A^*T^2e^{-q\Phi_B/k_BT}$$

The effective Richardson constant A^* is proportional to the effective mass of the majority carriers m^*

(2.9) $$A^* = \frac{4\pi q m^* K_B^{\ 2}}{h^3}$$

As can be seen the current-voltage characteristic of the thermionic emission-diffusion theory has the form of the ideal diode equation from Eq. 2.1 with $I_0 = I_s$ and an ideality factor η = 1.0. This behavior is also consistent with measurements on Schottky diodes on n-type silicon carbide as presented in Ref. [Zimmerman].

According to the thermionic emission theory, the characteristic parameter of a Schottky contact, the barrier height Φ_B, does only influence the saturation current J_s (Eq.2.8). Diodes with different barrier heights are therefore shifted along the ordinate in a semilogarithmic plot, such as Fig. 2.2(b). In a real Schottky diode the thermionic emission theory does only describe the forward current-voltage characteristic for a certain range of current densities. At higher diode currents the additional voltage drop over the quasi-neutral

regions of the semiconductor and in the metal contact therefore it plays an important role. In this case Eq. 2.2 applies as

$$I = A \cdot J_s \cdot e^{(qV - IRs)/\eta k_B T} \tag{2.10}$$

Where A is the area of the Schottky contact.

2.2.2 REVERSE OPERATION

The thermionic emission-diffusion theory predicts a constant leakage current density for a reverse biased Schottky diode of the same size as the saturation current density

$$J = -J_s = -A^* T^2 \cdot e^{-q\Phi_B / k_B T} \tag{2.10}$$

Experiments, however, show a significant increase of several orders of magnitude in the leakage current at increasing reverse bias, as plotted in Fig. 2.4.

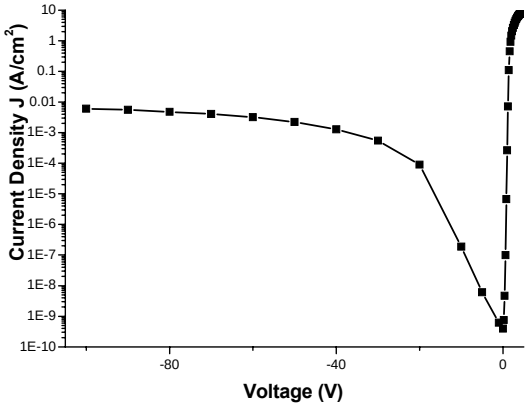

Figure 2.4 Reverse characteristic of a Schottky diode analyzed in this work

Three major contributions to the leakage current not accounted for by the thermionic theory are

1. **Image force lowering** of the Schottky barrier. The electrostatic attraction between a carrier on the semiconductor side of the junction and the induced mirror charge in the metal side of the junction leads to a lowering of the effective barrier height for the electron

(2.11) $$\Delta\Phi_B = \sqrt{\frac{2qN_D E_{MAX}}{\varepsilon_0 \varepsilon_r}}$$

Where E_{MAX} is the peak electric field at the Schottky contact

(2.12) $$E_{MAX} = \sqrt{\frac{2qN_D(-V)}{\varepsilon_0 \varepsilon_r}}$$

for applied voltages V significantly higher than the built in potential $|V| >> \Phi_{bi}$. In order to take the barrier lowering into account Eq. 2.10 can be rewritten to

(2.13) $$J_{\Delta\Phi}(V) = -A^* T^2 \cdot e^{-q\Phi_B/k_B T} \cdot e^{q\Delta\Phi_B/k_B T}$$

2. **Space charge generation** of electron-hole pairs in the depletion region. At a generation rate U, related to the carrier emission from deep levels with capture cross sections $\sigma_{n,p}$ and energy positions E_t in the bandgap, an emission time constant τ_e can be defined [SZE]

(2.14) $$U = \left[\frac{\sigma_p \sigma_n v_{th} N_t}{\sigma_n \exp\left(\frac{E_t - E_i}{k_B T}\right) + \sigma_p \exp\left(\frac{E_i - E_t}{k_B T}\right)} \right] \cdot n_i \equiv -\frac{n_i}{\tau_e}$$

E_i and n_i are the intrinsic Fermi level and carrier concentration, respectively, v_{th} is the thermal velocity. The generation related contribution to the leakage current becomes

(2.15) $$J = \int_0^w q|U|dx = \frac{qn_i w}{\tau_e}$$

Where w is the voltage V dependent width of the depletion region, described by Eq. 2.6.

3. **Tunneling currents** through the potential barrier. For high doping concentrations in the semiconductor material, the width w of the depletion region decreases (Eq. 2.6) and the probability of direct tunneling of carriers through the barrier increases. At doping concentrations above a certain value (typically $N_{A,D} >> 10^{18}$ cm^{-3}), the tunneling current is

(2.16) $$J_{\Delta\Phi}(V) \propto e^{-q\Phi_B/E_{00}}$$

With the characteristic energy E_{00}

(2.17) $$E_{00} = \frac{q\hbar}{2}\sqrt{\frac{qN_D}{\varepsilon_0\varepsilon_r m^*}}$$

Dominates the carrier transport through the contact. This allows the formation of non-rectifying, ohmic contacts to highly doped semiconductor regions

Additional effects have to be taken into account to explain increased leakage currents observed below the avalanche breakdown voltage. Examples of such effects are thermionic field emission and field emission, multiplication of carriers, crystal defects and barrier inhomogeneities.

2.3 *p / n* junctions

When the metal contact in a Schottky diode is replaced by a semiconductor region of opposite doping than the base material, a *p/n* junction is formed as shown in Fig. 2.5. The principle of the junction formation is similar to the one discussed earlier for the metal-semiconductor junction in Section 2.2. The Fermi levels E_{Fn} and E_{Fp} in the two semiconductor materials line up and a barrier with the built-in potential Φ_{bi} is formed [Neudek]

(2.18) $$E_{Fn} - E_i = k_B T \ln\left(\frac{n_{no}}{n_i}\right)$$

(2.19) $$E_i - E_{Fp} = k_B T \ln\left(\frac{n_{po}}{n_i}\right)$$

Assuming full ionization of the dopant atoms $n_{n0} = N_D$, $p_{p0} = N_A$ on either side of the junction the built-in potential is given as

(2.20) $$q\Phi_{bi} = \left(E_i - E_{Fp}\right) - \left(E_{Fn} - E_i\right) = k_B T \ln\left(\frac{N_A N_D}{n_i^{\,2}}\right)$$

E_i is the intrinsic level and n_i the intrinsic carrier concentration of the semiconductor material

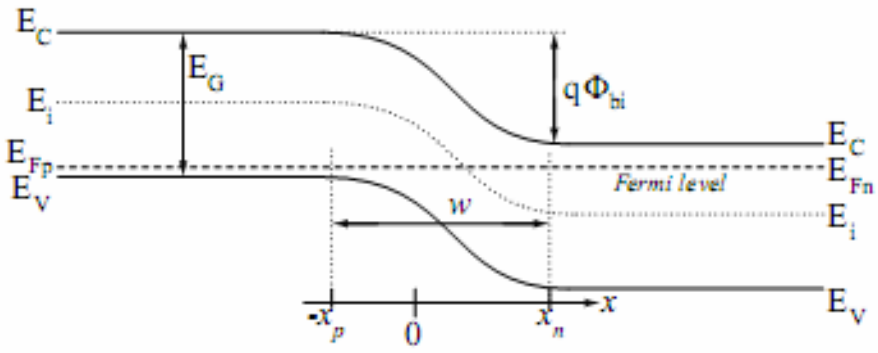

Figure 2.5: Band structure of a *p/n* diode in thermal equilibrium without external bias. E_C is the conduction band edge, E_V is the valence band edge, E_i the intrinsic Fermi level of the semiconductor. *w* is the width of the depletion region formed by the built-in potential Φ_{bi}.

Particle detector, as explained in the before, most often utilize an asymmetric doping profile at the *p/n* junction. The lower doped side will support the applied voltage under reverse operation. The electrical contact to the low-doped region is made through an additional layer of highly doped material of the same type, resulting in either one of the following structures:

p / i / n The low-doped part consists of intrinsic i.e. essentially undoped material, which will be fully depleted at low reverse voltages. These diodes are mainly used as detectors for particles and electromagnetic radiation. The term pin diode is often used to address the whole family of designs.

p+ / n / n+ The low-doped or drift region in these diode is of *n*-type. Since the series resistance of a diode is determined by the carrier mobility and doping concentration, it is advantageous to use *n*-type drift regions because of the higher electron mobility in all common semiconductors .

n+ / p / p+ The drift region in these diode is p-type doped. Due to their higher majority carrier mobilities and resulting lower

series resistance, *n* drift zones are more widely used than *p* layers. In the recent discussion about degradation phenomena in silicon carbide diodes the *p*-type drift regions might attract new interest in the field of power rectifiers due to absence of forward bias degradation.

2.3.1 FORWARD OPERATION

Considering the electron and hole current densities through the junction

(2.21) $$J_n\left(x=-x_P\right)=\frac{qD_n n_{p0}}{L_n}\left(e^{qV/k_BT}-1\right)$$

(2.22) $$J_p\left(x=-x_P\right)=\frac{qD_p p_{n0}}{L_p}\left(e^{qV/k_BT}-1\right)$$

where $-x_p$ and x_n mark the edges of the depletion region, leads to the diode equation for the ideal *p/n* junction

(2.23) $$I=A\left(J_n+J_p\right)=I_o\left(e^{qV/k_BT}-1\right)$$

Which corresponds to the characteristic of the ideal diode in Eq. 2.1 with an ideality factor $\eta = 1$. The saturation current in the case of the *p/n* junction consists of the minority carrier currents

(2.24) $$I_0=qA\left(\frac{D_n}{L_n}n_{p0}+\frac{D_p}{L_p}p_{n0}\right)$$

Where $D_{n,p}$ are the diffusion constants, Ln,p are the minority carrier diffusion lengths for electrons and holes, respectively. n_{p0} and p_{n0} are the equilibrium minority carrier concentrations. Since the minority carrier concentration is higher in semiconductor materials with lower doping levels,

(2.25) $$n_{p0} = \frac{n_i^2}{p_{p0}} \qquad p_{n0} = \frac{n_i^2}{n_{n0}}$$

The lower-doped side of an asymmetric *p/n* junction determines the saturation current of the junction. As described in the case of Schottky diodes, generation and recombination in the space charge region also contribute to the diode current. These currents are caused by recombination centers with an energy located deeply in the band gap and add to the general diode current

(2.26) $$I = I_0\left(e^{qV/k_BT} - 1\right) + \frac{qAn_i}{2\tau_e}\left(e^{qV/2k_BT} - 1\right)$$

When the measured diode current-voltage characteristics are plotted on a semilogarithmic scale, the generation-recombination currents can be seen as a slope $q/\eta k_BT$ with an ideality factor of $\eta = 2$.

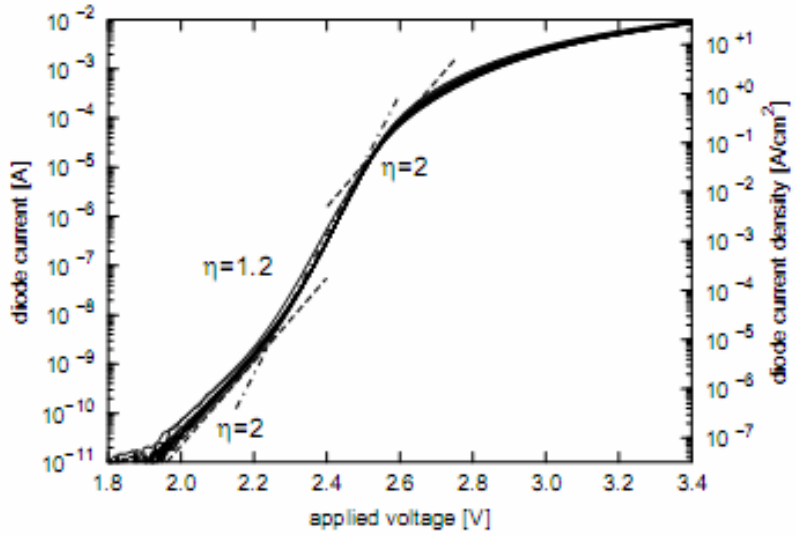

Figure 2.6: Current-voltage characteristics of a *p/n* diode. Four different regions can be distinguished by the slope of the curves, indicating different conduction mechanisms.

For higher voltages the curve shows a smaller ideality factor in the order of $1.0 \leq \eta \leq 2.0$ before the high-injection regime is reached. This tendency can also be seen when plotting the differential ideality factor

$$\eta = \frac{q}{k_B T} \frac{1}{d(\ln(I))/dV} \tag{2.27}$$

The deviation from the theoretically predicted ideality factor of $\eta = 1.0$ can be explained by a generalized form of the Schottky-Noice-Sah theory [Estropov] for the current transport through a junction. In this theory the current transport is explained by means of carrier recombination through multiple deep and shallow levels in the band gap. The theory predicts an ideality factor of

$$\eta = \frac{2d + s}{d + s} \tag{2.28}$$

Where s is the number of discrete shallow levels and d is the number of discrete deep levels in the band gap, participating in the recombination process. According to this theory the often observed ideality factor of $\eta = 1.2 = 6/5$ in silicon carbide *p/n* junctions would thus be caused by the participation of $d = 1$ deep and $s = 4$ shallow levels in the bandgap [Anikin01][Anikin02].

2.3.2 REVERSE OPERATION

The reverse leakage current of *p/n* junctions is generally dominated by space-charge generation currents caused by the same mechanisms, as described by Eq. 2.26. Fig. 2.6 shows the depletion region of a *p+/n* junction under reverse bias. The maximum of the electric field E_{max} is found at the location of the metallurgical junction between the *n*- and *p*-type semiconductor. The depletion region extends a distance $x_{n,p}$ into both sides of the junction

$$x_p = -E_{\max}\frac{\varepsilon_0\varepsilon_r}{qN_A} \qquad x_n = -E_{\max}\frac{\varepsilon_0\varepsilon_r}{qN_D} \tag{2.29}$$

under the assumption of the depletion approximation [57]. In the case of an asymmetric *p+/n* junction with $N_A >> N_D$ the extension of the depletion region into the highly doped *p*-type anode can be neglected and the highest electric field is found at the metallurgical junction.

$$E_{MAX} = \sqrt{\frac{2qN_D}{\varepsilon_0\varepsilon_r}|V|} \tag{2.30}$$

The carriers of the leakage current are accelerated by the electric field in the depletion region. When a carrier gains sufficient kinetic energy it can create an electron-hole pair by the impact ionization. Both electrons and the hole in turn are accelerated in the electric field and can create additional carrier pairs as depicted in Fig. 2.7.

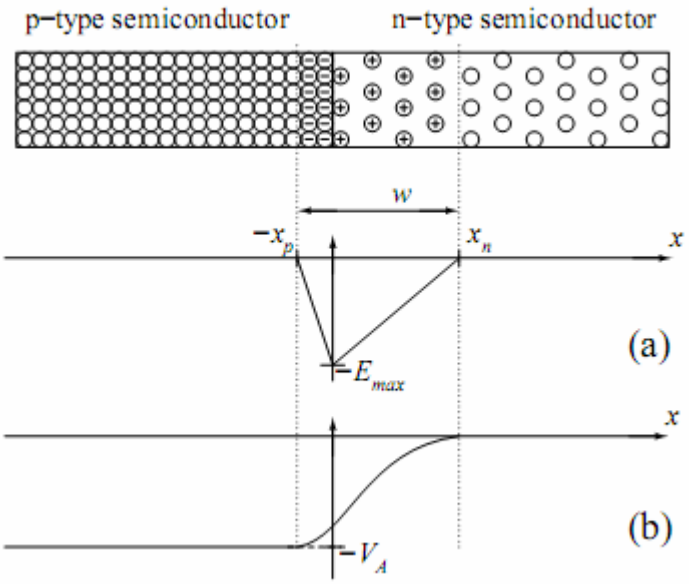

Figure 2.7: Depletion region in a reverse biased *p+/n* junction. The charged dopant atoms on both sides of the junction balance each other. Graph (a) shows the electric field and (b) the potential along the diode.

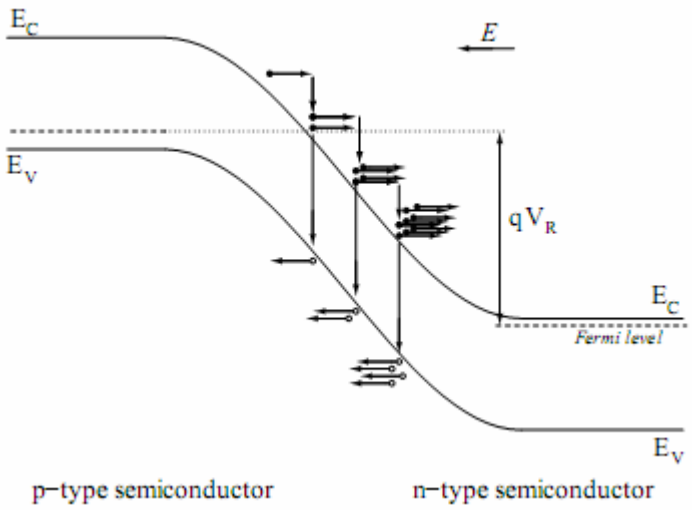

Figure 2.8: Band structure of a reverse biased *p/n* diode. Avalanche multiplication at breakdown is schematically shown for electrons generating additional electron-hole pairs on their way through the depletion region.

2.4 Junction Edge Terminations

This chapter has so far only considered one-dimensional structures where the electric field vector was perpendicular to the sample surface. In real devices, however, the junction shows curvatures and the device geometry shows edges and surfaces, where the peak electric field will be increased due to field crowding. Since the breakdown voltage of a device is closely related to the maximum electric field at the junction of the device, areas of increased electric field will significantly reduce the ability of power devices to withstand and block high reverse voltages. Electrical breakdown will preferably occur at the periphery of the three-dimensional junction if the maximum field in these areas is not reduced by proper edge termination techniques.

2.4.1 JUNCTION TERMINATING EXTENTION

Another approach to reduce the electric field at the junction edge by widening the depletion region and thus avoid the effect of field crowding is called junction termination extension (JTE). This is especially suitable for implanted junctions with small radii of curvature at the implantation edges. In a JTE the device is surrounded by implanted areas of the same doping type as the main junction but at lower concentrations (Fig. 2.9). All JTE zones are in electrical contact to each other and to the main junction. The JTE region should be completely depleted at the theoretical bulk breakdown voltage of the main junction in order to stretch the depletion region along the surface. Computer simulations can be used to find an optimal design depending on the semiconductor material parameters and the doping concentrations of the low-doped drift zone.

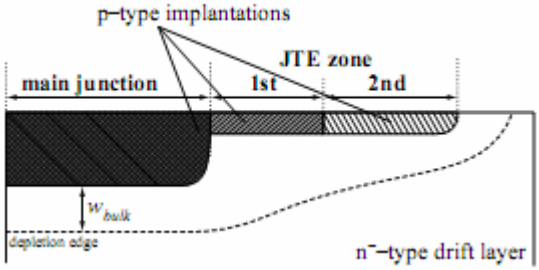

Figure 2.9: Schematic cross-section through a diode with junction termination extension implantations.

2.4.2 FIELD RING

If the diode is surrounded by isolated rings of the same doping type as the main junction the depletion region will also extend further at the surface than in the bulk, effectively lowering the electric field in the edge region of the junction. This is schematically shown in Fig. 2.10. By optimizing the field-ring width and spacing around the junction, bulk breakdown can be reached [Baliga]. In contrast to JTE structures, all field-rings can be implanted simultaneously together with the main junction. This fact eases the implementation of field ring termination into the process flow.

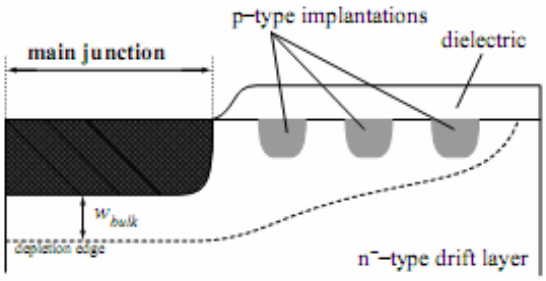

Figure 2.10: Schematic cross-section through a diode with field-ring edge termination.

2.5 Current-Voltage and Activation-Energy Measurements Set-up

The Current-Voltage characterization has been performed with a Keithley 6517 Electrometer; this instrument works as voltage source and as amperometer either. The maximum sensitivity of the amperometer is 0.1 pA. The system has been interfaced to a personal computer through a GPIB board. Visual Basic software controls some parameters of the measurement:

- The starting and the final voltage V_i, V_f
- The voltage step ΔV
- The time between the setting of the polarization and the current value reading t_V

The temperature is monitored by a Lakeshore 330 temperature controller with a K-type thermocouple with a sensitivity of 0.1 K. The activation-energy measurements employ the same equipments of the I-V characteristics, only the software that controls the measurement, is different. In this case the software controls, through the Lakeshore Temperature controller, the temperature rising ramp, and it reads the values of the sample current at different temperature by means of the electrometer. The voltage source is used to bias the sample with a constant polarization. To rise the temperature is used a Joule-effect heater, with a 50 Ω resistor and a maximum current of 1 A. The controlled parameters, in this case, are:

- The temperature range T_i, T_f
- The temperature step ΔT
- The constant bias voltage V_R

In Figure 4.1 is shown the block diagram for these measurements

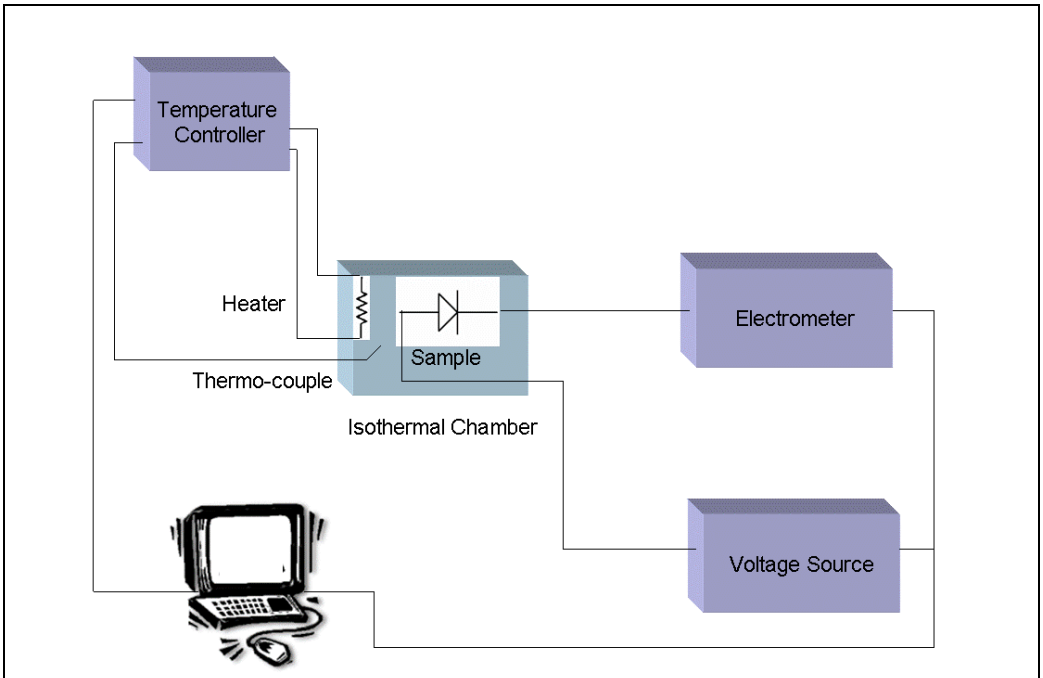

Figure 2.11 Block diagram for I-V characterization and activation-energy measurements

Bibliography

[Lebedev1] A.A. Lebedev, V.V. Kozlovski, N.B. Strokan, D.V. Davydov, A.M. Ivanov, A.M. Strel'chuk and R. Yakimowa, Fiz. Tekh. Poluprovodnikov 36, 1354 (2002)

[Bruzzi] M. Bruzzi et al., Nucl. Instr. And Meth. In Phys. Res. A 541, (2005)

[Sellin] P.J. Sellin, J. Vaitkus, Nucl. Instr. and Meth. in Phys. Res. A 557, 479 (2006)

[Lebedev2] A.A. Lebedev, A.M. Ivanov, N.B. Strokan, Fiz. Tekh. Poluprovodnikov 38, 129 (2004)

[Zimmerman] U. Zimmerman, A. Hallen, J. Osterman, E. Danielsson, D. Kuylenstierna, and B. Breitholtz: in Workshop Microtechnology and Thermal Problems in Electronics, Microtherm 2000 (edited by M. Langer, Z. Lisik, and J. Podgorski) (Technical University of Lodz, Lodz, Poland, 2000), pp. 146–151

[Sze] S.M. Sze, Physics of semiconductor devices (Wiley Interscience, 1981)

[Neudek] G. W. Neudeck: The PN Junction Diode, vol. 2 of Modular series on solid state devices (Addison-Wesley Publishing Inc., Reading, Massachusetts, 1983), ISBN 0-201-05321-7

[Estropov] V. V. Evstropov, K. V. Kiselev, P. I. L., and B. V. Tsarenkov: Sov. Phys. Semicond. 18, pp. 1156–1172 (1984)

[Anikin01] M. M. Anikin, V. V. Evstropov, I. V. Popov, V. N. Rastegaev, A. M. Strel'chuk, and A. L. Syrkin: Sov. Phys. Semicond. 23, pp. 405–407 (1989)

[Anikin02] M. M. Anikin, V. V. Evstropov, I. V. Popov, A. M. Strel'chuk, and A. L. Syrkin: Sov. Phys. Semicond. 23, pp. 1122–1125 (1989)

[Baliga] B. J. Baliga: Power Semiconductor Devices (PWS Publishing, Boston, 1995), ISBN 0-534-94098-6

Chapter 3: Physical principles of measurements.

3.1 Capacitance Voltage Measurements

A *p/n* or a Schottky junction in reverse bias has a capacitance, which it will be referred to as "depletion" capacitance. This capacitance depends on various factors: the doping concentration, the temperature, the doping distribution, the built-in potential [Look]. The capacitance-voltage (C-V) characterization is the measurement of the capacitance as a function of the reverse bias, and is a paramount technique in semiconductor material and device characterization, as it gives the possibility of determining the doping density in the semiconductor and also its variations in depth. Moreover, the capacitance may be affected by the presence of electronic states (deep levels) in the gap, thus making it possible to characterize them by means of capacitance-based measurements.

3.1.1 CAPACITANCE VOLTAGE MEASUREMENTS ON SCHOTTKY DIODES

The space charge region of a Schottky diode can be considered a parallel plate capacitor. They, mainly, differ in the dependence of the stored charge on the applied bias. In a Schottky diode the charge depends on the applied bias, thus we can define a differential capacitance per unit area:

$$C(V) = \frac{\partial Q(V)}{\partial V} \tag{3.1}$$

The relationship between the stored charge and the applied bias can be found by solving the Poisson equation in the full depletion approximation:

(3.2) $$\frac{\partial^2 \phi}{\partial x^2} = -\frac{\rho}{\varepsilon_S}$$

For a Schottky barrier on a n-type material, the capacitance per unit area is [Look]:

(3.3) $$C = \left(\frac{q\varepsilon_S}{2(\phi - V)} N_D \right)^{\frac{1}{2}}$$

Since $1/C^2$ is linearly dependent on the a applied bias:

(3.4) $$\frac{1}{C^2} = A + Bx$$

the barrier height ϕ is related to the intercept with the y axis, A, through the relations:

(3.5) $$\phi = \frac{q\varepsilon_S A}{2} N_D$$

And

(3.6) $$\phi_B = \phi + \frac{k_B T}{q} \ln\left(\frac{N_C}{N_D} \right)$$

whereas the slope is related to the donor doping concentration [Sze]:

(3.7) $$N_D = \frac{2}{q\varepsilon_S B}$$

3.1.2 CAPACITANCE VOLTAGE MEASUREMENTS ON JUNCTION DIODE

The depleted region of a *p/n* junction can be considered as a parallel plate capacitor. The difference between a *p/n* junction and a Schottky barrier lies in the fact that in a Schottky barrier the depletion region is located only in the semiconductor. Since the quantity of stored charge depends on the depletion layer width, a differential capacitance can be defined:

$$C(V) = \frac{\partial Q(V)}{\partial V} \tag{3.8}$$

The relationship between the charge Q and the applied bias can be found by solving the Poisson equation (3.2) for the junction. In the depletion approximation, the transition region between the space charge region and the neutral region can be neglected. From (3.2) two equations are obtained, one for the n-type region and one for the *p* type region:

$$\frac{\partial^2 \phi}{\partial x^2} = qN_d \tag{3.9a}$$

$$\frac{\partial^2 \phi}{\partial x^2} = qN_A \tag{3.9b}$$

By solving these equations the extension of the depletion region is found as a function of the applied bias, both in the *n* type region and in the *p* type region (eqs. 3.11a and 3.11b).

(3.10a) $$x_n = \left(\frac{2\varepsilon_S}{q} \frac{N_A}{N_D} \frac{1}{N_A + N_D} (\phi_i - V) \right)^{\frac{1}{2}}$$

(3.10b) $$x_p = \left(\frac{2\varepsilon_S}{q} \frac{N_D}{N_A} \frac{1}{N_A + N_D} (\phi_i - V) \right)^{\frac{1}{2}}$$

Then

(3.11a) $$Q_n = qN_D x_n$$

and

(3.11b) $$Q_p = qN_A x_p$$

the capacitance of the space charge region is given by

(3.12) $$C = \left(\frac{q\varepsilon_S}{2(\phi - V)} \frac{N_A N_D}{N_A + N_D} \right)^{\frac{1}{2}}$$

By comparing equations (3.12) and (3.10) the dependence of the capacitance per unit area of a *p/n* junction is the same as for a parallel plate capacitor, but in a *p/n* junction the charge, and, consequently, the capacitance, depend on the applied bias.

In equation (3.12) the quantity $1/C^2$ shows a linear dependence on the applied bias V:

(3.13) $$\frac{1}{C^2} = A + Bx$$

Where the intercept with the *y* axis gives the built-in potential:

$$\phi = \frac{q\varepsilon_S A}{2}\frac{N_A N_D}{N_A + N_D} \tag{3.14}$$

The slope is related to the doping concentration:

$$B = -\frac{2}{q\varepsilon_S}\frac{N_A N_D}{N_A + N_D} \tag{3.15}$$

In a *p+/n* junction, $N_A >> N_D$; the value of the doping density in the lightly doped region, in this case the *n* type region, can thus be obtained:

$$N_D = -\frac{2}{q\varepsilon_S B} \tag{3.16}$$

By solving the Poisson equation for different values of the applied bias the doping profile in the lightly doped region can be obtained [Sze].

3.1.3 CAPACITANCE-VOLTAGE MEASUREMENTS SET-UP

The block diagram of the instrumentation used for the C-V characterization is sketched in Fig. 4.2. The building blocks of the setup are the Keithley 230 bias generator and the Keithley 3330 LCZ meter. The LCZ meter has operating frequencies ranging from 120 Hz to 10^5 Hz. The measurement is driven by software, with the following parameters:

- The bias interval V_{max}, V_{min}
- The bias step ΔV
- The time interval Δt between bias setting and capacitance reading

- The LCZ meter operating frequency f_{CAP}

The temperature is controlled with a Lakeshore 330 temperature controller.

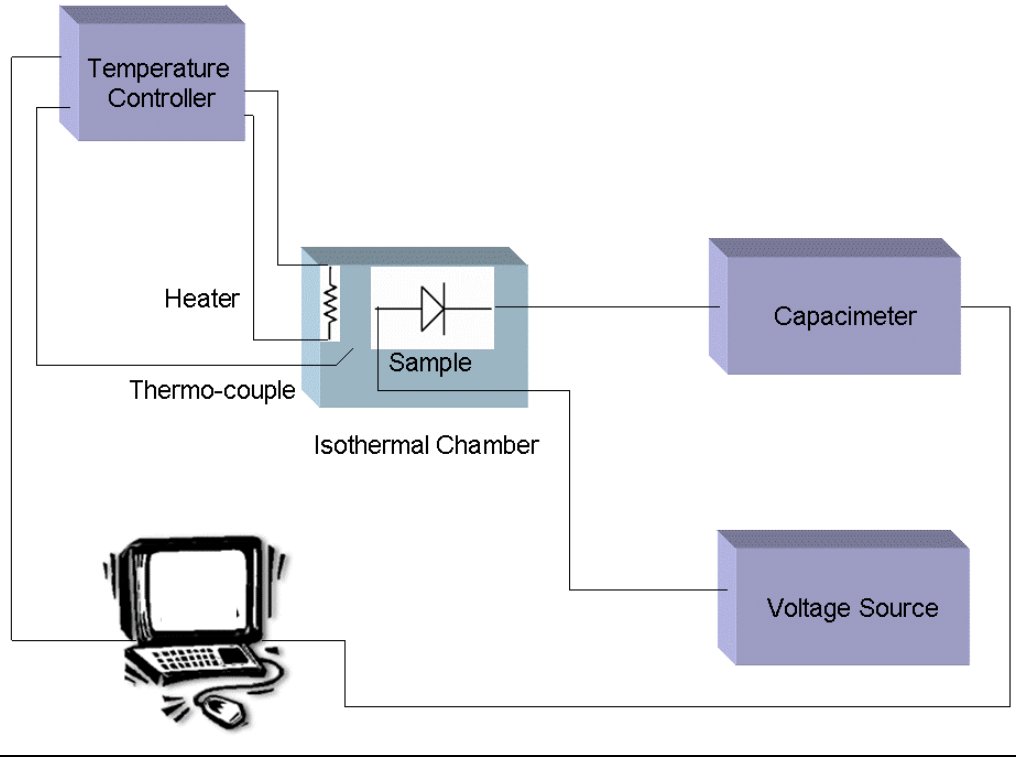

Figure 3.1 Block diagram for C-V characterization

3.2 Electrical and Electro-optical properties of defect by complementary transient spectroscopy

Impurities and defects introduce energy levels in the band gap of a semiconductor. These are usually divided into two classes, shallow and deep states. Shallow levels are hydrogenic impurities at which the electron is weakly bound by a Coulomb potential in an extended state, with the effective mass of the appropriate band edge. In the case of deep levels the impurity potential is strongly localized, and the electrons are tightly bound. The terms shallow and deep are referred to the energy level of the defect in the band gap, since the energy level of deep centres is deeper in the band gap than the energy level of shallow impurities [Blood,Orton]. The study of deep centres needs techniques sensitive to low defects concentrations, able to distinguish between majority- and minority-carrier traps, to provide information about the concentrations, energy levels and capture rates of the traps [Lang]. These techniques are mostly based on the study of transient phenomena related to carrier capture and emission at the centres. In a *p/n* junction or in a Schottky diode a pulsed bias induces a transient of the junction capacitance or conductivity. By monitoring the transient response as a function of temperature information on defect energy level, concentration, and capture rate are caught. The DLTS (Deep Level Transient Spectroscopy) technique is one of the most convenient and powerful methods for the detection and the characterization of deep levels in semiconductors.[Blood,Orton]. It is based on the analysis of capacitance transients repetitively generated by electrical excitation of the traps located in the space charge region of a junction. The transients are thermally stimulated and analyzed utilizing the rate window concept [Lang] In many applications, such as for example the study of semi-insulating or compensated materials, DLTS cannot be applied and other techniques are more appropriate to investigate deep traps. A significant

improvement was obtained by applying rate window concept to conductivity transients generated by optical excitation pulses or by electrical excitation pulse during a continuous optical generation of pairs. Various techniques have been developed based on this approach and among these PICTS (Photo-Induced Current Transient Spectroscopy)[Blood,Orton][Tapiero]and P-DLTS (Photo DLTS)[Mooney] are particularly interesting. They allow the determination of deep trap parameters (activation energy, capture cross section and concentration) in semi-insulating materials with good resolution, even though the data interpretation is more complex than in DLTS. Optical characterization techniques, such as cathodoluminescence (CL) can also be reliably used to investigate recombination process at deep levels in semi-insulating materials and are a suitable complement to the electrical transient spectroscopy methods. CL method will be explained in the next paragraph about scanning electron characterization techniques.

3.2.1 PHYSICS OF CARRIER CAPTURE AND EMISSION AT A TRAP

The dynamic occupancy at a deep centre is determined by capture of majority and minority carriers, and emission of majority and minority carriers. Capture processes are characterized by the capture cross section $\sigma_{n,p}$, related to the carrier concentration n and to the carrier thermal velocity $<v_{n,p}>$. If the total trap concentration is N_T and if n_T are the traps occupied by electrons at any instant, the number of electrons captured by the unoccupied traps in the time interval Δt is:

$$\Delta n_T = \sigma_n < v_n > n\left(N_T - n_T\right)\Delta t \tag{3.17}$$

and the electron capture rate is

(3.18) $$c_n = \sigma_n < v_n > n$$

and the electron capture rate is

(3.19) $$c_p = \sigma_p < v_p > p$$

Carrier emission is characterized by the emission rate $e_{n,p}$. Thermal emission rates are proportional to the Boltzmann factor, $\exp(-\Delta E/kT)$, where ΔE is the difference in energy between the trap and the conduction/valence band.

(3.20a) $$e_n = \frac{\sigma_n < v_n > N_C}{g} \exp\left(-\frac{\Delta E}{k_B T}\right)$$

(3.20b) $$e_p = \frac{\sigma_p < v_p > N_A}{g} \exp\left(-\frac{\Delta E}{k_B T}\right)$$

The occupancy of the state is determined by the competing emission and capture processes. The net change of electron occupancy at a trap is given by

(3.21) $$\frac{dn_T}{dt} = \left(c_n + e_p\right)\left(N_T - n_T\right) - \left(e_n + c_p\right)n_T$$

Where n_T is the number of occupied states and N_T is the total concentration of traps.

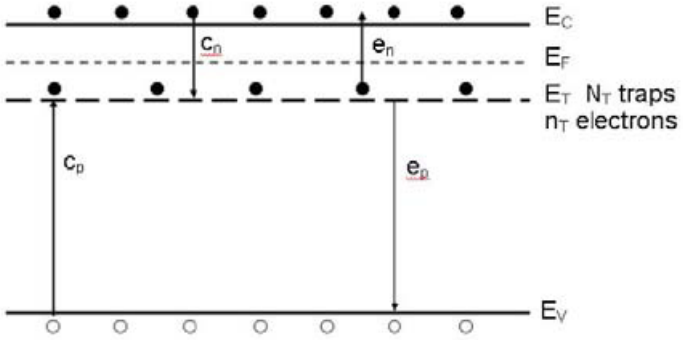

Figure 3.1 Capture and emission processes at a trap

Fig. 3.1 illustrates the capture and emission processes that take place at a deep level with energy E_T, and density N_T, occupied by n_T electrons. Let us consider a *p+/n* diode, that is the case analysed in this thesis. The junction behaviour is completely general, thus a Schottky diode will behave in the same way. Since the depletion region is primarily in the lightly doped side of the junction, the discussion is focused only on the traps in the lightly doped *n* type material of a *p+/n* diode. When the diode is reverse biased, the capture rates are zero because no mobile carriers are available for capture. The steady state occupation of the level is given by

$$n_T = \left(\frac{e_n}{e_n + e_p} \right) N_T \tag{3.22}$$

Traps can be divided into electron traps or hole traps. Electron traps tend to be empty and thus capable of capturing electrons, whereas hole traps tend to be occupied by an electron in order to have a hole recombine with the trapped electron (capture a hole). Consequently for electron traps $e_n >> e_p$ and for hole traps $e_p >> e_n$. The equilibrium state can be reached from two initial conditions, i.e. all the traps are initially occupied or all the traps are initially empty. For the first case:

(3.23a) $n(t) = N_T$ $t < 0$

(3.23b) $n(t) = N_T\left(1 - \exp(-c_n t)\right)$ $t > 0$

For the second case

(3.24a) $n(t) = 0$ $t < 0$

(3.24b) $n(t) = N_T \exp(-e_n t)$ $t > 0$

When a bias pulse is applied to the junction carriers are introduced, and the steady state occupancy is perturbed. The bias pulse also produces a capacitance change in the junction. Two main types of bias pulses can be distinguished: majority-carrier pulses, which momentarily reduce the capacitance and introduce only majority carriers; minority-carriers pulses, which drive momentarily the junction into forward bias, and minority and determine majority carrier injection. When the bias pulse is removed the capacitance returns to its quiescent value (Figure 3.2). The sign of capacitance change depends on whether the occupation of the traps had been increased or decreased by the pulse. For majority carrier injection the capacitance is reduced after the bias pulse, because compensating carriers are trapped in the space charge region, thus, the transient induced by majority carrier traps is negative. An increase in occupation by minority carriers causes an increase in capacitance, thus a transient induces by minority-carrier traps unloading is positive. Figure 3.2 is a schematic diagram of the trap occupation in a *p+/n* diode in the quiescent state (a), during the pulse (b), and after the bias pulse (c), for majority carrier traps. The transient response provides information on trap-filling procedures. The concentration of the traps is obtained from the transient amplitude. The concentration of hole traps in a *p+/n* diode is given by the relationship

(3.25) $$N_T = 2\frac{\Delta C}{C}\left(N_D - N_A\right)$$

Where ΔC is the capacitance change at the instant zero C is the capacitance in the quiescent state, and N_D-N_A is the apparent donor concentration on the *n* side of the junction where the trap is observed.

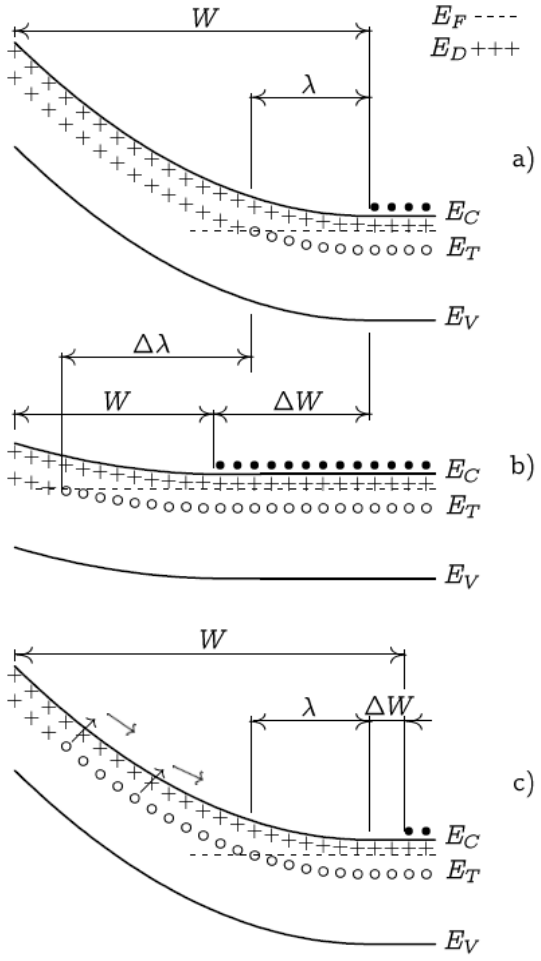

Figure 3.2 Electron in a p+/n junction in the quiescent state (a), a majority carrier injection pulse (b), and during the transient (c).

3.2.2 MAJORITY CARRIER TRAPS SPECTROSCOPY: DLTS

The DLTS technique is based on measurements of capacitance transients as a function of temperature. An apparatus capable of measuring the capacitance signal at two instants during the transient is employed. The diode is reverse biased at a voltage V_r and is then filled for a time t_f. A majority carrier transient is produced by filling the traps maximum to zero bias, whereas a minority carrier transient can be produced by filling the traps with a slightly positive bias , in case of a p-n junction, or with a light pulse in case of a Schottky diode. The bias is periodic with a period t_r, as shown in Fig. 3.3a. During the pulse, majority carriers are injected into the depletion layer and traps are filled. When the bias is set to V_r again, carriers are emitted at a rate e_p producing an exponential transient (Figure 3.3b).

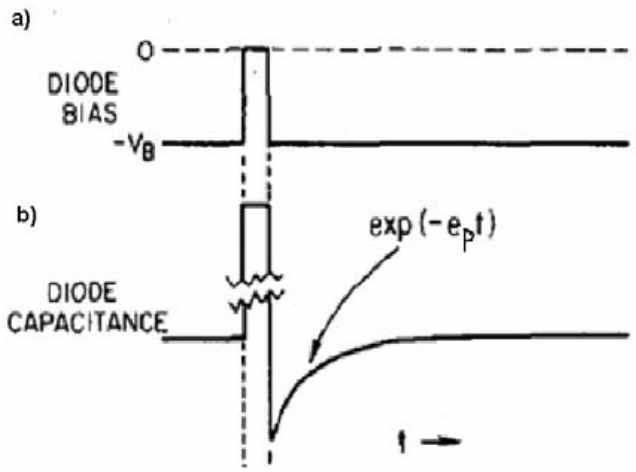

Figure 3.3 Periodic bias pulse applied to the junction (a), and consequent exponential transient (b).

The capacitance transient in its general form can be written as

$$C(t) = C(\infty) + \Delta C_0 \exp(-t/\tau) \tag{3.26}$$

Thus the signal is given by

$$S = \Delta C_0 \left[\exp\left(-t_1/\tau\right) - \exp\left(-t_2/\tau\right)\right] \tag{3.27}$$

where t_1 and t_2 are the instants at which the capacitance is measured, and τ is the time constant equal to e_n^{-1}. The maximum signal is obtained when the time constant τ is equal to a preset time constant τ_{ref}.

$$\tau(T) = \tau_{ref} = \frac{\left(t_2 - t_1\right)}{\left[\ln\left(t_2/t_1\right)\right]} \tag{3.28}$$

The dependence of e_n on the junction temperature (see 3.20a), is illustrated in Fig. 3.4.

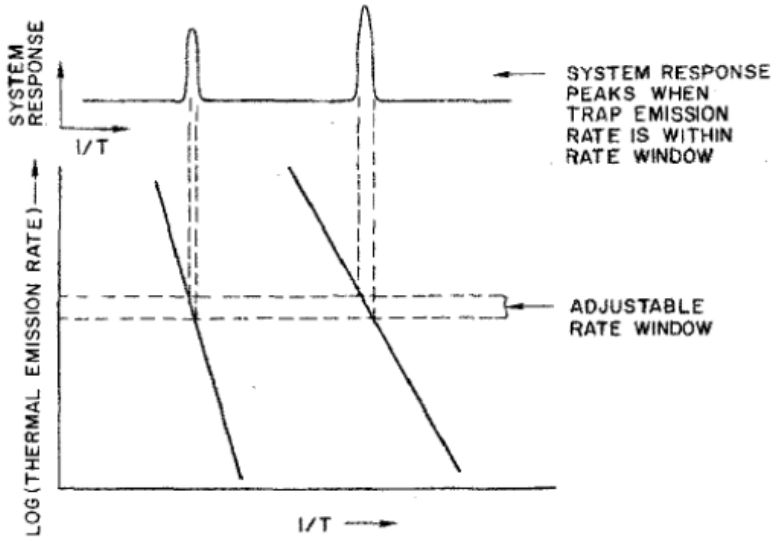

Figure 3.4 Relationship between the temperature dependent emission rate of a trap and peak temperature.

Consider two traps, featured by E_1 and σ_1 and E_2 and σ_2 respectively. As temperature increases the emission rate e_n increases and a peak occurs when

$\tau=e_n^{-1}$ passes through τ_{ref} for each trap. The DLTS output as a function of temperature is illustrated in Figure 3.5. For a given τ_{ref} the peak temperatures T_{pk1} and T_{pk2} are characteristic of each trap. By varying the t_1 and t_2 the peak position of each trap shifts (Fig. 3.4) and e_n can be obtained as a function of temperature. This is the rate window concept. The height of the peak maximum is related to the trap concentration (Eq. 3.25).

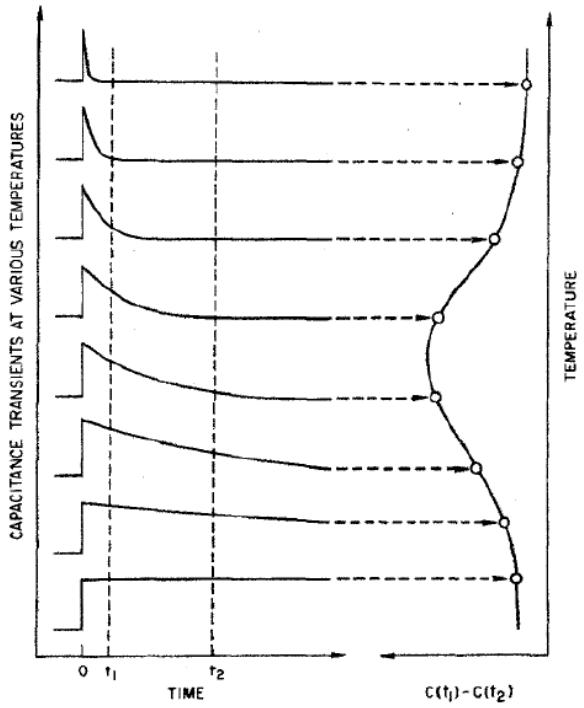

Figura 3.5 Dependence of the transient on temperature, and DLTS signal related to the rate window.

By repeating the scan with different rate windows, i.e. by changing the instants t_1 and t_2 in Fig. 3.5, sets of values of I and T_{pk} are obtained. From these values the trap energy and apparent capture cross section can be extracted by considering the linear dependence of the quantity $ln(T_2/e_n)$ on the reciprocal temperature (see eq. 3.20a).

(3.20a) $$e_n = \frac{\sigma_n < v_n > N_C}{g} \exp\left(-\frac{\Delta E}{k_B T}\right)$$

The product $<v_n>N_C$ is proportional to T_2, thus $ln(T_2/ e_n)$ is linearly dependent on the reciprocal temperature:

(3.29) $$\ln\left(\frac{e_n}{T^2}\right) = \ln(\sigma_n \gamma) - \left(\frac{\Delta E}{k_B} x\right) \qquad \text{where} \quad x = \frac{1000}{T}$$

The plot of the $\ln(T_2/ e_n)$ in function of the reciprocal temperature is defined Arrhenius plot; from this plot it's possible to calculate the energy of the deep level that is related to the slope of the line, whereas the capture cross section is related with the intercept with the reciprocal temperature axis.

3.2.3 PHOTO-CONDUCTIVITY TRANSIENT SPECTROSCOPY

Among the methods based on the analysis of photoconductivity, PICTS seems to be one of the most interesting and promising [Blood,Orton][Tapiero]. Traps are periodically filled by photocarriers generated by above band-gap light pulses; thermally stimulated detrapping induces a temperature dependent current transient to which the rate window concept can be applied. The approach, which follows directly the DLTS technique, allows PICTS to achieve higher sensitivity than other current methods. PICTS can be applied to samples with two ohmic contacts on the surface (planar configuration) or with a Schottky barrier and a back side ohmic contact (Schottky configuration). Both configurations produce similar spectra, but the Schottky barrier should give better resolved peaks [Fang]. In the planar configuration the emission of the carriers from the traps modulates the conductivity of the sample, whereas in the other case, the current is produced by carrier emission

in the depletion region. The general form for the transient current equation can be applied to both configurations:

(3.30) $$\Delta J(t) = -qBn_t(0)e_n \exp(-te_n)$$

Where $n_{ot}(0)$ is the trapped charged after the filling pulse and:

(3.31a) $$B = x_1\left(1 - \frac{x_1}{2W}\right)$$ for the Schottky case

(3.31b) $$B = E\tau_n\mu_n$$ for the planar case

Where x_1 is the depth at which the trap level equals the Fermi level at the steady state reverse bias, E is the electric field τ_n is the electron recombination lifetime and μ_n is the electron mobility. Because of the term e_n in front of the equation 3.31, the determination of the trap parameter becomes more complex.

Equation 3.31 applies both to emission from majority and from minority carrier trap since the current transients are of the same sense for both kinds of traps. Thus, the PICTS method reveals both majority and minority traps even though there is no define and reliable way to distinguish between them. As in high resistivity materials containing a high amount of compensating impurities the photoconductivity is general unipolar, the detected traps are most probably majority carrier traps, at least at low temperature [Balland]. To process current transients, it is usually assumed that a high photoexcitation is applied, so that all traps are saturated, and that there is negligible retrapping and linear recombination. [Balland]. One inconvenient feature of the planar configuration is the presence in equation (3.32b) of the $\mu\tau$ pre-exponential term due to the recombination and retrapping processes related not only to the investigated trap but also to the other deep centres. These effects, which may

be temperature dependent, influence the conductivity transient that cannot be simply described and analyzed. A possibility for eliminating this difficulty is to normalize $\Delta J(t)$ by the photocurrent $\Delta J_L(t)$[Yoshie, Kamihara]. The normalized transient takes the form [Tapiero]:

$$\Delta J_N(t) = \frac{\Delta J(t)}{\Delta J_L(t)} = \frac{\mu\tau}{\mu_0\tau_0}\frac{d^*}{\beta(\lambda)I_A}(h\nu)N_t \exp(-te_n) \tag{3.32}$$

Where d^* is the excited layer thickness, $\beta(\lambda)$ is the quantum efficiency, I_a is the intensity of light absorbed by the sample and $h\nu$ is the energy of the incident light.

The quantum efficiency $\beta(\lambda)$ is defined through the equation:

$$\beta(\lambda) = \frac{(1-R)\times\alpha\times d^*}{1-R\times(1-\alpha\times d^*)} \tag{3.33}$$

Where R is the reflectivity of the material in analysis and α is the absorption coefficient of material, which can be evaluated for the case of indirect band-gap material by [Galeckas]:

$$\alpha(T) = A\left[\frac{(h\nu\text{-}E_g(T)\text{-}k_B\theta)^2}{1\text{-}\exp(\text{-}k_B\theta/k_BT)} + \frac{(h\nu\text{-}E_g(T)+k_B\theta)^2}{\exp(k_B\theta/k_BT)\text{-}1}\right] \tag{3.34}$$

Where $E_g(T)$ is the value of the band-gap at a defined temperature T due to semi-empirical Vrasni law, $k_B\theta$ is the energy of the phonon due to the indirect band-gap transition and A is a constant of the material.

In narrow band-gap materials the factor $\mu\tau/\mu_0\tau_0$ is about 1 so it is possible to a good approximation to cancel out the $\mu\tau$ factor; for wide band-gap materials this approximation is not true but it is possible to estimate the $\mu\tau$ factor by

sampling the transient at the rate window times t_1, t_0 and it is possible to calculate the $\mu\tau/\mu_0\tau_0$ as showed in:

$$\frac{\mu_0\tau_0}{\mu_1\tau_1} = \left(\frac{I_t}{I_0}\right)^{1-\gamma} \qquad \text{where } 0.5 < \gamma < 1 \tag{3.35}$$

Therefore, the PICTS method, which possesses a better resolution than DLTS [Yoshie, Kamihara2], can be applied to semi-insulating materials to characterize deep traps, but it fails to determine their nature (majority/minority).

In table 3.1 is resumed the PICTS and DLTS methods compared also with P-DLTS

Table 3.1 Spectroscopic methods of operation

Transient Spectroscopy	Electrical excitation	Optical excitation	Output signal	Carrier traps
DLTS	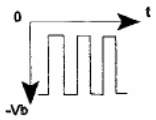	none	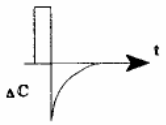	majority
PICTS	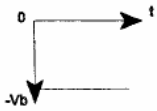	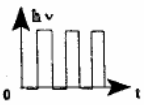	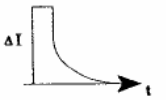	majority and minority
P-DLTS	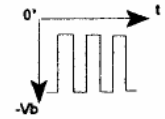	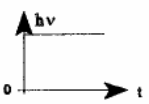	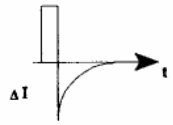	majority

3.2.4 THERMAL TRANSIENT SPECTROSCOPY SET-UP: DLTS, PICTS.

The thermal transient spectroscopy measurement is performed as follows: the sample temperature varies slowly, while the sample bias varies as described in Table 3.1 for the different techniques, with a fixed period P. Moreover, the capacitance or the current of the sample at reverse bias V_R and the capacitances during the transient at t_1 and t_2 must be measured. In order to achieve this, we make use of the following experimental equipment, which is sketched from Fig. 4.3a to 4.3c .

Temperature controller and cryogenic apparatus.

This instrument, a Lake Shore DRC91C, allows one to set and control the temperature of the sample. The user determines the temperature interval and heating rate through the software. For our setup, the heating rate must be lower than 0.083K/s. The temperature interval can vary from 77K, i.e. the liquid nitrogen temperature, to about 600K. The sample is left in a cryogenic apparatus, consisting of a cryostat containing liquid nitrogen, and a sample holder. A T-type thermocouple measures the temperature, while the sample holder can be heated by a resistor with a resistance of 35 Ω.

Impulse generator and equipment gauges.

The impulse generator and the gauges (capacitance meter for DLTS, amperometer for PICTS), together with the exponential correlators, are building blocks of the Sula Technologies Deep Level Spectrometer. The impulse parameters that are set on the impulse generator are:

- the period P

- the reverse bias V_{rev}
- the filling pulse bias V_{fill}
- the pulse duration (pulse width) t_p.

In the case of photoconductivity transient spectroscopy a UV-LED is used to optical excitation. The main wavelength of LED is around 370 nm, but it has also a secondary emission around 390 nm. The wavelength 370 nm corresponds to above band-gap of 4H-SiC energy, hence suitable for our purpose. To generate light pulse for the PICTS technique an external pulse-generator is used (HP 8003 Pulse Generator). The capacitance meter works at a frequency of 1 MHz, thus being able to reproduce accurately capacitance transients with time constants of the order of some tens of μs. The output of this instrument yield the reverse-bias capacitance C_0, and the capacitance transient, which is further processed by the correlators and boxcar averager of the instrument. To perform current measurement the 1 MHz signal is switched off and a current pre-amplifier is added to the set-up, due to the low reverse current of 4H-SiC samples. The amplification range is between 40 dB and 120 dB.

Exponential correlators and double boxcar averagers.

The deep level spectrometer incorporates four correlators, which play the role of reducing the noise affecting the capacitance or current transient. The output of each correlator is then processed by a double boxcar averager, which, in turn, yield as output the signal $\Delta C=C(t_1)-C(t_2)$, or $\Delta I=I(t_1)-I(t_2)$ depending on the technique. To each boxcar averager correspond four different values of the couple (t_1,t_2), so that in a single measurement it is possible to collect four spectra. The ratio t_1/t_2 is fixed and equal to 2.5 for capacitance measurements and to 1.95 for current measurements. The signal is the processed by the double boxcar averager. Here two input channels correspond to two linear

gates which sample the signal at instants t_1 and t_2, while a differential block yields at the output the difference of the signals measured by the two gates. The measurement setup for DLTS and PICTS are illustrated in fig. 4.3a, 4.3b and 4.3c, respectively.

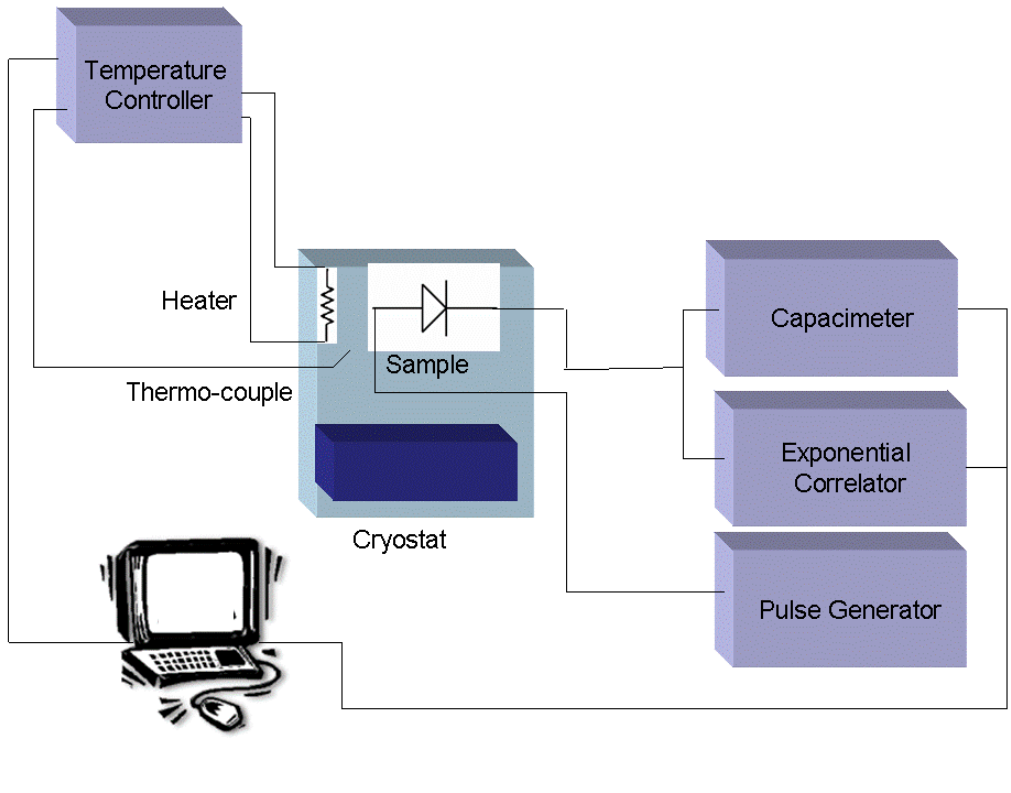

Figure 3.2a Block diagram for DLTS measurements

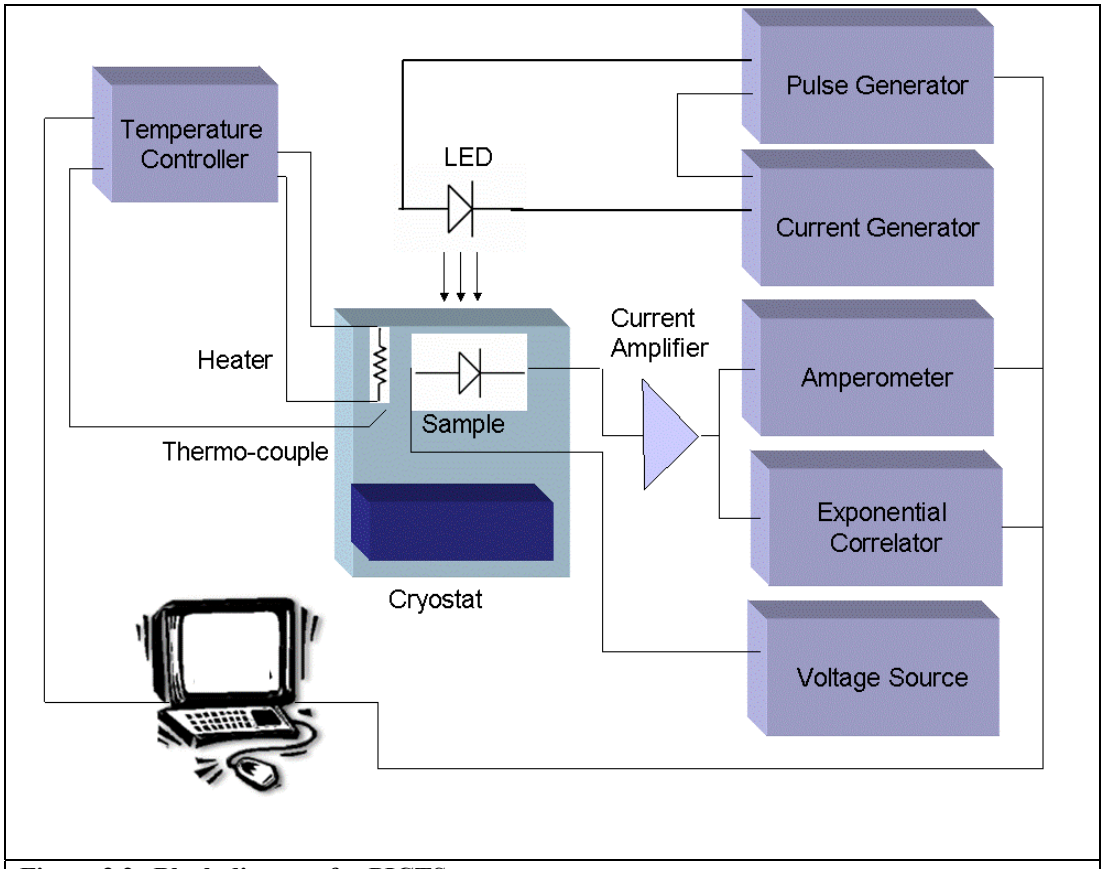

Figure 3.2c Block diagram for PICTS measurements

3.3 Scanning Electron Microscopy and Spectroscopy

Scanning electron microscopy is a useful tool for an analysis of surfaces. The variety of interactions between electrons and solids allows a versatile way of characterization. In a SEM electrons are used for analysis. An electron gun provides electrons by thermoionic or field emission. The electron beam, which typically has an energy ranging from a few hundred eV to 50 keV, travels towards the sample passing through a series of magnetic lenses designed to focus the beam to a very fine spot. The focused beam passes through pairs of scanning coils in the objective lens, which deflect the beam in a raster fashion in order to scan a rectangular area of the sample surface. The electron beam is focused by one or two condenser lenses into a beam with a very fine focal spot. When the beam hits the sample surface the electron beam is deflected in various directions and spreads in a volume, known as the interaction volume. Interactions in this region lead to the emission of secondary electrons which are detected to produce an image. Several types of interactions take place, thus leading to several types of images produced by backscattered electrons, secondary electrons, transmitted electrons, or Auger electrons. Other phenomena caused by the incident beam are formation of electron-hole pairs, leading to electron beam induced conductivity, and cathodoluminescence. The signal is then revealed by a detector and an image is formed and presented on the screen of a Cathode Ray Tube. The correspondence between the spots excited by the beam and pixels on the CRT is the essential feature of a SEM [Armigliato].

3.3.1 BEAM-SAMPLE INTERACTION

An accelerated electron incident on a solid undergoes two main kinds of interaction: Elastic diffusion, which deflects the electrons without changing their energy. Anelastic diffusion, in which electron lose energy, but do not change their direction. The latter is the process that produces all types of signal except for backscattered electrons. The electrons of the external orbitals, the most weakly bound, are expelled from the solid. Since these electrons have low energies, only the ones generated near the surface have energy enough to overcome the surface barrier of the material and get out of the solid.

Due to the wide nature of events that take place in the beam solid interaction, the physical model of the interaction is rather complex. An analytical expression of the decrease in energy per unit length is [Kotera].

(3.38) $$\frac{dE}{dS} = -2e^4 \pi N_a \frac{\rho Z}{EA} \ln\left(\frac{1.166E}{J}\right)$$

where e is the electron charge, ρ is the material density, Z is the atomic number, A is the atomic weight, N_a is the Avogadro number, E is the mean energy of the beam (keV), at the length x measured along the effective path of the electron, and J is the mean ionization potential of the hit material. The term J represents the mean energy loss of the incident beam for each anelastic interaction, and increases with Z, that is defined in keV by the Bethe expression [Rao-Sahib,Wittry]:

(3.39) $$J = \left(9.76Z + 58.5Z^{-0.19}\right)10^{-3}$$

The elastic scattering can be divided into two contributions: Rutherford diffusion, by the coulomb potential of the nucleus, and multiple diffusion,

which consists in a series of small angle deviations along the path, due to the coulomb interaction with the nuclei screened by the electrons. The maximum distance of an electron before a high angle deviation varies with Z. Thus, electrons penetrating into a solid with a low atomic number have high angle diffusion probability lower than electrons penetrating into a solid with high atomic number. As a consequence the interaction volume has a drop-shape for solids with low atomic numbers, and hemispherical for solids with high atomic numbers, as illustrated in Figure 3.6 [Kanaya,Okayama].

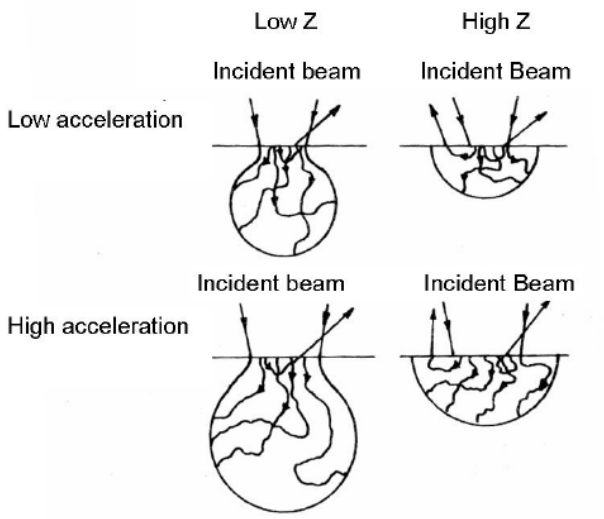

Fig. 3.6. Interaction volumes of the incident beam with a solid as a function of the beam energy in case of low and high atomic number

The full penetration range of electrons is expressed by the empirical relation in micron [Kanaya,Okayama]

$$R_e = \left(\frac{0.0276 A}{\rho Z^{0.889}} \right) E_b^{1.67} \tag{3.40}$$

Where ρ is expressed in g/cm^3 and E_b in keV.

3.3.2 IMAGES BY SECONDARY ELECTRONS

Images by secondary electrons are the most frequently used to analyse sample surfaces. Since secondary electrons have low energy (<50 eV) it is possible to detect only electrons that originate within a few nanometers from the surface. The electrons are detected by a photomultiplier, and the resulting signal is rendered into a two-dimensional intensity distribution. The brightness of the signal depends on the number of secondary electrons reaching the detector. If the beam enters the sample perpendicular to the surface, then the activated region is uniform about the axis of the beam and a certain number of electrons "escape" from within the sample. As the angle of incidence increases, the "escape" distance of one side of the beam will decrease, and more secondary electrons will be emitted. Thus steep surfaces and edges tend to be brighter than flat surfaces, which results in images with a well-defined, three-dimensional appearance. On the contrary cavities tend to be darker because of the shadow effect of the surrounding area. The number of secondary electrons depends on the beam energy and on the atomic number of the target. Thus, different sample compositions can be revealed by SEM.

3.3.3 ELECTRON BEAM INDUCED CURRENT

The nature of the SEM's probe, energetic electrons, makes it uniquely suited to examine electronic properties of semiconductor materials. The high-energy electrons from the SEM beam will inject charge carriers into the semiconductor. Thus, beam electrons lose energy by promoting electrons from the valence band into the conduction band, leaving behind holes. If the sample contains an internal electric field, such as in a p-n junction, the SEM beam injection of carriers will cause electron beam induced current (EBIC) to flow. The current is revealed through a circuit illustrated in Fig. 3.7.

When a beam hits a solid the currents that are formed are: the beam current I_p, the secondary electron current I_s, the backscattered electron current I_b, and a current of absorbed electrons I_a. I_a is produced by the fact that I_p-I_b-$I_s \neq 0$, thus the tendency of the sample to get charged is balanced by the current I_a, flowing from the sample to the mass of the circuit. This relationship shows that I_a is complementary to the current of emitted electrons I_b+I_s.

(3.41) $$I_a = I_p - (I_b + I_s)$$

This does not necessarily mean that the contrast in EBIC images is the opposite as in SEM images. In fact, the EBIC contrast is also related to variations in the collection efficiency, due to recombination centres or variations in the internal electric field that separates the charges. A comparison between secondary and EBIC images allows a study of defects.

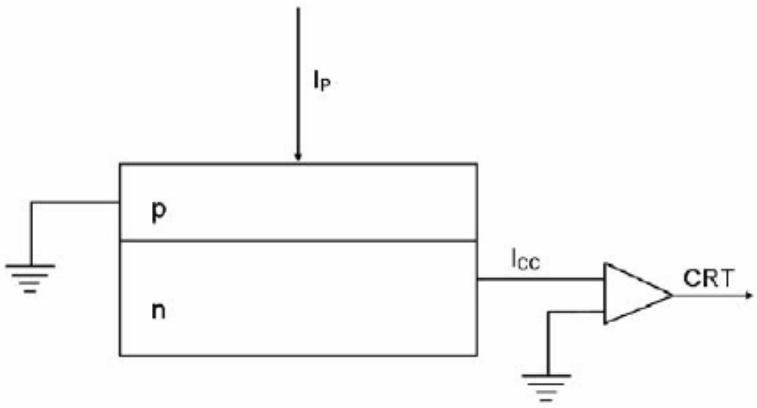

Figure 3.7. Equivalent circuit for an EBIC measurement on a p-n junction.

3.3.4 CATHODOLUMINESCENCE

Cathodoluminescence is the emission of light as the result of electron (cathode-ray) bombardment. CL is the unique contactless method that provides microcharacterization of the optical and electronic properties of semiconductor materials among the SEM techniques. In general CL analysis performed in a scanning electron microscope can be divided into microscopy and spectroscopy. In the former, luminescence images or maps of regions of interest can be displayed; in the latter, a spectrum corresponding to a selected area of the sample can be obtained [Yacobi,Holt].

The CL signal is formed by detecting photons of the ultraviolet , visible, and near-infrared regions of the spectrum. These photons are emitted as the result of electronic transitions between the conduction and valence bands and levels lying in the band gap of the material. Many useful signals in these cases are due to transitions that involve impurities and a variety of defects. Therefore, there is no general rule that would serve to identify bands or lines in the CL spectrum. In inorganic solids light is emitted as the result of electronic transitions between quantum mechanical states differing in energy. Luminescence emission spectra can be divided in intrinsic and extrinsic. Intrinsic luminescence, which appears at ambient temperature as a near Gaussian-shaped band of energies with its intensity peak at a photon energy $h\nu \approx E_g$, is due to recombination of electrons and holes across the fundamental energy gap, so it is an intrinsic property of the material. This edge emission band arises from essentially conduction-band to valence-band transitions. In materials with direct gap, the most likely transitions are across the minimum-energy gap, between the most probably filled states most likely to be unoccupied at the maximum of the valence band. If the band extrema do not occur at the same wave vector *k* transitions are indirect. For the conservation of the moment in the indirect band-gap material phonon participation is required. Thus, the recombination of electron-hole pairs must be accompanied by the simultaneous emission of a photon and a phonon. Since this requires

two particle interaction, the probability of such a process is significally lower compared with direct transitions. Therefore, fundamental emission in indirect-gap semiconductors is relatively weak, especially when compared with that due to impurities or defects (Figure3.8).

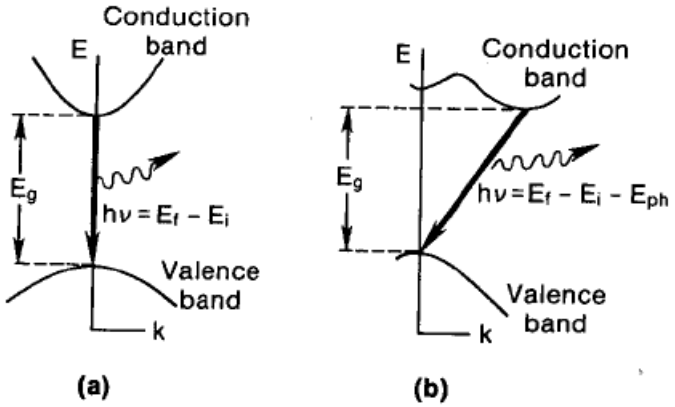

Figure 3.8 The energy transition in (a) direct and (b) indirect-gap semiconductors between initial states E_i and final state E_f. For indirect transitions the participation of a phonon (E_{ph}) is required

The emission spectra, which depend on the presence of impurities, are defined extrinsic. A simplified set of radiative transitions that lead to emission in semiconductors containing impurities is given in Figure 3.9. General properties of these transitions will now be discussed briefly. Process 1 is an intraband transition: an electron excited well above the conduction-band edge and reaches thermal equilibrium with the lattice. Process 2 is an intraband transition; this produces intrinsic luminescence. Process 3 is the exciton decay observable at low temperature; both free excitons and exicitons bound to an impurity may undergo such transitions. For bound excitons, one of the charge carriers is localized at a center that can assist in conservating momentum during the transition. This will be especially important in indirect-gap materials. Processes 4,5 and 6 arise from transitions that start and/or finish on localized states of impurities (e.g. donors and acceptors) in the gap; these produce extrinsic luminescence. The recombination processes between free

carriers and trapped carriers of the opposite type are known as the Lambe-Klick model representing donor-to-free-hole transition (process 4) and the Schon-Klasens model representing free-electron-to-acceptor transition (process 5), and the donor-acceptor pair (DAP) recombination model (process 6). Transition 7 represents the excitation and radiative deexcitation of an impurity with incomplete inner shells.

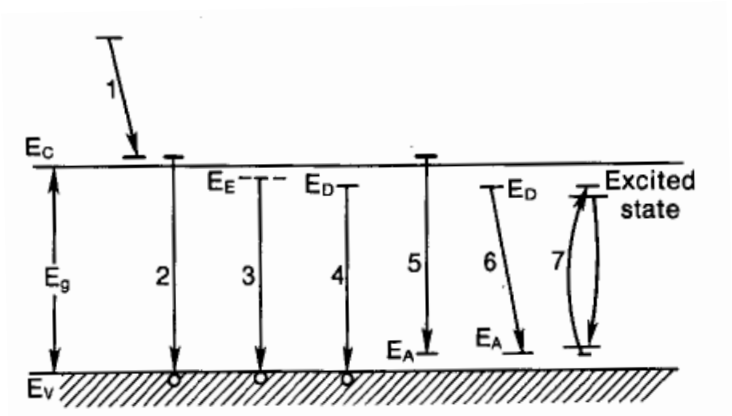

Figure 3.9 Schematic diagram of radiative transitions between the conduction band (E_C), the valence band (E_V) and exciton (E_E), donor (E_D) and acceptor (E_A) levels in a semiconductor.

It has to be reminded that CL can describe only radiative emission process. Nonradiative recombination events can be deduced only from CL-image, provided the contrast between radiative and nonradiative sites is sufficiently strong . However, quantitative information on defect-induced nonradiative process is unavaible in spectroscopic CL analysis. [Yacobi,Holt]

3.3.5 CATHODOLUMINESCENCE SET-UP

Cathodoluminescence observations were done with an electron beam tester composed of a scanning electron microscope (Hitachi 4210) and a light detection system. Observations are performed with different electron accelerating voltage (between 10 KeV and 30 KeV) in the way to perform a depth resolved CL analysis. A low temperature system is installed on the

microscope: the building block is a rotary pump that makes flow liquid helium inside the chamber in the way to cool down the system to 30 K; the temperature is monitored with a Lakeshore 321 cryogenic temperature controller. The beam current is varied in the way to achieve a higher electron-hole pair formation. The spot size in the electron microscope is 50 nm. Cathodoluminescence emission is collected by an ellipsoidal mirror and led to a monochromator (Jobin Yvon, HR-320) via an optical fibre. A serial detector and parallel detector are installed in the system. The serial detector is a photomultiplier (Hamamatsu, R3310-02) working in a photon-counting mode. The parallel detector is a charge-coupled device (Jobin Yvon, Spectra-View 2D). The parallel detection system is used for CL spectral acquisition and the serial one for CL imaging. The system is controlled by BIAMS software. It is possible to control by software different parameters as:

- The monochromator slit size
- The scanning time
- The resolution of the CL images

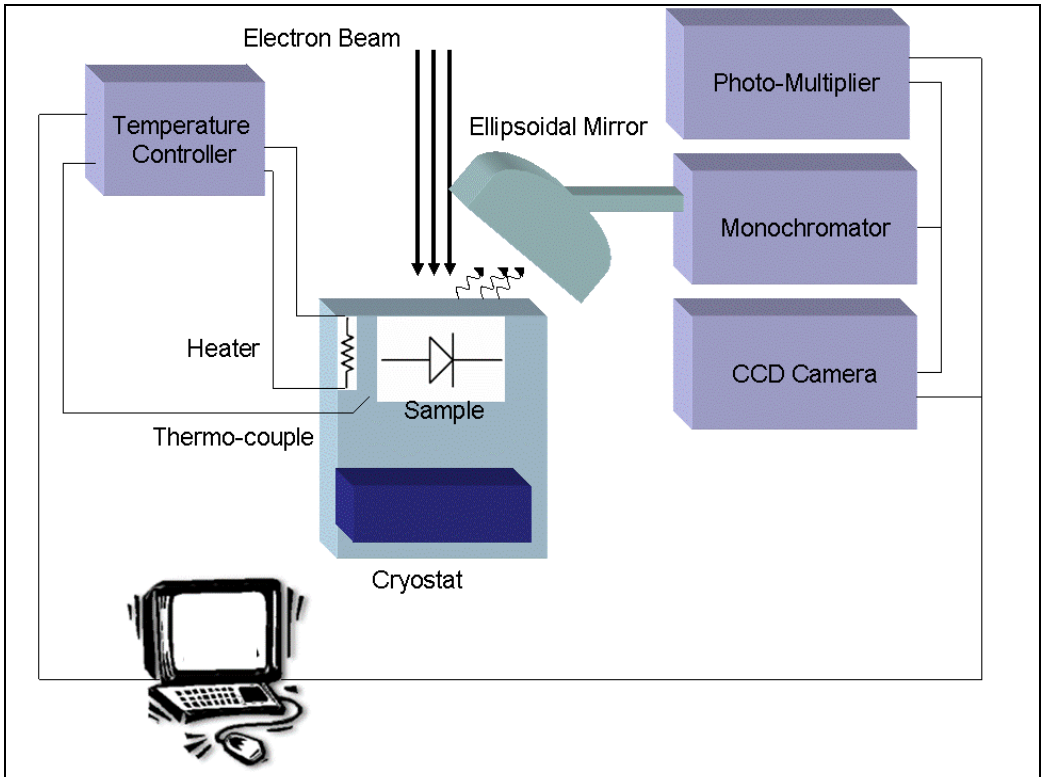

Figure 3.3 Block diagram for CL observations

Bibliography

[Look] Look D.C., Electrical characterization of GaAs materials and devices. Wyley Publ. New York (1989)

[Sze] Sze S M *Physics of semiconductor devices* Wiley, New York (1969)

[Blood,Orton] Blood P, Orton JW. T*he electrical characterization of semiconductors: majority carriers and electron states.* Academic Press, London (1992)

[Lang] Lang DV, J Appl Phys, 45 p. 3023 (1974)

[Tapiero] M. Tapiero, N. Benjelloun, J.P. Zielinger, S.E. Hamid and C. Noguet J. Appl Phys. 64 p. 4006 (1988)

[Mooney] P. M. Mooney J. Appl. Phys. 54, p. 208 (1983)

[Fang] Z. Fang, L. Shan, T.E. Schlesinger, A. G. Milnes Solis State Electronic 32 p.405 (1989)

[Balland] J.C. Balland, J.P. Zielinger, C. Noguet, M. Tapiero J. Phys D 19, p. 57 (1986)

[Yoshie, Kamihara] O. Yoshie, M. Kamihara, Jpn. J. Appl. Physics 22 p.621 (1983)

[Galeckas] A.Galeckas, Phis.Stat.Sol, (a), 191, n2, 613-620, (2002)

[Yoshie, Kamihara2] O. Yoshie, M. Kamihara, Jpn. J Appl. Physics 22 p.629 (1983)

[Armigliato] Armigliato A, Valdrè U, *Microscopia Elettronica a scansione e microanalisi*, Univ. Bologna

[Kotera] M. Kotera, K. Murata, K. Nagami, J. Appl. Phys. 52 p. 997 (1981)

[Rao-Sahib,Wittry] T.S Rao-Sahib, D.B Wittry, J. Appl. Phys. 45 p. 5060 (1974)

[Kanaya,Okayama] K. Kanaya, S. Okayama J. Phys. D 5, 43 (1972)

[Yacobi,Holt] B.G. Yacobi, D.B. Holt, Cathodoluminescence microscopy of inorganic solids

Chapter 4: Neutron irradiation induced defect in 4H-SiC particle detector

Silicon carbide (SiC) is one of the compound semiconductor which has been considered as a potential alternative to Si for the manufacture of dosimeters, spectrometers and charge-particle detectors in high energy physics experiments [Ruddy]. In fact, the option to upgrade the luminosity of the Large Hadron Collider (LHC) at CERN will involve radiation fluence of fast hadrons above 10^{16} cm^{-2} [RD50]. The radiation hardness of the current n-type silicon detectors is unable to cope with such an environment. Silicon carbide is one of the most promising wide band gap material due to its radiation hardness properties [IEEE]. For this reason over the last few years considerable effort has been concentrated on the better understanding the detection performance of silicon carbide detectors after heavy irradiation. The most recent results concern the use of semiconductors epitaxial 4H-SiC [Castaldini01], [Kalinina] as well as semi-insulating 4H-SiC materials [Rogalla] [Cunningham]. It is well known that the degradation of the detectors with irradiation, independently of the material used for their realization, is caused by lattice defects, like creation of point-like defect, dopant deactivation or damage regions (cluster or dead layers) and that a crucial aspect for the understanding of the defect kinetics at a microscopic level is the correct identification of the crystal defects in terms of their electrical activity. The understanding of the defect kinetics, in fact, would inform how to modify the material in order to reduce the degradation of the electrical properties of the detectors [RD48][Lindstrom]. For this purpose preliminary study have been performed on irradiation on Schottky 4H-SiC particle detectors with 6.5 MeV protons and 8 and 15 MeV electrons [Castaldini02][Alfieri] and 4H-SiC junction detectors [Menichelli][Moscatelli]. In this chapter the study has been extended to the case of 4H-SiC detectors, irradiated with neutron at different fluences. The chapter is divided in two main subsection, one for Schottky detectors and the

second one for junction detectors, respectively. In the *p*+/*n* detector case, a thorough study of the un-irradiated device has been carried out, in the way to achieve a better understanding of the implantation induced defect and of the transport properties of this device.

4.1 Schottky particle detector

4.1.1 ANALYZED SAMPLES AND IRRADIATION CONDITION

The samples examined were 4H-SiC epilayers grown by Chemical Vapour Deposition (CVD) and provided by CREE Research. The doping concentration of the epitaxial layer was N_D= 6.5 x 10^{14} cm^{-3} as measured by C-V characteristic. This value is in good agreement with the grower data. This layer, 39 μm thick, was grown on a 400 μm thick 4H-SiC substrate with doping density N_D= 10^{19} cm^{-3}. The declared micropipe density was 16-30 cm^{-2}. The epitaxial growth was performed using silane (2% diluited in H_2) and propane (5% in H_2) as process gases. Palladium purified hydrogen was used as carrier gas. The carbon to silicon ratio is 2. Schottky contact was nickel silicide, 200 nm thick, annealed at 600 °C in N_2 atmosphere with a diameter of 2.55 mm. Metal oxide field rings were synthesized in order to prevent the electric field crowding at the contact edges. The ohmic contacts were obtained by growing Ti/Pt/Au multilayer (with thickness of 30 nm /30 nm /50 nm respectively). The details of the contact processes are reported in [Nava01] and [Sciortino].

Figure 4.1 is the cross section of the analyzed Schottky diodes. The samples have been irradiated with increasing fluence (from 2 x 10^{13} cm^{-2} to 8 x 10^{15} cm^{-2}) of 1 MeV (NIEL equivalent in silicon) neutrons (Table 4.1). Details about the nuclear reactor used (TRIGA), the irradiation set up and procedure and the neutron spectrum can be found in [Nava02].

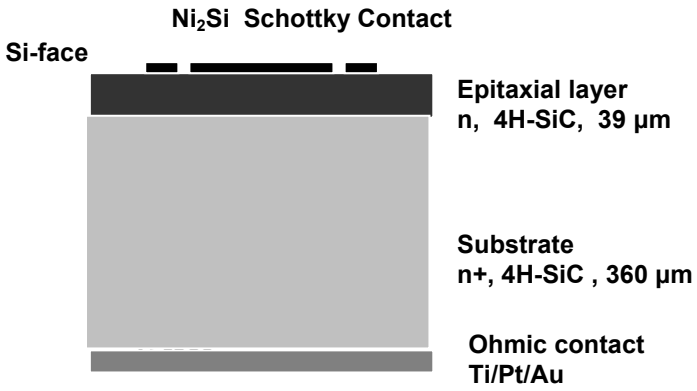

Figure 4.1 Schottky diode structure

Table 4.1 Irradiation Condition

Neutron 1 MeV	
Sample	Fluence (n/cm^2)
A#13	Not Irradiated
A#14	2 x 10^{13}
A#15	6 x 10^{13}
A#5	1 x 10^{14}
A#23	8 x 10^{14}
A#21	3 x 10^{15}
A#30	5 x 10^{15}
A#32	7 x 10^{15}
A#38	8 x 10^{15}

4.1.2 EFFECT OF IRRADIATION ON THE ANALYZED SAMPLES: EVOLUTION OF TRANSPORT PROPERTIES.

The defects, expectedly introduced by high-fluence irradiation, affect the electronic transport properties. The diodes current density as a function of forward and reverse voltage, before and after irradiation at different neutron fluences is shown in Figure 4.2a. The irradiation causes two main effects. For low fluence (up to 1 x 10^{14} n/cm^2) the forward current density decreases, showing the effect of the sum of parallel diodes currents with different barrier height and series resistance[Dascalu][Definev][Ewing]. In this case the reverse current density increases, it is due to the increase of defect concentration which participates in the reverse bias conduction. For high neutron fluence (higher than 1 x 10^{14} n/cm^2) there is a decrease of both the reverse and forward current; on irradiated samples with fluences higher than 8 x 10^{14} n/cm^2 the value of the current density is equal in forward and reverse current. The decrease of both reverse and forward current is due to the neutron irradiation induced introduction of defects in the material which act as charge carrier trapping centres. The thermal activation plot of the temperature-corrected diode reverse current J/T^2 vs. inverse temperature $1000/T$ for un-irradiated and irradiated diodes up to 8 x 10^{15} n/cm^2 is shown in Figure 4.2b. Two groups of curves, labelled A and B, have been identified which refer to diodes irradiated at fluences lower than 1 x 10^{14} n/cm^2 and higher up to 8 x 10^{15} n/cm^2, respectively. The thermal activation energy of the group A has been evaluated around 0. 64 eV; the activation energy for the group B is 1.1 eV. The increase of the thermal activation energy means that the deep level energy, which dominated the reverse current, is moved toward mid-gap energy.

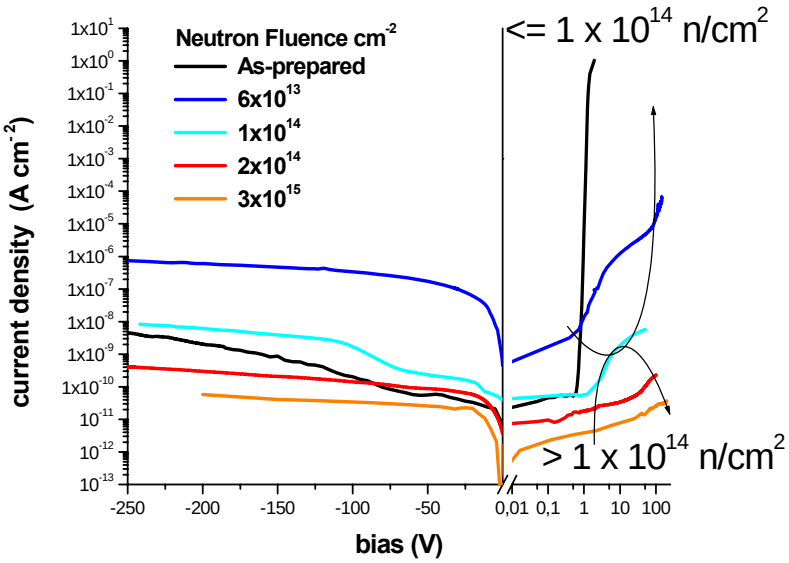

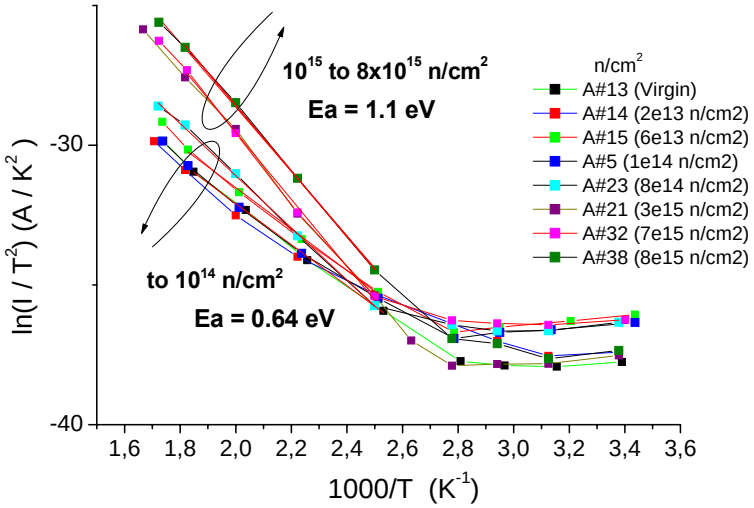

Figure 4.2a) J-V characteristics of the analyzed samples at different neutron fluences

b) Thermal activation energy plot, with grouping due to the different behaviour of the low fluence

and high fluence irradiated samples

Figure 4.3 shows the experimental charge collected efficiency (CCE), tested by irradiating the Schottky contact with 4.14 MeV α-particles, as a function of the reverse bias for un-irradiated detectors and irradiated ones at the indicated fluences. The high radiation hardness of 4H- SiC manifests itself as a small change in the charge collection efficiency of the detector up to 1 x 10^{14} n/cm^2; increasing the neutron fluence, the CCE decrease monotically to an asymptotic value, but the detector is still operative also after strong irradiation. The device is still operative because after 2 x 10^{14} n/cm^2 the irradiated detector can be reverse biased with higher voltage without breakdown. The aforesaid grouping, suggested for thermal activation energy measurements, can be proposed also for CCE measurements. Group A shows high collection efficiency at low reverse voltage, meanwhile group B shows a decrease of CCE also with the possibility of increasing the applied reverse voltage. Comparing the activation energy measurements, the change in the dominant deep level for reverse conduction cause the degradation in the CCE, the 1.1 eV deep level induces an effect of carrier compensation that is the reason of the decreasing of the carrier collection.

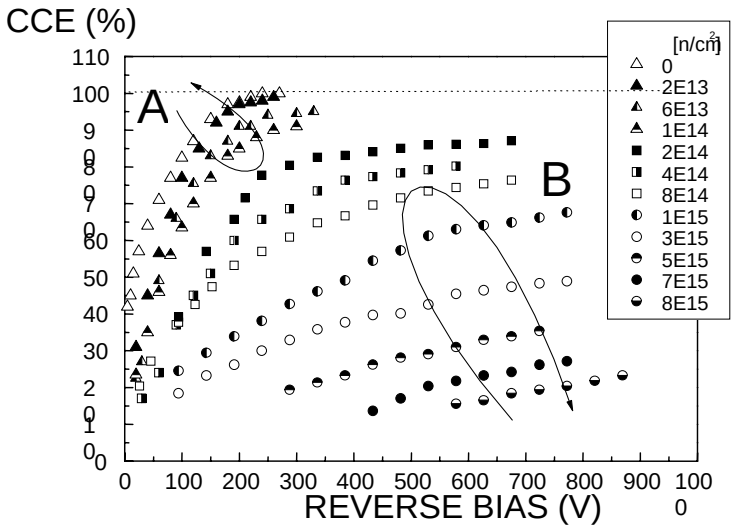

Figure 4.3 Charge Collection Efficiency of the irradiated samples as function of the reverse bias

A comparison of EBIC micrograph of un-irradiated device (Fig. 4.4a) and low fluence irradiated one (Fig. 4.4b) shows the effect of irradiation on the lattice. The inhomogeneity of the EBIC contrast in irradiated sample is a proof of the lattice disorder caused by the neutron irradiation. Figure 4.4a shows the presence of line defect inside the device. In hexagonal silicon carbide, grown off-axis, is possible to observe two different kind of edge dislocation. The edge dislocation has the Burger vector $\vec{b}$,which is normal to the dislocation direction. It is possible to divide in threading edge and basal edge dislocations. The threading edge dislocation are perpendicular to the surface, meanwhile the basal edge dislocation lays on the growth plane (8° degree off axis), the strain field induced by these defects can be a source of point defect induced by neutron irradiation. This hypothesis is proved by the dark halo that surrounds the line defect in the irradiated sample (underlined in Fig. 4.4b).

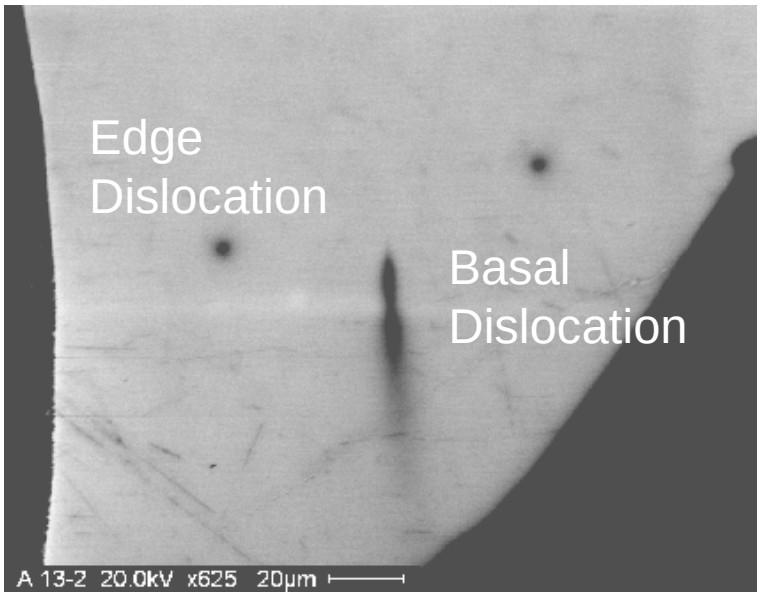

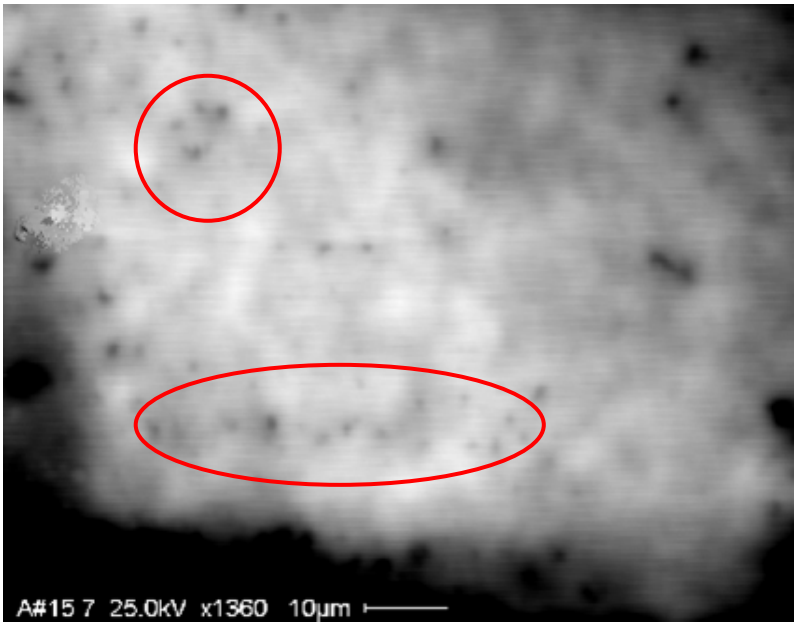

Figure 4.4a) EBIC micrograph of un-irradiated device, showing the different of line defects

b) EBIC micrograph of low fluence irradiated sample, the contrast is inhomogeneous

4.1.3 EFFECT OF IRRADIATION INVESTIGATED BY DLTS AND PICTS

A deeper electrical characterization of the irradiation-induced defects is however required to monitor in more details the compensation effect and moreover to explain the observed degradation of the CCE at the highest neutron fluences. For this purpose DLTS and PICTS measurements have been carried out on the as-prepared and neutron irradiated samples. Figure 4.5 shows the DLTS spectrum of the un-irradiated sample. Five peaks appear in the spectra; the SN1 deep level has an activation energy E_C-E_t = 0.06 eV, and then can be related to the nitrogen doping of the device [Chen]. The SN3 due to its energy (E_C-E_t = 0.68 eV) can be related to the well-known defect of silicon carbide Z_1/Z_2. The main findings of the un-irradiated sample analysis is that even if deep centers, as SN5 and SN6, with energy E_C-E_t = 0.82 eV and

E_C-E_t = 1.16 eV, respectively. These deep levels, more likely play the main role in the limitation of the CCE, are too low in concentration (≈10^{12} cm^{-3}) to influence it, in agreement with experimental data of Fig. 4.3. A complete resume of the deep levels parameters will be reported in Table 4.2 after the PICTS analysis.

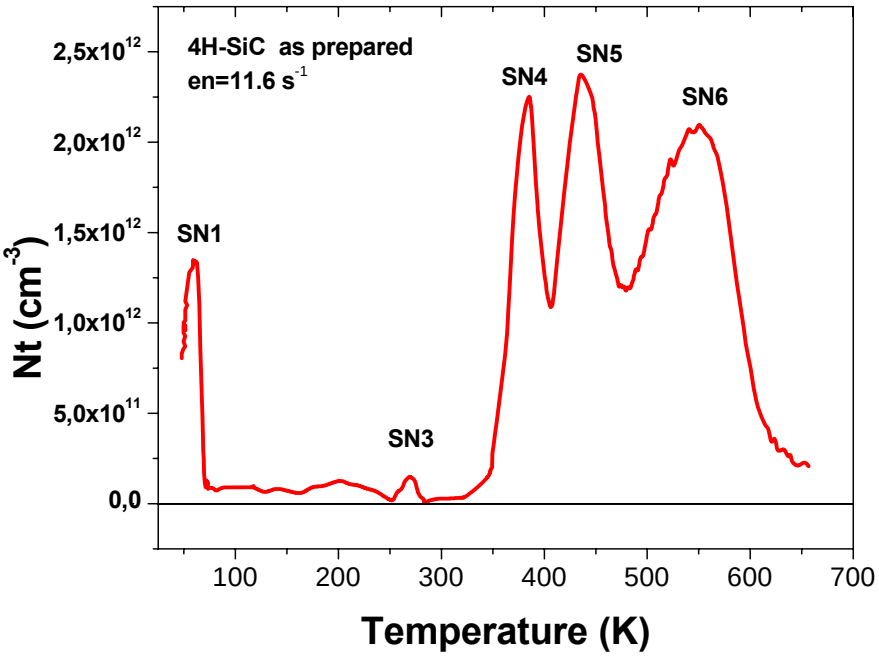

Figure 4.5 DLTS spectra of the un-irradiated sample.

Upon neutron irradiation at 2 x 10^{13} n/cm^2 and 6 x 10^{13} n/cm^2 (Fig 4.6), some main findings can be deduced: two new electron trapping centres appear, labelled SN2 and SN7 respectively. SN2 has an activation energy E_C-E_t = 0.4 eV, and appear at low temperature, SN7 appear at high temperature and it has an activation energy E_C-E_t = 1.5 eV. The concentration of SN5, SN6 and SN7 increases with fluence. Its maximum value, however, is always less than 7 x 10^{13} cm^{-3} and it explains the good charge collection values (Fig 4.3) even after irradiation at the above mentioned fluences. The SN3 concentration increase

more rapidly than the near mid-gap levels. In fact SN3 level has a concentration that doubles SN5, SN6 and SN7 concentrations. SN3 energy value is similar to the activation energy of the level, found in the thermal activation energy plot. The increase of the concentration of this deep level explains the higher reverse current in the I-V characteristics. This effect underline that SN3 level has an important role in the reverse conduction of Schottky particle detector. Also the concentration of the SN1 deep level explains the parallel diode effect in the forward current of the I-V characteristics of the irradiated samples. The increasing of the concentration can cause the formation of shallow donor concentration gradient in the Schottky diode, and then a creation of diodes with different series resistance and barrier height [Sze].

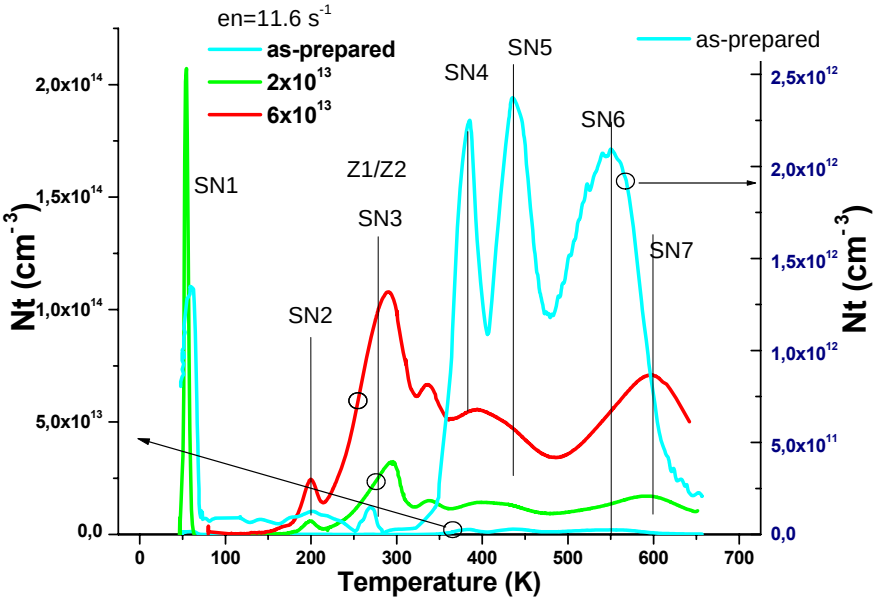

Figure 4.6 DLTS spectra of the irradiated samples up to 1 x 10^{14} n/cm^2 , on the right scale the spectra is showed as reference for the peak position.

The compensation effect of free carriers due to the presence in the gap of defect-related deep levels causes a drastic decrease of the value of the

capacitance. With fluences higher than 1 x 10^{14} n/cm^2 the capacitance reaches the geometrical value, with a linear dependence in function of the voltage.

Due to the significant compensation effect it is impossible to carry out DLTS measurements, in the case of irradiation with fluence higher than 1 x 10^{14} n/cm^2, the microscopic electronic properties of the neutron induced defects as activation energy E_t and capture cross section σ, have been determined by PICTS. The evolution of PICTS spectra acquired in the temperature range 75-650 K is shown in Figure 4.7 for the diodes irradiated at fluences from 2 x 10^{14} n/cm^2 to 8 x 10^{15} n/cm^2. Two main effects can be deduced by means of the evolution of the PICTS spectra. The normalized PICTS signal of the SN1 deep level decrease, increasing the neutron fluence, Matsuura demonstrated that high energy irradiation can cause doping deactivation [Matsuaara]. In our case, neutron irradiation would cause the nitrogen atoms migration from the hexagonal substitutional site. The kicked off nitrogen atoms can create complex with other point-like defect and then induce new intra-gap deep level in 4H-SiC. A new peak, labelled SN2b, appears. It has an activation energy of E_t = 0.49 eV but it is not possible to asses to which band is referred because it has been found by PICTS measurements, but considering its signature is possible to relate the SN2b to the Z_1 defect in the donor charge configuration. The dominant feature occurs between 400 and 650 K. In this range of temperature broad peaks can be observed which correspond to the deep level SN5, SN6 and SN7, as shown by the Arrhenius plot in Figure (4.8). The same levels detected by DLTS in the low fluence irradiated samples As the fluence rises to higher values ($\Phi > 10^{15}$ n/cm^2) the normalized PICTS signal of these levels increases and consequently their concentration. To identify which of them play the main role in the degradation of the detection properties the trapping time, τ, of these electron trapping centre are evaluated. Concentration, trapping time together with activation energy and capture cross-section for the most irradiated samples (Φ = 8 x 10^{15} n/cm^2) are reported in Table 4.2. It is obvious that the deepest levels SN6 and SN7 become dominant at the highest fluence because their trapping times are of

the same order of magnitude or lower than the transit time of the carrier in the device, which defines the time the electronic system will spend collecting any charged induced by the ionising radiation. In these cases part of the generated charge carriers, recombining at the defects, is lost and does not contribute to the collected charge signal [Martini]. It is worth noting that some of the deep levels (SN5 and SN6) increasing dramatically in concentration in the irradiated diodes, are present also before irradiation even if a very low density. On the contrary the most deep level, SN7, whose density reaches very high value (10^{16} cm^{-3}) was totally absent in the un-irradiated samples. In the range of temperature in which SN7 appears, the leakage current of the device increases drastically so the normalized PICTS signal is lower than SN5 or SN6.

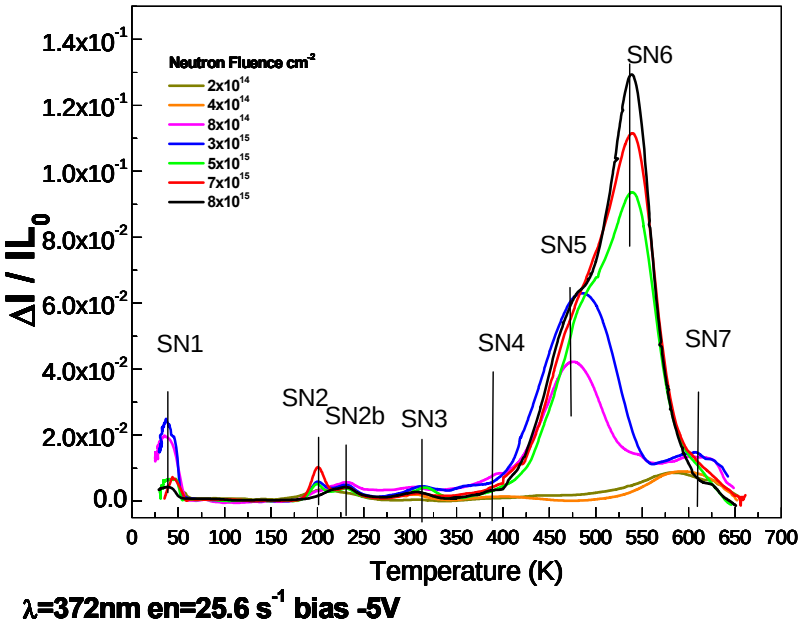

Figure 4.7 PICTS spectra of the high fluence irradiated samples

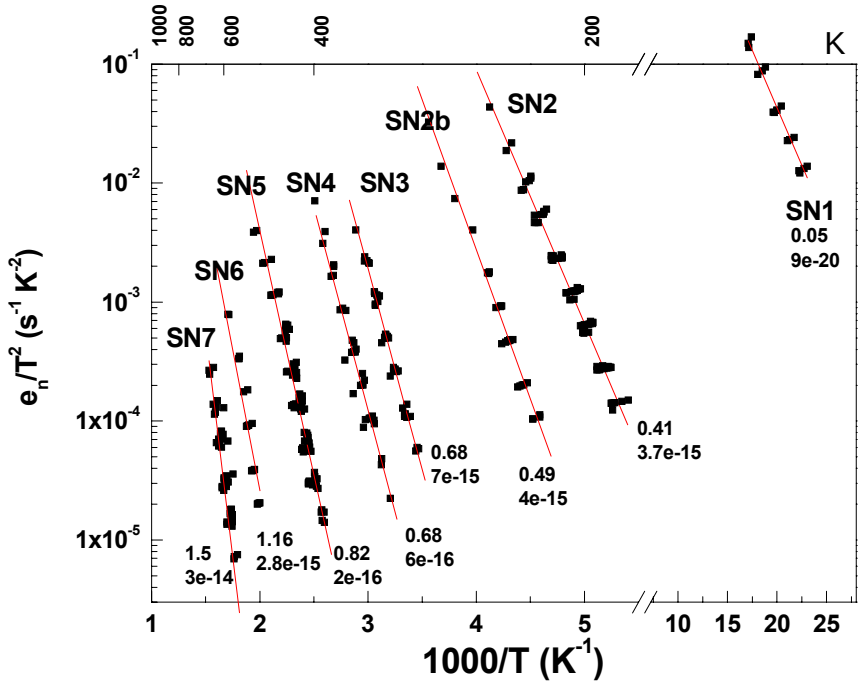

Figure 4.8 Arrhenius plot of the deep level, found in this analysis

To resume and highlight the effect of irradiation on the detectors, the normalized PICTS signal as a function of the neutron fluence have been shown in Figure (4.9a) and (4.9b) for the level SN1 and SN6. The dependence from fluence is not shown for SN7, since we really cannot evaluate precisely due to the high photocurrent values. It is possible to deduce that SN6 and SN7 have a similar behaviour. Figure (4.8 a) shows, also, the degradation of the forward current, that can be related to the decrease of the concentration of the SN1 doping donor and the strong increase of the SN6. Figure 4.8b indicates that the remarkable degradation of the CCE for high fluence, can be ascribed mainly to the strong increase of the concentration of the near mid-gap deep levels.

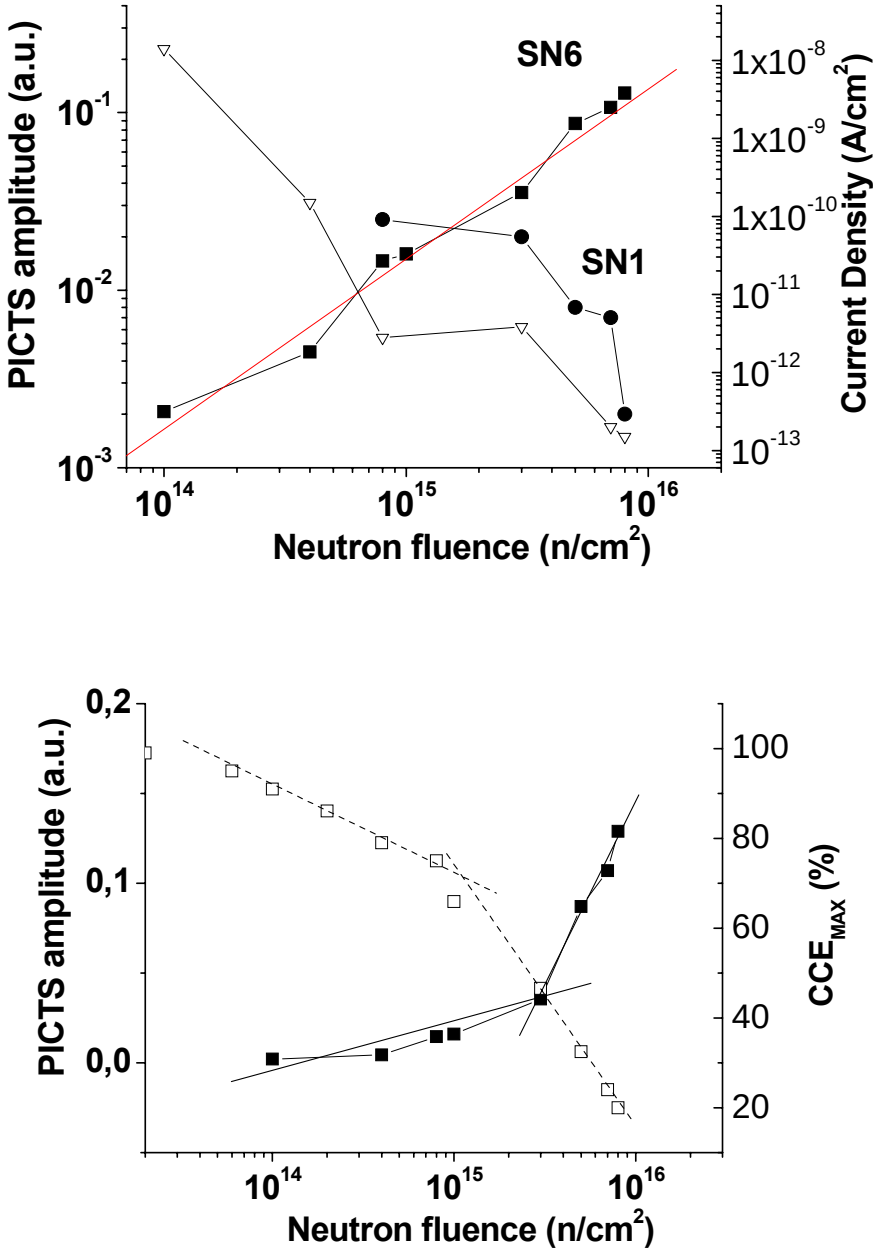

Figure 4.9a) PICTS signal of the SN1 (full circle) and SN6 (full square) as function of the neutron fluence,

compared with the forward current density (open triangle)

b) PICTS signal of the SN6 (full square) as function of the neutron fluence, compared with the charge

collection efficiency (open square)

Table 4.2 Resuming table of the deep level parameters

Deep levels Parameters					Comparison with published data	
Trap	E_C-E_t (eV)	N_t (cm^{-3})	σ (cm^2)	τ (sec)	Deep Level	Defect
SN1	0.06	10^{14}	8.8×10^{-20}	4.0×10^{-3}	N_{hs} [Chen]	N hex site
SN2	0.41	10^{14}	3.7×10^{-15}	1.4×10^{-7}	EH1, $Z_2^{0/+}$ [Hemmingson]	$V_{Si}^{-/--}$
SN2B	0.49	10^{13}	4.0×10^{-15}	1.9×10^{-7}	$Z_1^{0/+}$ [Hemmingson]	
SN3	0.68	10^{13}	7.0×10^{-15}	1.2×10^{-7}	Z1/Z2 [Hemmingson]	$V_{Si}+V_C$
SN4	0.68	-	6.0×10^{-16}		EH3 [Storasta]	-
SN5	0.82	10^{13}	2.0×10^{-16}	$7{,}6 \times 10^{-6}$	SI5 [Son]	V_{Si}^{+}
SN6	1.16	10^{15}	2.8×10^{-15}	4.0×10^{-9}	EH5 [Storasta]	V_C+V_{Si}
SN7	1.50	10^{16}	3.0×10^{-14}	3.4×10^{-11}	EH6/EH7 [Negoro]	V_C^{+}

4.2 Junction particle detector

4.2.1 ANALYZED SAMPLES AND IRRADIATION CONDITION

The diode structure (Fig. 4.10a), realized at CNR-IMM (Bologna, Italy), is based on a *p*+ emitter, ion implanted in the *n*-type epilayer. The *n*-type epilayer was grown at the Institute of Crystal Growth (IKZ, Germany) with thickness equal to 55 μm and a nominal donor doping $N_D = 2 \times 10^{14}$ cm^{-3}. A n^+ buffer layer with a thickness of 3 μm and a doping concentration of the order of $N_D = 10^{16}$ cm^{-3} was also grown between the bulk and the epilayers to improve the back-contact conduction. The crystal growth procedure is the same for the Schottky diode epilayer. A multiple aluminium implantation process was carried out at 305 °C, energy and fluence were varied in order to obtain an almost square box doping profile at the wafer surface with plateau and depth values equal to 4×10^{19} cm^{-3} and 0.45 μm, respectively. The energy and fluence are resumed in Table 4.3.

Table 4.3 Implantation parameters for the *p*+ emitter

p+ implant energy and dose	
Energy (KeV)	Dose (Ions/cm^2)
400	4.34×10^{14}
500	4.34×10^{14}
600	8.55×10^{14}

The annealing for the electrical activation of the implanted Al was performed in an inductive furnace at 1600 °C for 30 minutes. Diode diameter was between 150 and 1000 μm. Most of the diodes featured a 250 μm wide (with a superposition of 10 μm with the emitter), 1.4 μm deep, *p*- junction terminal extection (JTE) with a doping $N_A = 4 \times 10^{17}$ cm^{-3}. The JTE structure is synthesized to avoid the electrical field crowding at the edge of the barrier. The ohmic back contact was nickel silicide [La Via], and the top ohmic contact was an alloy of titanium and aluminium (28% - 72%) with a thickness of 400 um, the details for the contact process is reported in [Moscatelli01]. Figure 4.9b shows the photolithographic mask of the analyzed samples. The junction diodes have been irradiated at two different fluences (3×10^{15} cm^{-2} and 1×10^{16} cm^{-2}) of 1 MeV (NIEL equivalent in silicon) neutrons (Table 4.4). Details about the nuclear reactor used (TRIGA), the irradiation set up and procedure and the neutron spectrum can be found in [Nava02].

Table 4.4 Irradiation Condition

Neutron 1 MeV	
Sample	Fluence (n/cm^2)
J8	Not Irradiated
K7	3×10^{15}
M7	1×10^{16}

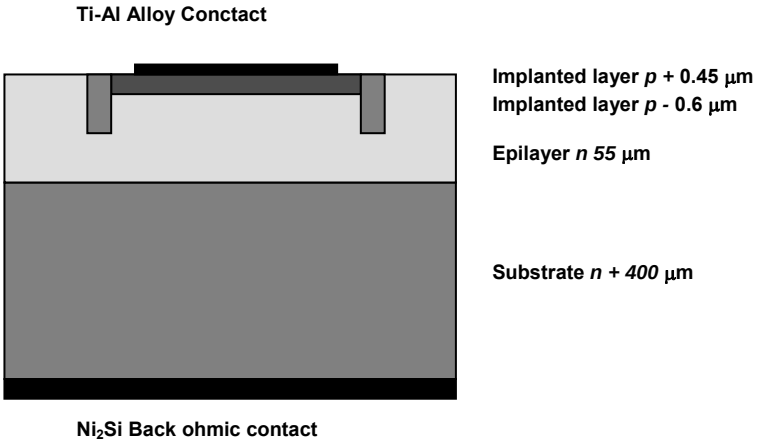

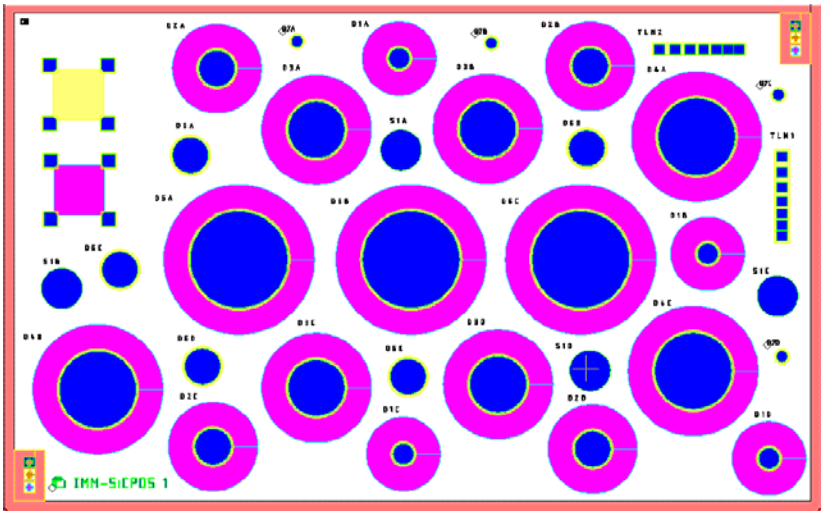

Figure 4.10 a) Cross section of the junction diodes analyzed in this thesis
b) Photolitographic mask of the analyzed samples

4.2.2 Defect analysis on un-irradiated samples by capacitance transient spectroscopy

The analysis of the defects of the un-irradiated detectors has shown interesting results due to the complex structure of the device. C-V characteristic (Fig

4.11a) of diodes, with different geometry shows different device parameters: the apparent carrier concentration $|N_D-N_A|$ goes from 1.2 x 10^{14} cm^{-3} to 1.7 x 10^{14} cm^{-3}, the built-in voltage ranges from 2.6 V to 3.2 V. Apparent concentration (Fig 4.11b) shows a strong carrier compensation effect in the near-surface region (about 5 micron). Normally in junction diodes this kind of effect is related to ion implantation tail, which causes a graded junction in the zone next to the ion implanted square box.

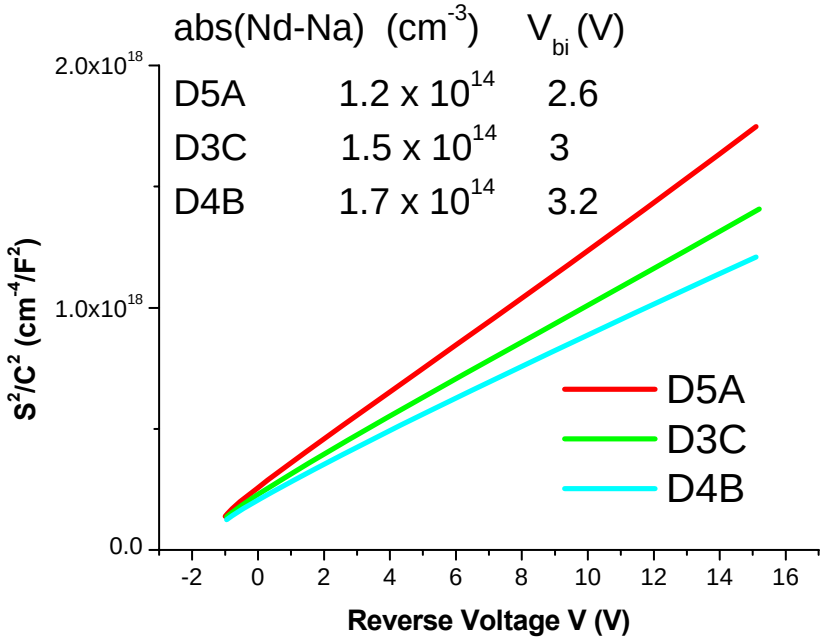

Figure 4.11 a) Capacitance-Voltage characteristics for diodes with different geometric parameters

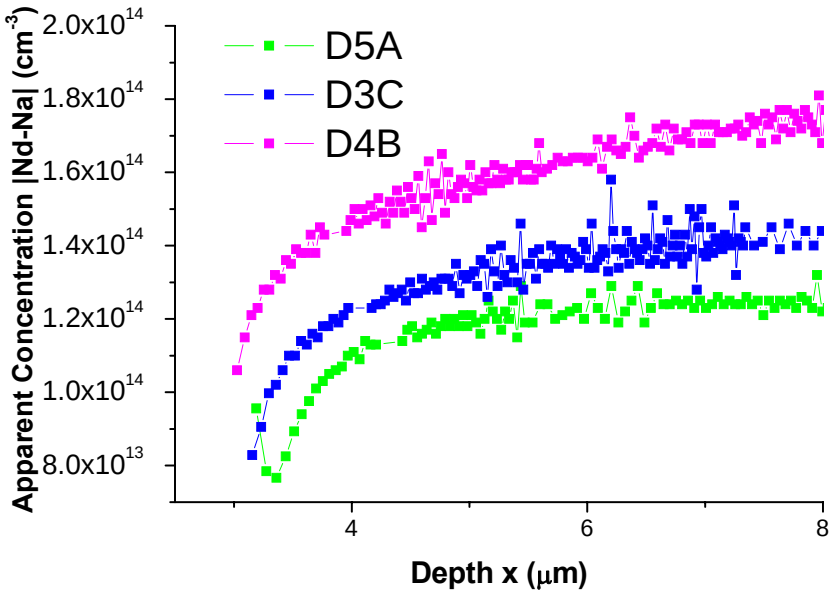

Figure 4.11 b) Apparent concentration as function of the depth

The implant profile for the aluminium ion implantation has been simulated in the way to compare with experimental data (Inset of Fig. 4.12). The simulation has been performed with a Person IV frequency method [Canino_Thesis][Janson]. Figure 4.12 shows the apparent carrier concentration as function of the depth for experimental data (full symbol) and for implantation tail simulation (open symbol). The simulated carrier concentration shows a compensation effect which is more surface-related (first 3 um under the implantation region) than the experimental data, it means that other acceptor levels participate to the compensation effect. Making the assumption that only one level participates to the carrier compensation effect it is possible evaluate the concentration profile of the deep level, as the subtraction of the experimental data with the simulated ones. The deep level concentration is about 5 x 10^{13} cm^{-3} at a depth of 3 μm, the concentration of the deep level decrease up to 1 x 10^{13} cm^{-3} at a depth of 5 μm.

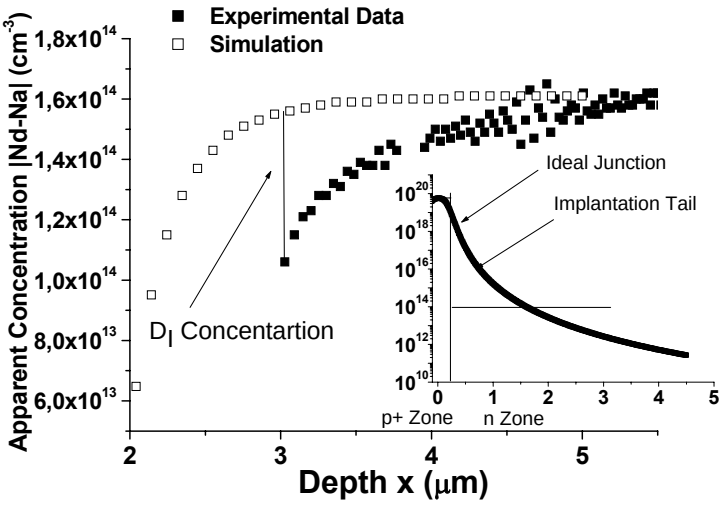

Figure 4.12 Comparison between simulated apparent concentration (open square), and experimental data (full square). In the inset is shown the implantation tail simulated with the Pearson model.

In order to identify the deep level related to the compensation effect, thermal activation energy measurements have been performed for different samples. The activation energy for all the analyzed diodes is $E_V + E_t = 0.4$ eV (Fig 4.13). In the simulated case the ion implantation tail is due only to the aluminium doping level, whose energy is ($E_V + E_t = 0.20$-0.25 eV [Troffer]), so it means that the compensation effect is related to a level which lies deeper in the band-gap in comparison with the aluminium dopant. This level can be induced by ion implantation but it is not related directly to the doping level due to the difference in energy.

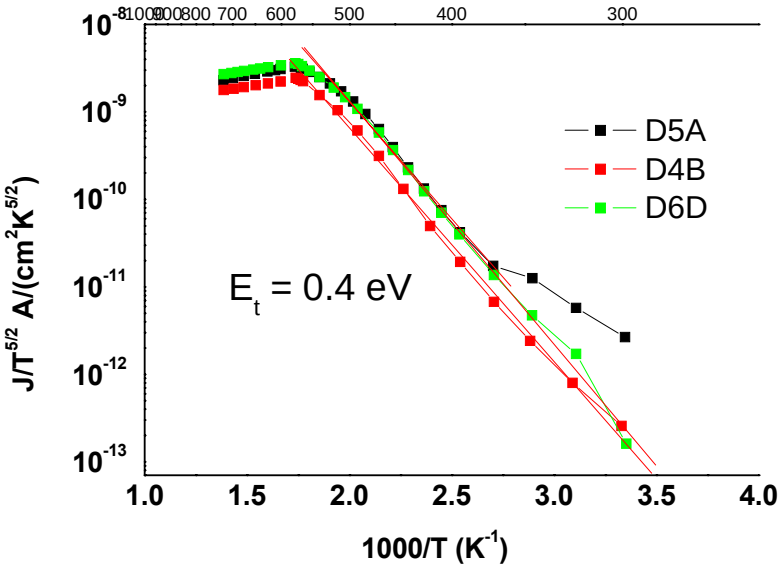

Figure 4.13 Thermal activation plot of different diodes, with a positive polarization in the way to analyze the same region probed by C-V measurements

Figure 4.14 shows different DLTS spectra performed with a fixed reverse bias (V_R = -10 V) and different filling pulse (V_{FP} from -7 V to 2 V). Three peaks appear in the DLTS spectra. All the levels are minority carrier centres, and they have been labelled SH1 and SH2. SH1 peak shows a shoulder that has been labelled SH1*. The SH2 peak appears only in minority carrier injection (i.e. with a forward bias filling pulse) meanwhile the SH1 peak and its shoulder SH1* appear in every recorded spectra. The concentration of SH1 ranges from $N_t = 6 \times 10^{13}$ cm^{-3} with the highest forward bias filling pulse to $N_t = 0.8 \times 10^{13}$ cm^{-3} with the highest negative reverse bias filling pulse. The profile of concentration, found by DLTS measurements, is in good agreement with the apparent carrier concentration found in the C-V analysis. So it possible to relate the carrier compensation effect to the presence of the SH1 deep level confirming the aforesaid hypothesis of a single deep level induced carrier compensation effect.

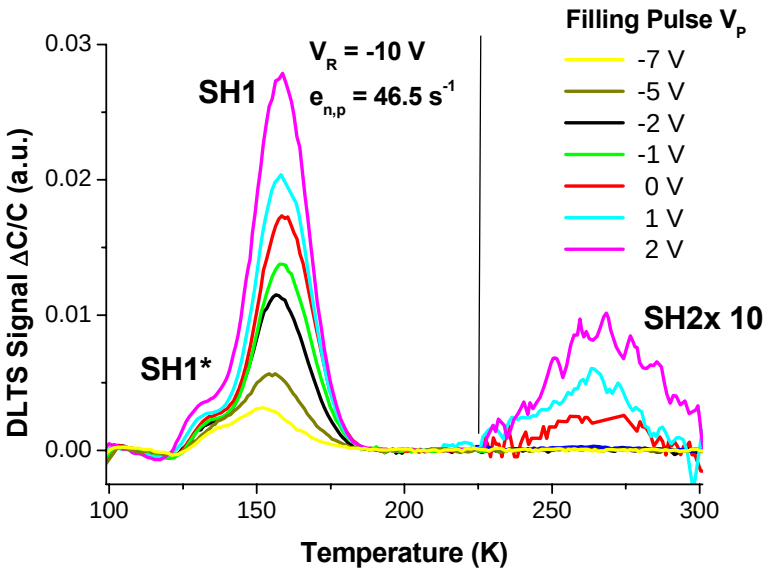

Figure 4.14 DLTS spectra with different filling pulse in order to achieve a profiling of the SH1 concentration.

The high concentration of the SH1 deep level, combined to the low net doping of the epilayers, forms a graded junction in the region next to the junction (as previously demonstrated, in the first 5 μm). The depletion region of the diode extends to the graded region, so it is possible to detect minority carrier deep level when the filling pulse is reverse bias. The signature, calculated by means of the Arrhenius plot, shows that the activation energy of the SH1 level is $E_V + E_t = 0.34$ eV and the capture cross section is $\sigma = 4 \times 10^{-14}$ cm^2. The activation energy of the SH1 peak is in good agreement with the dominating conduction level, found in the activation energy measurements. Making a comparison with literature the signature of the SH1 deep level is related to the D_1 center [Storasta02]. The D_1 center is normally found in *p* type epitaxial layer. The defect related to this center has not been still identified, many hypothesis have been proposed to explain the nature of this defect. The first proposed hypothesis was that D_1 center related defect was a carbon or silicon divacancy, associating the D_1 center with Z1/Z2 deep level but recently this theory has been excluded [Patrick], similarly Rao proposed a complex of a

silicon vacancy with a nitrogen atom in carbon site [Rao]. Galeckas et al. has related the D_1 center to a silicon core partial dislocation [Galeckas]. Fissel showed that the D_1 center is related to the presence of carbon dandling bonds, so he proposed a single carbon vacancy as cause of this deep level [Fissel]. Jones has proposed a stacking fault induced deep level [Jones]. The capture kinetic of the SH1, in our measurement, suggest a point-like defect, so it means that the partial dislocation core and the stacking fault hypothesis have to be excluded, due to the absence of a potential barrier around the defect. Storasta showed the electrical nature of the D_1 center by means of photoluminescence measurements. This deep level is a pseudo-donor; it means that, initially neutral, the deep level captures a hole due to its electronegativity, consequently the deep level has a positive charge, and then it captures an electron due to coulombian attraction, creating an excitonic bond between the electron and the hole. The exciton breaks up at low temperature and the electron is emitted around the 80 K, meanwhile the hole is emitted near room temperature. At room temperature the D_1 center emits holes that are the cause of aforesaid carrier compensation effect [Storasta02].

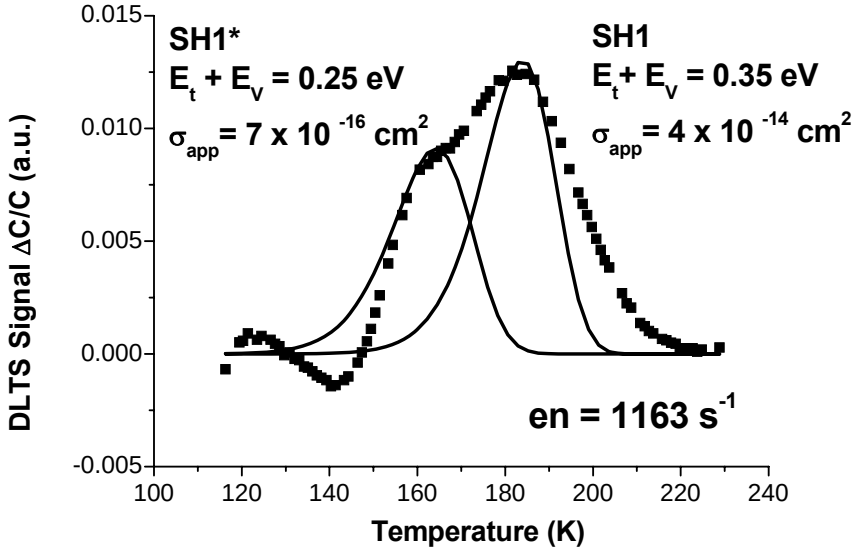

Figure 4.15 Deconvolution of the double peak SH1* and SH1, with the signature of the two deep levels extrapolated by the fitting regression

Figure 4.15 shows the deconvolution of the SH1* and SH1 peaks. SH1* is related to the aluminium implantation carrier band tail (the details of the signature has been showed in Fig 4.15). The different concentration profiling of SH1* and SH1, as function of the filling pulse, shown in Fig 4.14, demonstrates that the carrier compensation effect is not related to the aluminium doping shallow level. In fact the concentration of SH1* is always under $N_t = 1 \times 10^{13}$ cm^{-3}. The peak SH2 shows an activation energy $E_V + E_t = 0.5$ eV and a capture cross section $\sigma = 1 \times 10^{-15}$ cm^2. Due to its signature, it has been related to boron related D center. The boron is a typical residual impurity in silicon carbide, the low SH2 concentration ($N_t = 1 \times 10^{11}$cm^{-3}) is a demonstration of it.

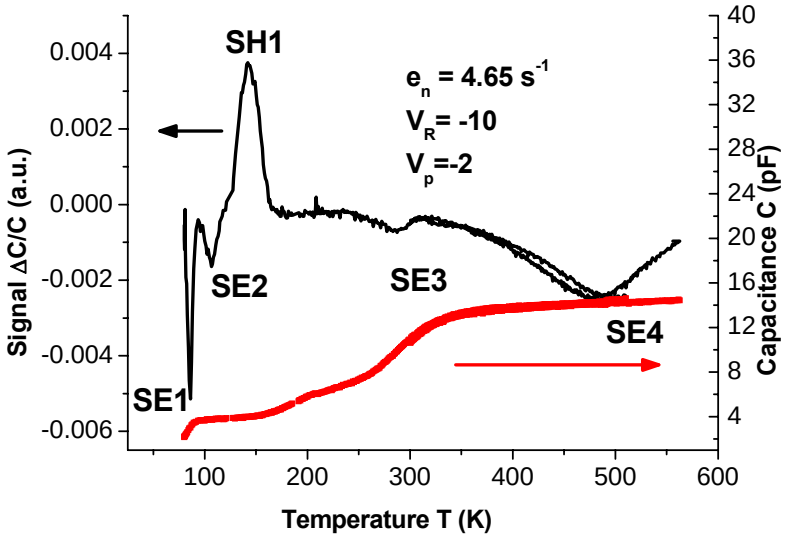

Figure 4.16 DLTS spectra of junction diode. On the right scale the behaviour of the capacitance as function of the temperature.

Figure 4.16 show the DLTS spectra in a large temperature range (80 -550) K, over the aforesaid minority carrier deep levels, four majority carrier deep levels have been found. They have been labelled from SE1 to SE4 with the

increasing of the temperature peak. Table 4.5 resumes the deep levels parameters.

Table 4.5 Resuming table of the majority carrier deep levels parameters

	Activation Energy (eV)	**Capture Cross-Section (cm^2)**	**Attribution**
SE1	0.18	$(2 – 4) \times 10^{-14}$	Titanium [Lebedev]
SE2	0.21 – 0.24	$(2 - 3) \times 10^{-14}$	Single-layer Stacking Fault [Galeckas]
SE3	0.62 – 0.67	$(3 – 7) \times 10^{-14}$	Z1/Z2 [Hemmingson]
SE3*	0.5	1×10^{-16}	$Z_1^{0/+}$ [Hemmingson]
SE4	1.2	1×10^{-13}	EH5 [Storasta]

Thermal activation measurements (Fig 4.17) have been performed at the detector working condition (i.e. full depletion voltage reverse polarization) to achieve a better understanding of the device. The measurements have been carried out for different diodes. The activation energy ranges from $E_t = 0.6$ eV, for the diodes with JTE structure, to $E_t = 0.7$ eV, for diodes without. It is possible to relate the deep level found by means of thermal activation measurements with the SE3 deep level found in the DLTS analysis.

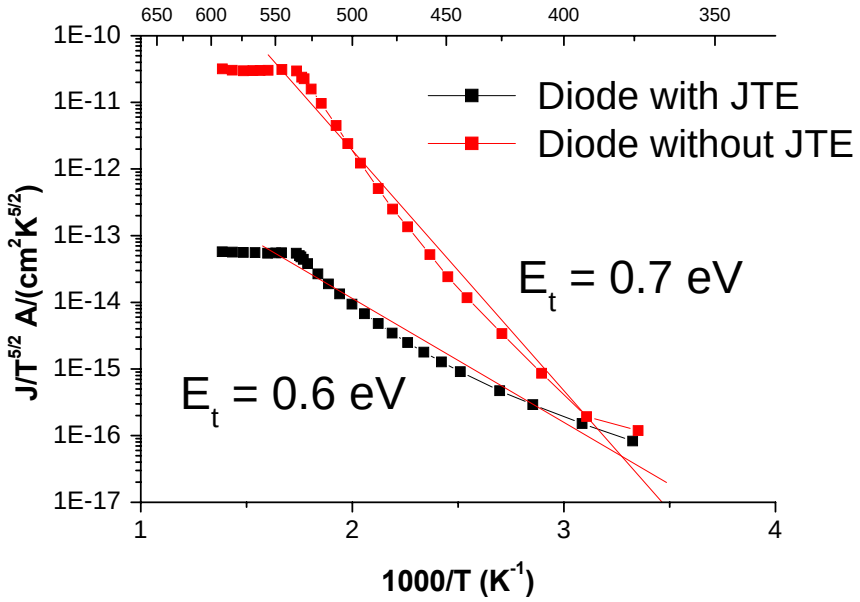

Figure 4.17 Thermal activation plot with a full depletion reverse polarization, in order to analyze the working condition of the detector

From a qualitative analysis it appears clearly that the concentration of the reverse bias conduction dominating level is higher in the diodes without the JTE structure. A DLTS analysis has been performed on this group of diodes, named D6. Figure 4.18a shows the DLTS spectra for a diode without JTE structure with different polarization condition. Only in the spectrum recorded with a reverse voltage V_R = -3.5 V and a filling pulse V_{FP} = +1.5 V, the SE3 peaks and a new shoulder SE3* appear. It means that the concentration of these two levels is not constant across the device; the deep levels concentration increases, getting next to the surface. This effect is detectable only in the D6 group diodes because, the electrical field of this structure expands laterally, meanwhile in the diodes with the JTE structure the electrical field is shaped in order to create a perfect square depletion region, without any lateral expansion. In Figure 4.18b the deconvolution of the SE3 and SE3* peaks is shown with the signature of both peaks. Making a comparison with literature it is possible that SE3 and SE3* are related to the

well known Z1/Z2 center. SE3* has been found by Hemmingson to be related to the Z1 center with another charge state[Hemmingson]. In the way to study a more surface-related region it has been carried out a profiling of the SE3 deep level concentration on a Schottky diode grown on the same wafer.

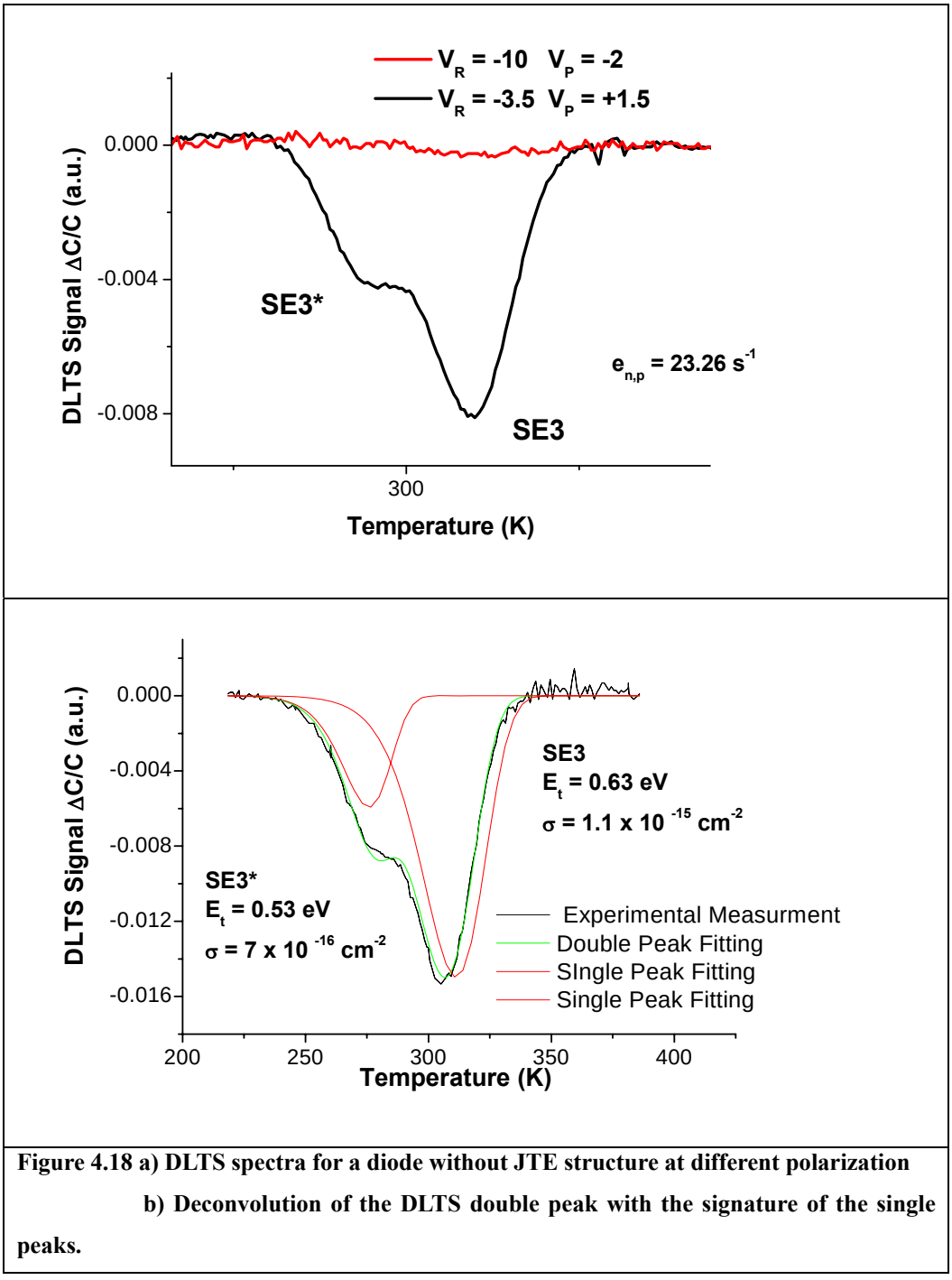

Figure 4.18 a) DLTS spectra for a diode without JTE structure at different polarization b) Deconvolution of the DLTS double peak with the signature of the single peaks.

Fig 4.19 shows the dependence of the concentration of the SE3 deep level as function of the distance from the barrier for the Schottky and for the D6 group junction diode. It is possible to see that the junction diode has an higher concentration of the SE3 deep level in comparison with the Schottky diode, it is possible to propose a hypothesis that the high-temperature annealing induce the migration to the surface of the defects that cause the SE3 and SE3* deep levels. Rigutti et al. have demonstrated the intrinsic nature of the Z1/Z2 defect, it notes that high-temperature annealing induce a migration of the intrinsic defect to the surface [Rigutti]. Pintillie et al. have proposed an nitrogen related complex to explain the nature of Z1/Z2 [Pintillie]; in our case the mechanism to create a complex, involving a nitrogen atom in the substitutional site, results unfavourable because the aluminium ion implantation, normally, induces a nitrogen doping deactivation (i.e. a kick-off mechanism from the sustitutional site), so the Z1/Z2 concentration should decrease in zone next to the junction barrier that is contradictory with our results.

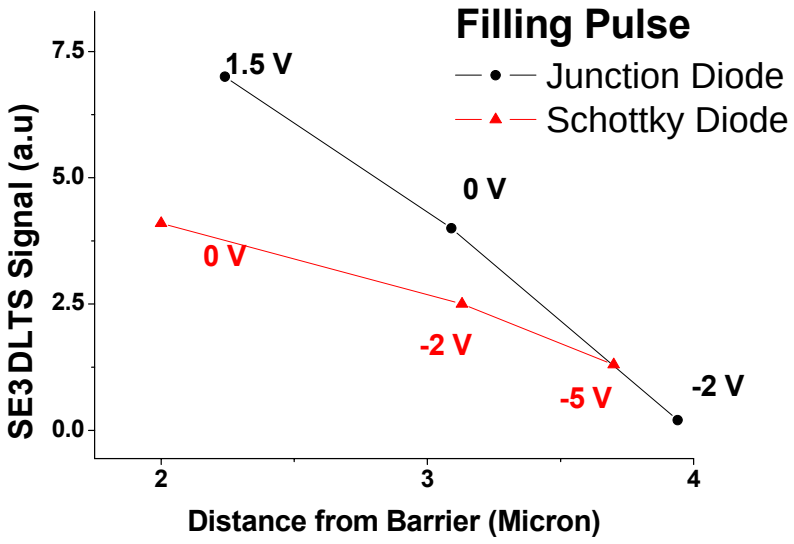

Figure 4.19 Profiling of the SE3 DLTS signal for the junction diode (black symbol), and for the Schottky diode (red symbol)

Another interesting finding in the Schottky barrier analysis is related to SE2 peak, Figure 4.20a shows some DLTS spectra, recorded with different emission rate. It notes that the SE2 peak amplitude shows a dependence on the measurement emission rate. This effect, normally, depends on the existence of a potential barrier around the defect as explained by Omling [Omling]. Line defects as dislocation or stacking fault cause this kind of effect. Figure 4.20b shows the filling kinetic of the SE2 defect with different filling pulse. By means Equation (4.1) is possible to calculate the potential barrier around the defect (4.20c).

$$q\phi(t_p) = k_B T\left[\ln(N_t - n_t)t_p n < v_{th} > \sigma_n\right] - \ln\left(t_p \frac{dn_t}{dt_p}\right) \tag{4.1}$$

So due to the SE2 filling kinetic behaviour it is possible to relate it to the single-layer stacking fault [Galeckas]. In the *p+/n* the effect of the dependence to the emission rate is not detected due to the superposition with the SH1 peak.

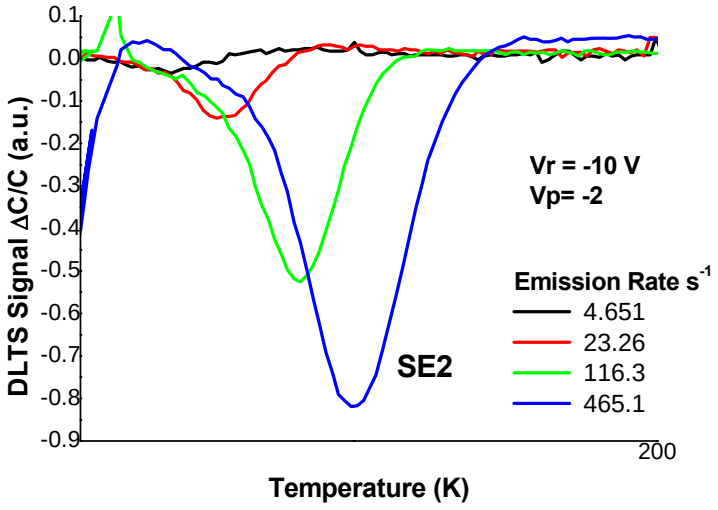

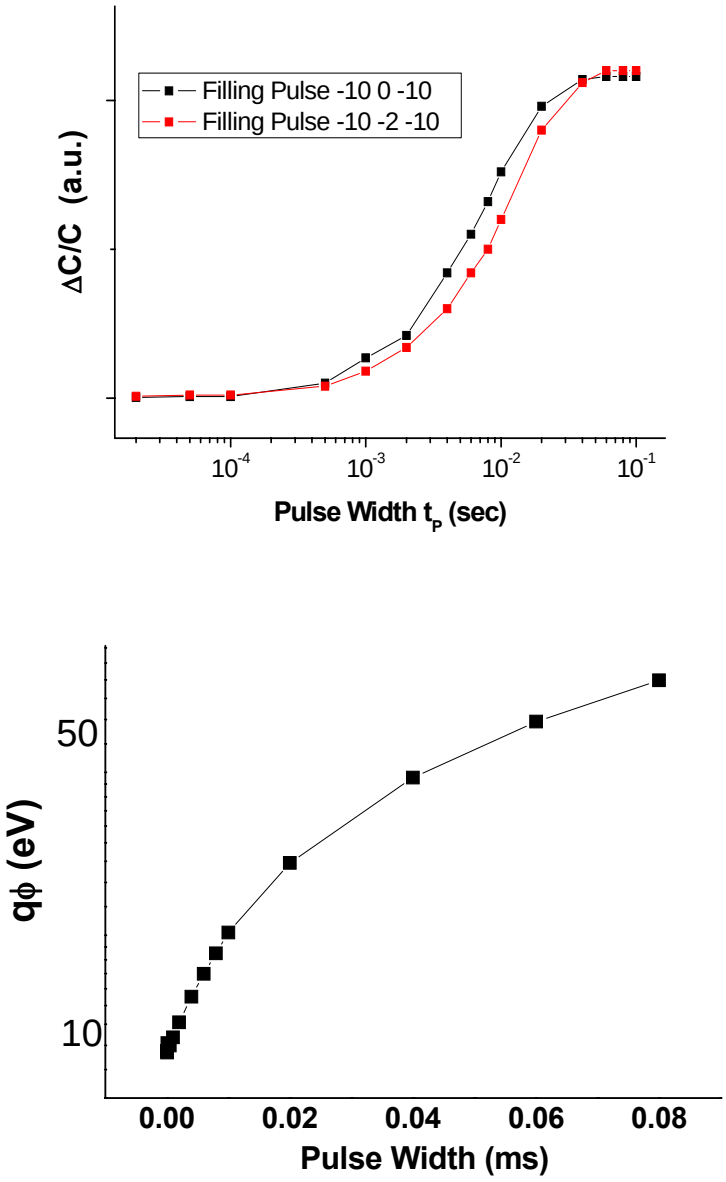

Figure 4.20 a) DLTS spectra of the SE2 peak showing the dependence of the peak amplitude as function of the emission rate

b) Profiling of the peak amplitude with different pulse width

c) SE2 Defect potential barrier as function of the pulse width

4.2.2 DEFECT ANALYSIS OF UN-IRRADIATED SAMPLES BY CATHODOLUMINESCENCE

Catholuminescence analysis of the un-irradiated samples have been carried out with different electron beam parameters and at different temperature; in the way to study the implantation induced defect in silicon carbide junction diodes. In the first part CL spectroscopy and microscopy have been performed at room temperature (RT) with an electron accelerating voltage equal to V_B = 10 kV, and an electron current density J_B = 1700 pA on the *p*+ and *p* Van der Paw structures, in the way to avoid the effect of screening due to the top ohmic metal contact. The electron depth, related to an accelerating voltage of V_B = 10 kV, has been calculated in two different ways, the first one is the maximum electron depth in the material by means of Equation (3.40) and it results R_{eMAX} = 750 nm; the second method is the Montecarlo-simulated electron distribution peak and it results R_e = 500 nm [CASINO]. This accelerating voltage has been chosen to probe only the implanted layer. CL micrograph has been recorded with a 150 X magnification; low magnification micrograph has been used in the way to analyze large area to achieve the spatial distribution of defects found in CL spectra. The *p*+ Van der Paw (VdP) structure has the same doping density and layer thickness of the p+ layer in the diodes, p one has the parameters of the JTE structure. In the second part of this analysis it has been carried out a comparison between the un-implanted zone of the epilayer and the Van der paw structures. In the way to achieve CL signal from the epilayers, it has been uses high accelerating voltage (V_B = 30 KV) and high electron beam current density (J_B = 2.1 nA). To increase the CL signal the spectra has been recorded at low temperature (50 K). Operating at low temperature induces sharp transitions which allow recognizing the defect clearly. Figure 4.20a shows the CL spectra of the *p*+ Van der Paw structure it notes the appearance of two broad band centred at 2.5 eV and 1.7 eV, respectively. No band-to-band transition is revealed, due to the indirect band-gap of the 4H silicon carbide. The

monochromatic CL micrograph, recorded at 1.7 eV and 2.5 eV, are shown in Figure 4.20b and 4.20c, respectively, they are taken on the same area of the sample in the way to understand the defect-induced by aluminium implantation. It notes that the 1.7 eV band is homogeneous in the analyzed area; the white spots in the micrograph are induced by thermal noise due to RT-CL measurements. The 2.5 eV broad band appears only in the Van der Paw structure, so it is induced by implantation. Similar results have been recorded for the p type Van der paw structure (Fig. 4.22a). The band at 2.5 eV shows high CL signal intensity, and a new shoulder centred at 2.7 eV becomes visible. The 1.7 eV band has small signal that becomes difficult to detect. The two micrograph (Fig.4.22b and 4.21c) shows the spatial distribution for the 2.5 eV and 2.7 eV bands. It is possible to note that both the bands are related to the implanted zone. A problem of superposition of the peak can be induced due to short distance in energy, but it is clear that both the peaks are due to the aluminium implantation.

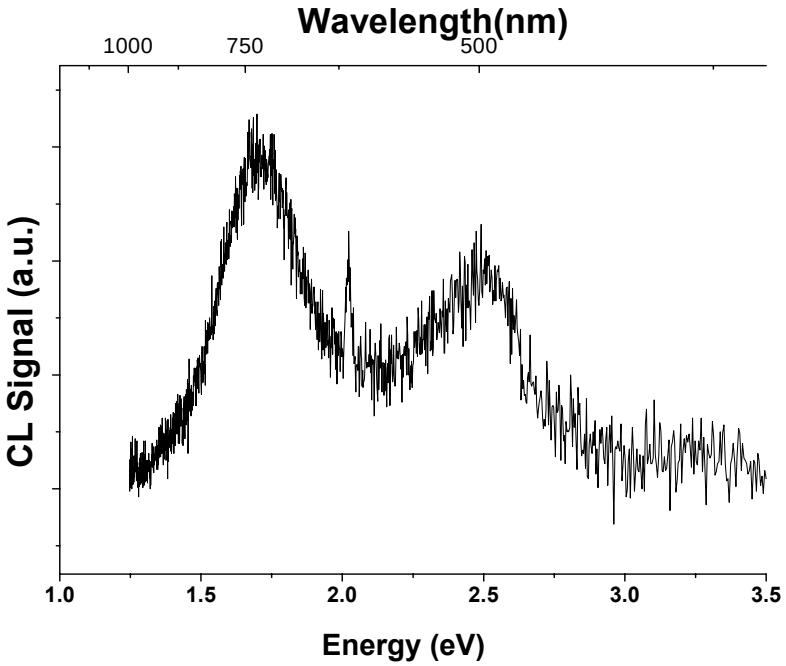

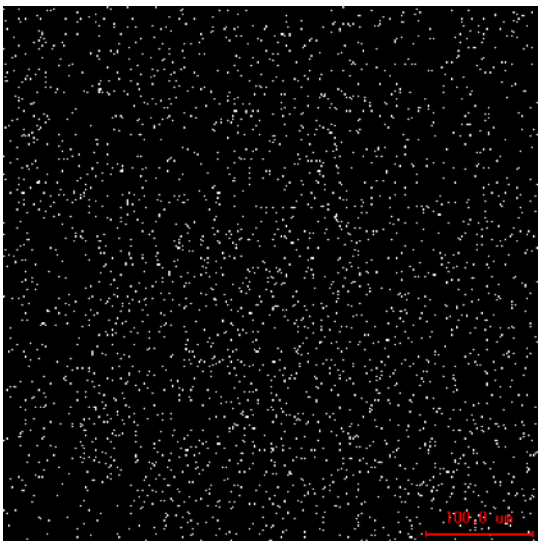

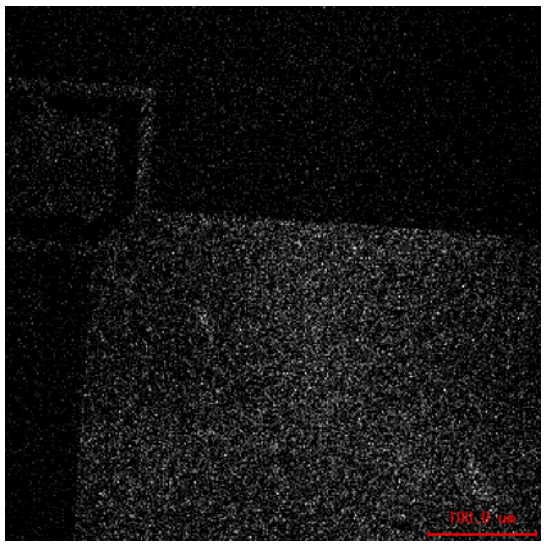

4.21 a) CL spectra of the *p*+Van der Paw structure

b) Monochromatic micrograph, performed with an energy of 1.7 eV, the defect distribution is homogeneous

c) Monochromatic micrograph, performed with an energy of 2.5 eV, the defect distribution is related only in the implanted area

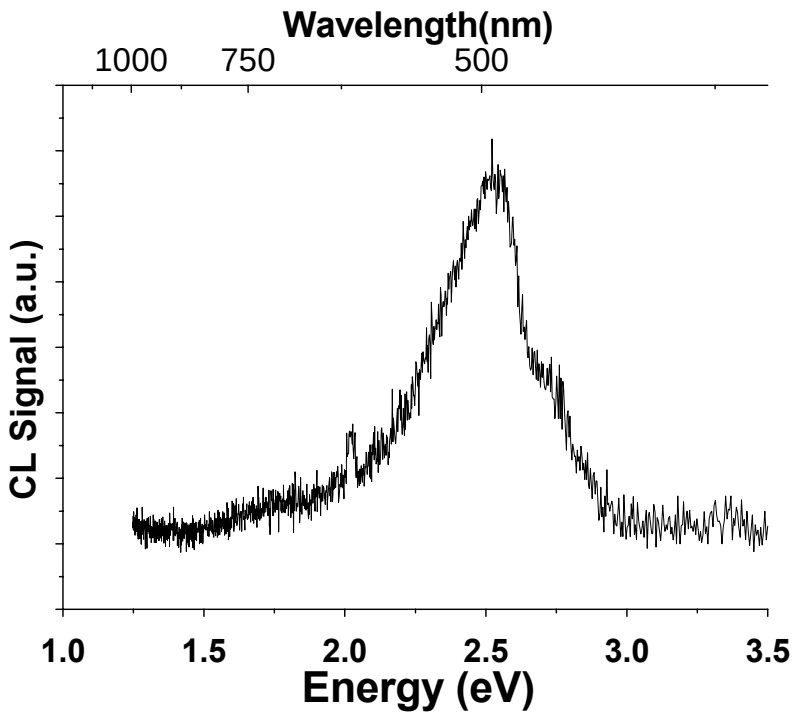

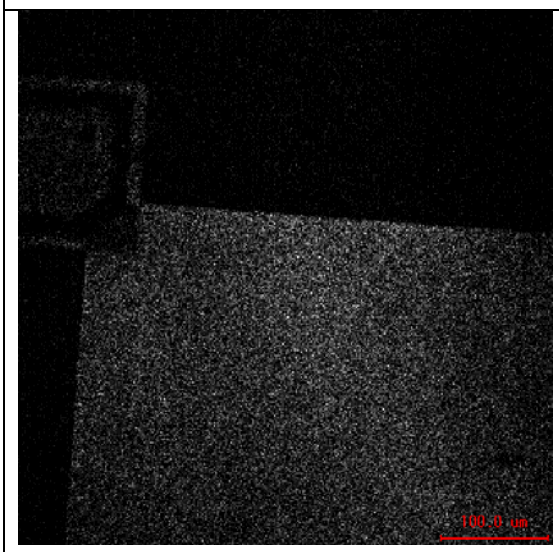

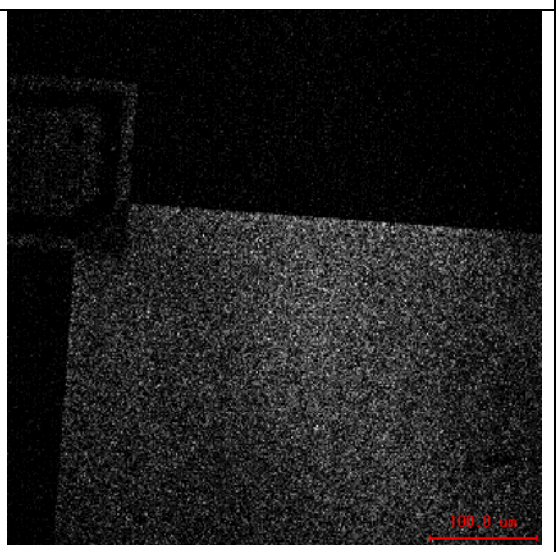

4.22 a) CL spectra of the *p* Van der Paw structure

b) Monochromatic micrograph, performed with an energy of 2.5 eV, the defect distribution is related only in the implanted area

c) Monochromatic micrograph, performed with an energy of 2.7 eV, the defect distribution is related only in the implanted area

Making a comparison with the foreshown DLTS measurements, it is possible to propose a correlation between the SE3 and SE3* deep levels and the 2.5 eV and 2.7 eV broad band, respectively, due to the similar values of energy. It seems that aluminium implantation increases the concentration of these deep levels in the implanted layer. This hypothesis is in agreement with SE3 concentration profiling previously shown (Fig 4.19). The higher intensity in the *p* type Van der Paw structure is due to the larger thickness of this layer. So the electron penetration sphere is completely contained in the implanted layer, in this way more electron-hole pair can recombine with the aforesaid mechanism. The 1.7 eV broad band that is homogeneous in the epilayers has been attributed to the presence of the EH6/7 intrinsic defect in silicon carbide. This level has been not found in the previous DLTS analysis due to the high temperature at which it appears in the DLTS spectra [Negoro]. A comparison between low-temperature CL (LT-CL) measurements on the epilayers and on the Van der Paw structures will explain better the implantation induced transition. Figure 4.23 shows the LT-CL spectra for the epilayer. The electron-hole pair generation is enhanced by the high accelerating voltage and the high beam current density, in fact different sharp peaks appears in the CL spectra. The maximum electron penetration depth with 30 kV is R_{eMAX} = 4.1 um, and the Montecarlo–simulated electron distribution peak is at R_e = 3.3 um. It notes a strong sharp band-to-band transition centered at 3.24 eV, with a shoulder at 3.12 eV related to nitrogen donor-to-free-hole transition. The value for the band-to-band transition is in agreement with the indirect band-gap transition for silicon carbide. The band-gap energy has been calculated to be E_G = 3.29 eV, so it means that the phonon energy in the band-to-band transition is $k_B\theta$ = 0.05 eV, in agreement with literature [Galeckas02]. The small transition centred at 2.94 eV has been identified with the non-phonon L_1 line associated with D_1 center [Mitani]. This result is really important because it clarifies that the D_1 center, found in DLTS analysis, exists also before the aluminium ion implantation. In order to clearly identify the different emissions contributing to the deep level luminescence of the SiC epilayers, a

Gaussian deconvolution of CL broad band has been carried out. Deconvolution of the mentioned band indicates the complex character of the deep level CL emission, which is actually composed by three bands. The emissions appear peaked at 2.80, 2.56 and 2.43 eV. The bands at 2.80 eV and 2.43 eV can be related to donor-acceptor pair recombination mechanism, the first is related to nitrogen-aluminium (N-Al DAP), the second one at the (N-D center DAP), respectively. The band at 2.56 eV is attributed to acceptor-to-free-electron Z1/Z2 transition.

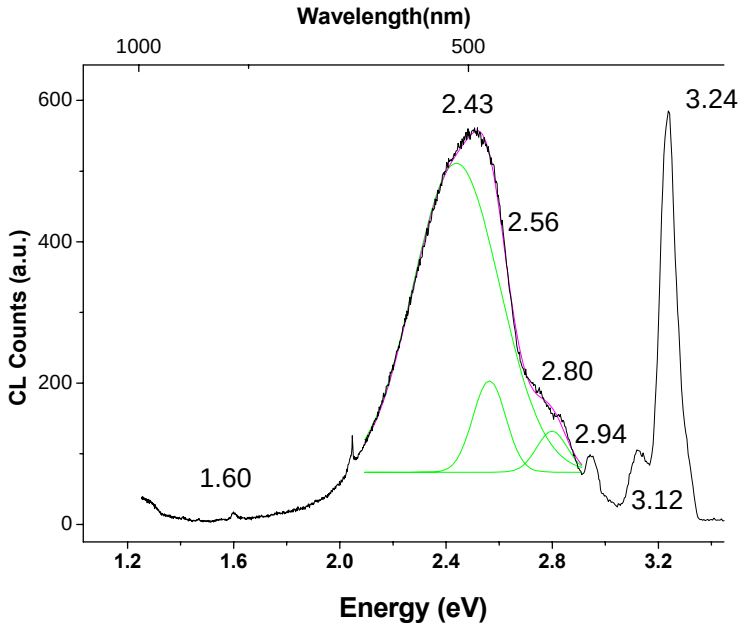

Figure 4.23 CL spectra of the un-implanted epilayers. The broad band has been deconvolved with different Gaussian peaks (green lines)

Fig 4.24 shows the CL spectra for the VdP structures compared to the epilayers. It notes that the band-to-band and the nitrogen related transition decreases in the implanted areas with the increasing of the aluminium concentration; the band-to-band transition intensity decreases due to the lattice disorder induced by the ion implantation. The 3.12 eV transition decreases due to the deactivation of the nitrogen doping as demonstrated by

Aberg, the ion implantation induces a deactivation of doping of the epilayers [Aberg]. The non-phonon L_1 line increases in intensity. This behaviour confirms the D_1 center concentration enhancement due to the ion implantation, found in the DLTS analysis. A new sharp band appears centred at 2.85 eV in the *p*+ Van der Paw structure, this band is related to the aluminium acceptor-to-free-electron. The N-Al DAP band increases in intensity. Both of the aforesaid peaks intensities are relative higher in the *p*+ Van der Paw structure. The broad band (centred at 2.72 eV in the *p* type VdP and at 2.66 in the *p*+ type VdP, respectively) is related to the Z1 defect, this band can be related to the SE3* deep level found in the DLTS analysis. The energy blue-shift in the *p*+ type VdP, is probably due to a convolution with Z1/Z2 band. As expected the ion implantation does not induce an increase in the intensity of the 2.43 eV band.

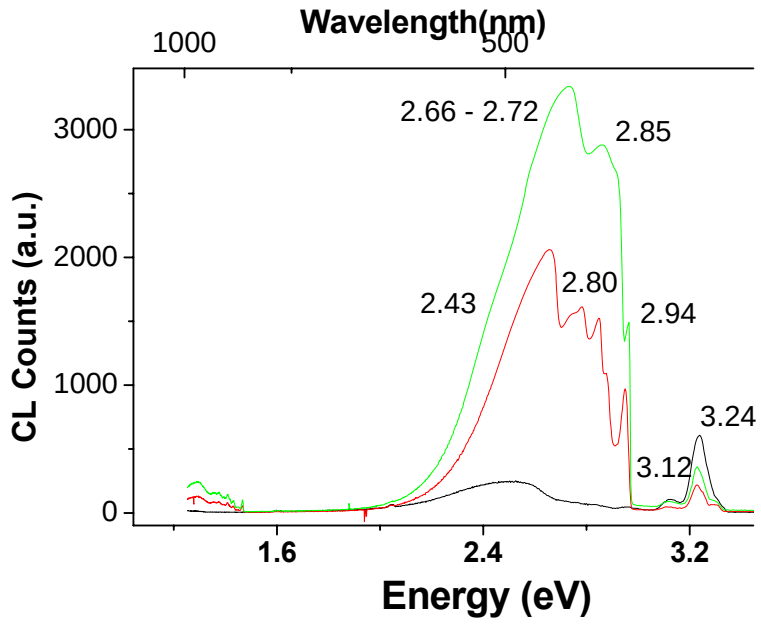

Figure 4.24 Comparison of the CL spectra of the epilayers (black line), *p*+ VdP structure (red line), and *p* VdP structure (green line)

4.2.3 EFFECT OF IRRADIATION: TRANSPORT PROPERTIES EVOLUTION.

The effect of neutron irradiation has the same effect on the transport properties of the junction diode as on the properties of the Schottky diodes. In the case of the *p+/n* it has been analyzed only high fluence irradiated detector. Forward current is affected by a carrier compensation effect that induces a decrease up to equality between forward and reverse current (Fig 4.25a). The thermal activation plot (Fig. 4.25b) shows a different result from the Schottky analysis. The thermal activation energy of the un-irradiated detector has been evaluated around E_a = 0. 6 eV; the activation energy for the irradiated samples is moved toward mid-gap energy and is E_a = 1.6 eV.

The effect of the neutron irradiation on the CCE properties has been reviewed in [Moscatelli].

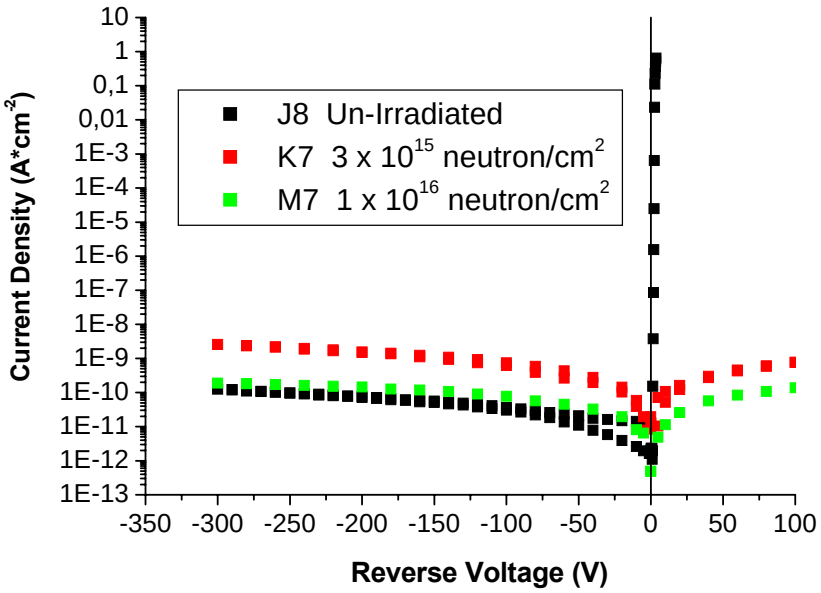

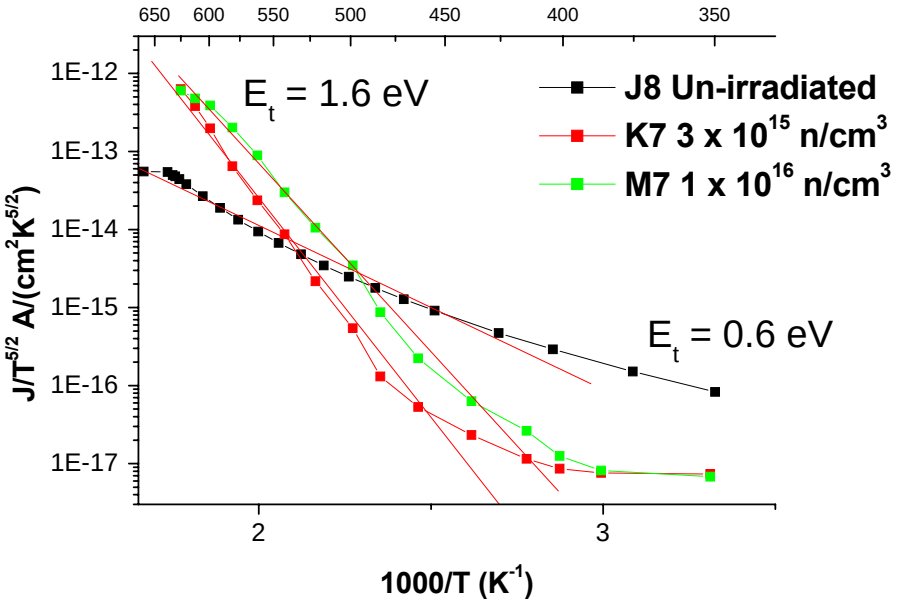

Figure 4.25 a) J-V characteristics for all the analyzed samples

b) Thermal activation plot, it notes the different behaviour between un-irradiated and irradiated

sample

4.2.4 EFFECT OF IRRADIATION BY PICTS, CL AND SE IMAGINING.

The evolution of PICTS spectra acquired in the temperature range 150-450 K is shown in Figure 4.26a for all the analyzed diodes and in the high temperature range in Figure 4.26b for irradiated diodes, respectively. The un-irradiated junction detector has low reverse current which allows performing PICTS measurements at low temperature; but, at high temperature, the reverse current increases up to reach the amplifier limit of the PICTS apparatus. Three main effect can be deduced by means of the evolution of the PICTS spectra. The SE1 PICTS signal increases with the neutron fluence. The SH1 and SH1* peaks disappear in the irradiated samples. The complete disappearing of these two peaks will be explained later, considering also the CL analysis. The other

effect is the appearance of the S5 peak at high temperature. This deep level has an activation energy about E_t = 1.6 eV, which is in agreement with the activation energy, found in the thermal activation energy plot. The activation energy and the capture cross-section of the S5 deep levels are affected by a high associated error because the peak temperature evaluation is difficult due to the photo-generated current saturation. This effect is evident due to the plateau after the peak. This level has been found in the CL analysis of the un-irradiated samples so it notes that S5 exists also before the neutron irradiation. S5 deep level can be related to EH6/7 deep level. The comparison between PICTS and CL permits to clarify the activation energy value of this deep level.

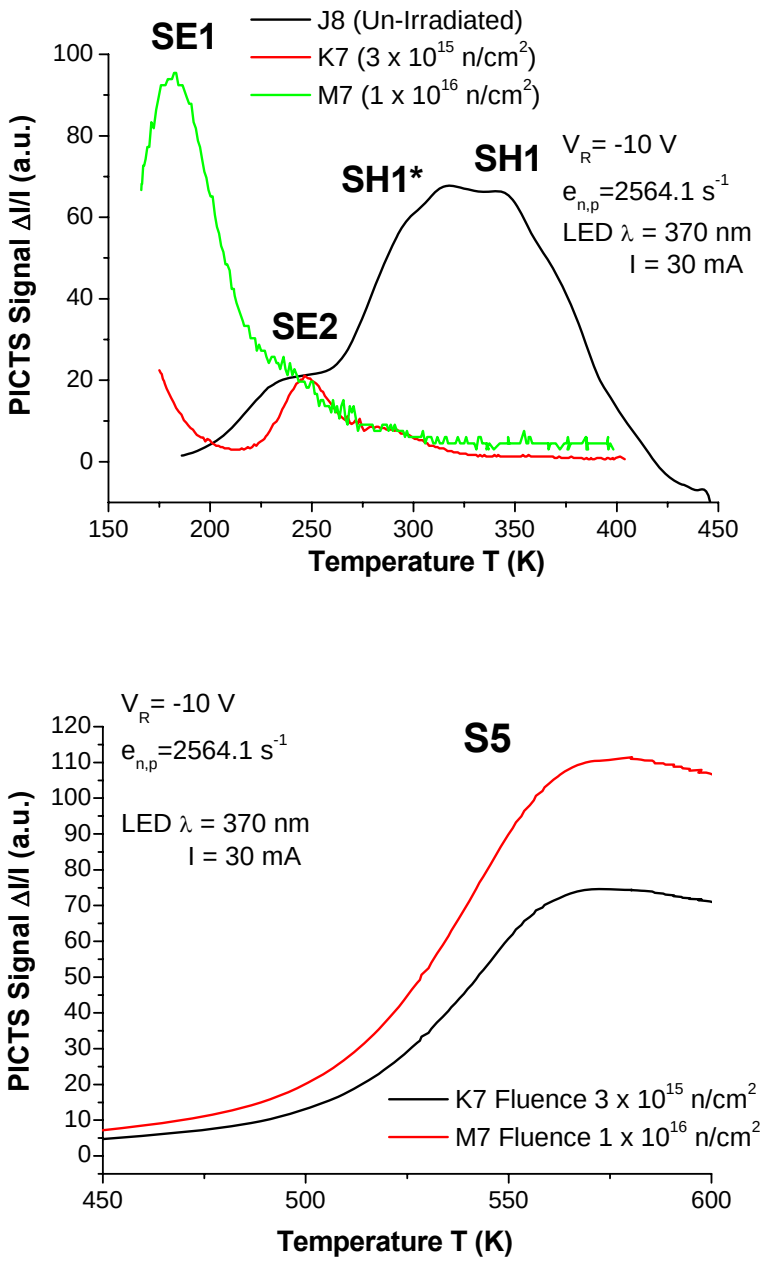

Figure 4.26 a) PICTS spectra for all the analyzed samples in the low temperature range
b) PICTS spectra for the irradiated samples in the high temperature range

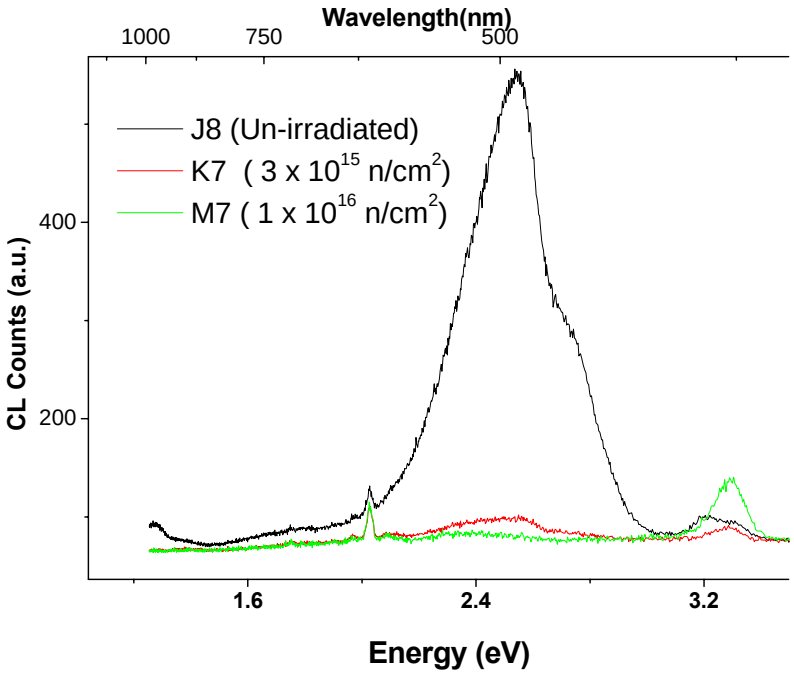

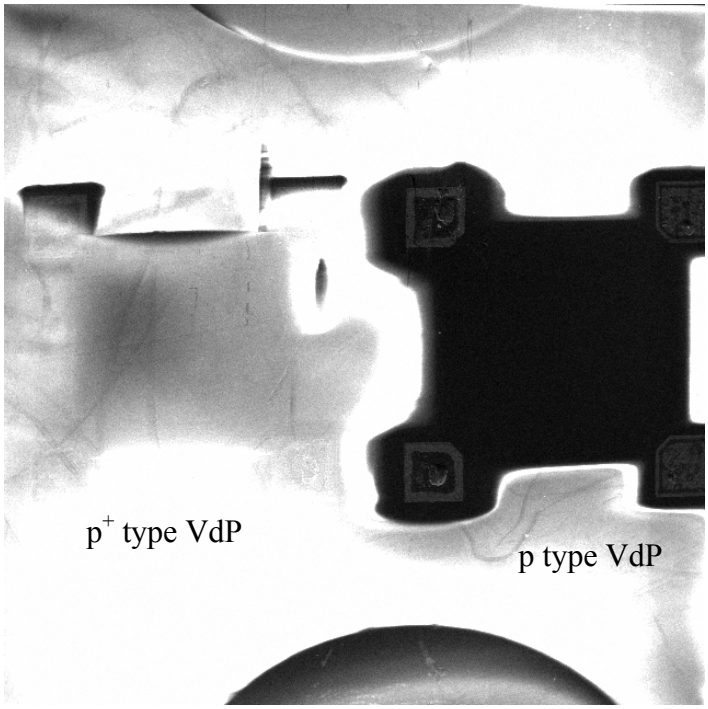

Figure 4.27 a) CL spectra for all the analyzed samples

b) SE Image of the Van der Paw structures of the K7 sample.

The implantation induced broad band decrease in intensity, increasing the neutron fluence (Fig 4.27a). It is possible to note a small band in the K7 sample, which totally disappears in the M7 sample. In the spectra of the M7 sample remains only the band due to the N-D center DAP centred at 2.5 eV. It is interesting to note that the band-to-band transition increases as function of the neutron fluence. In Figure 4.27b is shown a secondary electron image of the K7 Van der Paw structures. This image shows a strong effect of charging of the sample. The p^+ type VdP structure is more affected by the surface charging than the p type. The results obtained from PICTS analysis, CL measurements and SE image suggest the formation of an insulating layer at the surface. The high resistivity induces the charging of the insulating layer underlined in the SE image. The charging causes also a screening which avoids probing the charged region next to the surface. From the CL evolution, shown previously, it is possible deduce that the thickness of the layer varies with the neutron fluence because in the K7 CL spectrum the implantation induced broad band still appears. It also suggests that the insulating layer, with a neutron fluence of $\phi = 1 \times 10^{16}$ n/cm^2 , is thicker than the implanted square box and the related graded junction. In the PICTS analysis the formation of an insulating layer at the surface shifts the depletion region of the device to a larger depth. In the case of the K7 sample the depletion region overlap slightly the aforesaid graded junction, but the sensibility of the PICTS characterization does not allow to detect the SH1 and SH1* deep levels.

Conclusions

The neutron irradiation on 4H SiC detectors causes a strong effect of free carrier compensation. This effect is due, principally, to two main causes: deactivation of the doping, and the increase in concentration of deep levels near to mid-gap. In our study it has been analyzed two different 4H-SiC particle detector, Schottky and junction detectors. The carrier compensation mechanism results different for these two kind of devices. In the Schottky detectors the compensation is mainly due to the increase of different deep levels with activation energy over 1 eV. These deep levels are related to point-like defect that has been produce by elastic scattering of the neutron in the lattice. The effect of the deactivation of the doping in the Schottky device is evident, but it is related to the forward current degradation, so it means that this effect does not affect the detector in its working condition. The carrier compensation in junction diodes is due to the increase in concentration of the only mid-gap deep level EH6/7; no other deep levels have been found that could participate in the compensation effect. In order to explain the behaviour of the junction detector it has been proposed a hypothesis: the formation of an insulating thin layer next to the epilayers surface. This layer completely is larger than the implanted barrier for high neutron fluence, so it has been explained the intrinsic behaviour of the current-voltage characteristics. The complete disappearance of the implantation induced broad band in the CL spectra can be due to a charging of the insulating layer that screens the CL emissions. In fact the spectra of the high fluence irradiated sample (M7) looks like to the un-implanted epilayers spectra. It is important to underline that the neutron irradiation does not introduce new deep levels but it increases the concentration of the deep levels, previously found. It is clear by the comparison of different techniques with different sensibility, as CL and DLTS.

High energy neutrons does not induce nuclear transmutation in the semiconductor, which can create shallow levels; but, due to their neutral charge, they cause the formation of point-like defect or simple complex, as silicon or carbon vacancies and related complex, by means of the elastic scattering.

It has been found also some interesting similar aspect for the two types of detector. The reverse conduction is dominated by the Z1/Z2 deep level in both device types. This acceptor level induces a compensation effect of the apparent carrier concentration but it acts as a generation center for reverse current conduction. The concentration profiling of the Z1/Z2 is different for the device types. In the junction detector the concentration of Z1/Z2 is higher in the near-surface region, and meanwhile in the Schottky diode the concentration is uniform across the sample. Z1/Z2 defect can segregate on the region next to the surface by high-temperature annealing as the results of evaporation of carbon. In the low fluence irradiated Schottky diode the correlation between the increase of this deep level concentration and the increase of the reverse current is evident. Another similar aspect is that it has been revealed the presence of line defects by EBIC and DLTS analysis in the different structure. The line defects cause a strain field that can be a source region of irradiation induced point-like defects.

The analysis of the junction diode has put in evidence also some effects due to the aluminium ion implantation; the implantation induced increase of the D_1 center concentration provoke a graded junction in the region next to the barrier. The graded junction can cause a degradation of the charge collection due to recombination effect in the region next to the surface.

Bibliography

[Ruddy] F.H. Ruddy et al., IEEE Trans Nucl. Sci. 45, 3, 536-539 (1998)

[RD50] RD-50 Status Report 2002/2003 CERN-LHCC-2003-058 and LHCC-RD-002

[IEEE] IEEE Trans. Electro Devices, 45 number dedicated to silicon carbide (1999)

[Castaldini01] A. Castaldini et al., Mat. Sci. For., vol 483-485, pp 359-364 (2005)

[Kalinina] E.Kalinina et al., Mat. Sci. For., vol 483-485, pp 377-380 (2005)

[Rogalla] Rogalla et al., Nucl. Phys. B (proc suppl.) vol 78, p. 516 (1999)

[Cunningham] W. Cunningham, Nucl. Instrum. Methods Phys Res A, Vol. 487, pp. 33-39 (2002)

[Castaldini02] A.Castaldini et al., J. Appl. Phys. 15 (2005)

[Alfieri] G.Alfieri et al., Mat. Sci. For., vol 483-485, pp 365-368 (2005)

[Menichelli] Menichelli et al., Diamond and Rel. Mat., vol 16, 1 (2007)

[Moscatelli] Moscatelli et al., IEEE Trans. Nucl. Sci., Vol. 53 (2006)

[Nava01] F.Nava et al., IEEE Trans. Nucl. Sci., NS-53, p. 238 (2004)

[Sciortino] S.Sciortino et al., Nucl. Instr. And Meth. In Phys. Res., A552, p.273 (2005)

[La Via] La Via F, Roccaforte F, Raineri V, Mauceri M, Ruggiero A, Musmeci P, Calcagno L, Castaldini A, Cavallini A, Microelectronic Engineering 70, p. 519 (2003)

[Nava02] F.Nava et al., Nucl. Instr. And Meth. In Phys. Res., Vol. A510, p. 273 (2003)

[Dascalu] D. Dascalu, G. Brezeanu, P. A. Dan, and C. Dima: Solid State Electron. 24, pp. 897–904 (1981)

[Definev] D. Defives, O. Noblanc, C. Dua, C. Brylinski, M. Barthula, V. Aubry-Fortuna, and F. Meyer: IEEE Trans. Electron Devices 46, pp. 449–455 (1999)

[Ewing] D.J: Ewing et al., J. Appl. Phys. 101, 114514 (2007)

[Sze] S. M. Sze: Semiconductor Devices - Physics and Technology (John Wiley and Sons, New York, 1985),

[Matsuaara] Matsuaara et al. Appl. Phys. Let., Vol. 83, 24, pp 4981-4983 (2003)

[Martini] M. Martini, J.W. Mayer, K.Zanio, Applied Solid State Science, vol 3, (Academic Press, New York, 1972)

[Chen] C.Q. Chen et al., J. Appl. Phys., vol 87,p. 3800 (2000)

[Hemmingsson] C.G. Hemmingsson et al. Phys rev. B, vol 58, p 16 (1998)

[Storasta] L. Storasta et al., Mat. Sci. For., vol 353-356, p 431-434 (2001)

[Son] N.T. Son et al., Mat. Sci. For., vol 433-435, p 45 (2003)

[Negoro] Y. Negro et al. Appl. Phys. Lett., Vol. 85,10, p 1716-1718 (2004)

[Moscatelli01] Moscatelli et al., Sem. Sci. Technol., Vol. 18, p554-559 (2003)

[Canino_Thesis] Mariaconcetta Canino, Ph.D thesis. Univ. Di Bologna (2007)

[Janson] Janson et al., J. Appl. Phys., Vol. 93, 8903 (2003)

[Troffer] Troffer et al., Phys. Stat. Soli. A, Vol. 162, Issue 1, p. 277-298 (1997)

[Storasta02] L. Storasta, Appl. Phys. Lett., Vol. 78, p. 46 (2001)

[Patrick] L. Patrick and W :J : Choyke, Phys. Rev. B, Vol. 5, P. 3253 (1972)

[Rao] M.V. Rao at al., J. Electron. Mater., Vol. 25, p. 75 (1996)

[Lebedev] A.A. Lebedev: Semiconductors, 33, p. 107(1999).

[Galeckas] A. Galeckas et al., Phys. Rev. B, Vol. 74, p. 233203 (2006)

[Fissel] A. Fissel et al., Appl. Phys. Lett. Vol. 78, 17, p. 2512-2514 (2001)

[Jones] K. A. Jones et al., J. Appl. Phys., Vol.96, 10, p. 5613-5618 (2004)

[Rigutti] L. Rigutti et al., Semicond. Sci. Technol., Vol 21, 6, p. 724-728 (2006)

[Pintillie] I. Pintillie et al., Appl. Phys. Lett., Vol. 81, p. 4841 (2002)

[Omling] P. Omling et al, Phys. Rev. B 32, 95, p. 6571-6581 (1985)

[CASINO] http://www.gel.usherbrooke.ca/casino/What.html

[Galeckas02] A. Galeckas, Phys. Sta. Solid., Vol. 191, 2, p. 613-620 (2002)

[Mitani] T. Mitani et al., Mat. Sci. For., in publish

[Aberg] D. Aberg et al., Appl. Phys. Lett., Vol. 78, 19, (2001)

Conclusions

Silicon carbide detectors have been irradiated with high energy neutrons up to fluences of 1 x 10^{16} cm^{-2}. It has been performed to clarify if silicon carbide could be a suitable material to replace the silicon in the tracking systems of the Large Hadron Collider (LHC) experiments. Schottky and junction particle detectors have been analyzed in order to clarify which structure has a higher charge collection efficiency and to comprehend the defects formation kinetics of the different structures. A preliminary thorough study of the un-irradiated aluminium implanted p+/n junction particle detector has been performed also to identify the device processing induced defects. It has been found two really interesting effects induced by the device processing. C-V measurements have shown strong carrier compensation in the region next to the barrier. It has been demonstrated that the compensation effect is not due to the aluminium implantation tail as expected, but to a deeper level, set at 0.35 eV from the valence band, by means of DLTS analysis. This level has been related to the well known D_1 center in 4H-SiC literature. The D_1 centre concentration profile suggests that the related defect is induced by the ion implantation of the *p* doping in a SiC epitaxial layer with a low net donor concentration. Analyzing the junction particle detector in the full depletion voltage condition (i.e. the working condition), it has been found that the reverse conduction is dominated by the Z1/Z2 deep level, in all the analyzed diodes. In the DLTS spectra of some diodes, this deep level does not appear. To clarify this effect, the Z1/Z2 concentration profile has been performed and it has been found that the deep level concentration is higher next to the barrier. Making a comparison with the DLTS measurements of a Schottky diode, synthesized on the same wafer, it has been recognized a similar behaviour of the Z1/Z2 concentration profile. The comparison has explained that the Z1/Z2 concentration profile is induced by a migration of the defect towards the

surface, segregating in the region next to it, and it has been, probably, caused by the post-implantation high temperature annealing.

The current-voltage characteristics of the irradiated diodes, Schottky and p^+/n, were affected by a strong compensation effect of the forward current. The samples become semi-insulating with a neutron fluence of 1x 10^{14} cm^{-2}. The combination of thermal activation energy measurements and PICTS analysis clarified that the compensation mechanism for Schottky and junction detectors is different. In the Schottky devices the compensation mechanism is due to the participation of different deep levels with activation energy near to mid-gap. Properly the decrease of the charge collection efficiency has been related to the increase of concentration of a deep level, set at 1.16 eV below the conduction band. Making a comparison with the SiC defect theoretical literature has been identified the traps related defects. All the defects found in this work are single point-like, as carbon or silicon vacancy, or small complex of intrinsic defects, as double vacancy or vacancy-interstitial. The decrease of the forward current can be also due to the decrease in concentration of the nitrogen doping donor. The nitrogen atoms, in substitutional site, are kicked off by the neutrons induced elastic scattering, and then the net donor concentration of the epi-layer decreases.

For the junction detector the compensation mechanism is dominated by one mid-gap deep level that increases in concentration as function of the neutron fluence. This level has activation energy of 1.6 eV below the conduction band. This deep level is related to the carbon vacancy. This defect induced a compensation effect which has been employed to growth high purity semi-insulating 4H SiC substrates. In the irradiated junction detectors, it has been proposed a hypothesis about the formation of an insulating layer next to the surface. This hypothesis is based on the results of different techniques, as PICTS, CL and secondary electron imaging.

In conclusion silicon carbide has demonstrated its high radiation hardness. The 4H-SiC particle detector continues working also after irradiation up to 1x10^{16} cm^{-2}. With this fluence, the detector has still a charge collection

efficiency of the 20%, when the common commercial silicon detector does not detect anymore. The aim for the improvement of silicon carbide, as particle detection material, is to grow larger wafer with lower intrinsic defects concentration.